

RICE UNIVERSITY

Ultralong-Range Molecules and Rydberg Blockade  
in Ultracold  $^{84}\text{Sr}$

by

Brian J. DeSalvo

A THESIS SUBMITTED  
IN PARTIAL FULFILLMENT OF THE  
REQUIREMENTS FOR THE DEGREE

Doctor of Philosophy

APPROVED, THESIS COMMITTEE:

J. C. Killian

Thomas C. Killian, Chair  
Professor of Physics and Astronomy,  
Department Chair

Randall G. Hulet

Randall G. Hulet  
Fayez Sarofim Professor of Physics and  
Astronomy

Philip R. Brooks

Philip R. Brooks  
Professor of Chemistry

Houston, Texas

July, 2015

## ABSTRACT

Ultralong-Range Molecules and Rydberg Blockade in Ultracold  $^{84}\text{Sr}$

by

Brian J. DeSalvo

This dissertation describes experiments on two-photon excitation of ultracold Sr to the  $^3S_1$  Rydberg series and represents the first experiments exciting Rydberg atoms via an intermediate triplet excited state. Due to the narrow linewidth (7.5 kHz) of the  $^1S_0 \rightarrow ^3P_1$  transition in Sr, this excitation scheme yields longer coherence times and less loss from the intermediate state compared to methods using the usual dipole allowed transitions. This is advantageous for realizing the possibility of Rydberg dressing, where a small amount of Rydberg character is admixed to ground state atoms allowing for continuously tunable long-range interactions. With this goal in mind, we explore the interplay of Rydberg blockade, Rydberg-Rydberg interactions, and ground-Rydberg interactions in high density, ultracold gases through Autler-Townes spectroscopy and photoassociation of ultralong-range Rydberg molecules.

First, we study ultra-long range  $\text{Sr}_2$  Rydberg molecules comprising one Rydberg atom and one ground-state atom. Molecules are photo-associated from an optically trapped thermal gas of  $^{84}\text{Sr}$  with lasers far-off resonance from the intermediate state and red-detuned from the atomic transition. The formation of molecules is detected as atom loss and the narrow spectroscopic features allow accurate determination of molecular binding energies as a function of principal quantum number. Comparison to theory yields good agreement and allows the first precision measurement of the

electron-Sr scattering length.

We then explore the density-dependent atomic photo-excitation line shapes in a thermal gas of  $^{84}\text{Sr}$  in an EIT configuration in the Autler-Townes regime. This is a promising configuration for Rydberg dressing. In this configuration we find fast loss due to Rydberg-Rydberg interactions in the form of energy level shifts and dephasing. To describe these effects, we employ a modified mean-field treatment taking in the effects of correlations and are able to capture the early time dynamics of the spectra.

Finally, we propose a method to detect Rydberg dressing in a BEC via low momentum transfer Bragg spectroscopy. We show preliminary results showing the sensitivity of this technique as well as calculations of the expected signal that it would detect.

## Acknowledgments

As I sit down to write this section, I realize that I need to exercise some restraint. This work represents the culmination of a long journey that began well before graduate school and as such there are many people who have helped me along the way. If I were to list every person who deserves acknowledgement here, I would likely double the length of the entire thesis. So in the interest of saving space, I submit the following incomplete list of the people who have made this work possible.

Many thanks to my advisor, Tom Killian, for his guidance and mentorship over the last seven years. He has always pushed me to improve my skills while giving me enough space to grow and make my own mistakes. To Barry Dunning, for taking the time to teach me about Rydberg atoms when we first decided to get into this work. His enthusiasm and relentless curiosity is truly inspiring. To Kaden Hazzard and Rick Mukherjee, for being some of the easiest to talk to theorists around. I hope I will have the opportunity to collaborate with both of them more in the future. To Pascal Mickelson and Natali Martinez de Escobar, for showing me the ropes and their years of hard work building the apparatus. To Mi Yan, for being my co-pilot on the apparatus for many years. To the new generation of Killian Lab students. It has been a lot of fun training and watching them grow from overwhelmed first-year grad students to mature independent physicists. To Jim Aman especially, for his hard work on all of the results presented here. I can't think of anyone else I'd rather have take over the experiment. To Dan Dries, James Hitchcock, Scott Pollock, Pedro Duarte, Ted Corcovilos, and Tobias Paprotta, for many great nights at Valhalla, where they taught me everything there was to know about ultracold atom experiments and grilling bacon wrapped shrimp. To Seth Aubin, for giving me my first taste of atomic

physics research at William and Mary and preparing me well to succeed in graduate school. To Jerry Ludwig, for making high school physics exciting and encouraging me to continue in the field. To many friends, especially Jed Pixley, Lindsey Anderson, Alex Witus, Marcel LaFlamme, Sara Haber, Joshua Rueckheim and Aditya Shashi, for their constant support and making my time in graduate school a lot more fun than it was probably ever supposed to be. To my dog, J.J. Thomson, for being a constant reminder of the importance of enjoying yourself and taking a walk once in a while. To Karen Rosenthal, for making these last two and a half years incredible and always being there for me. And finally, to my family, for everything.

# Contents

Abstract	ii
Acknowledgments	iv
List of Illustrations	ix
List of Tables	xv
<b>1 Introduction</b>	<b>1</b>
1.1 Rydberg Atoms	101 . . . . .
1.2 Why use Sr?	5 . . . . .
1.3 Rydberg Dressing	8 . . . . .
1.4 Thesis Organization	11 . . . . .
<b>2 Experimental Methods</b>	<b>12</b>
2.1 Introduction	12 . . . . .
2.2 Trapping and Cooling of Sr	13 . . . . .
2.2.1 461 nm Cooling and Magnetic Trapping	13 . . . . .
2.2.2 689 nm Laser Cooling	18 . . . . .
2.2.3 Optical Dipole Trap	19 . . . . .
2.3 Creating Rydberg Atoms	22 . . . . .
2.3.1 689 nm Photon Source	23 . . . . .
2.3.2 319 nm Photon Source	26 . . . . .
2.3.3 Locking the Laser	31 . . . . .
2.4 Detecting Rydberg Atoms	35 . . . . .
2.5 Electric Field Control	39 . . . . .
2.6 Finding a Rydberg Line	41 . . . . .

<b>3 Ultralong-Range Rydberg Molecules</b>	<b>45</b>
3.1 Introduction . . . . .	45
3.2 Submitted Publication: Ultralong-Range Rydberg Molecules in a Divalent-Atomic System . . . . .	46
3.2.1 Abstract . . . . .	46
3.2.2 Main Body . . . . .	46
3.3 Additional Material . . . . .	59
3.3.1 Rydberg Excitation . . . . .	59
3.3.2 Stark Shift Measurements . . . . .	61
<b>4 Rydberg Blockade Effects on Autler-Townes Spectra in an Ultracold Dense Gas</b>	<b>64</b>
4.1 Introduction . . . . .	64
4.2 Theoretical Groundwork . . . . .	65
4.2.1 Interaction Effects . . . . .	65
4.2.2 Rydberg-Rydberg Interactions . . . . .	69
4.2.3 Mean-Field Theory and Beyond . . . . .	71
4.2.4 Density Scaling . . . . .	75
4.2.5 Local Density Approximation . . . . .	77
4.2.6 A Quick Word on $\Gamma$ . . . . .	79
4.2.7 Previous Work . . . . .	80
4.3 Autler-Townes Spectra: Comparison of Experiment and Theory . . .	82
4.3.1 Experimental Details . . . . .	82
4.3.2 Calculation Details . . . . .	84
4.3.3 Short Time Dynamics . . . . .	85
4.3.4 Long Time Dynamics . . . . .	89
4.4 Conclusions . . . . .	90

<b>5 Probing Rydberg Dressing</b>	<b>96</b>
5.1 Introduction . . . . .	96
5.2 Measuring Interaction Strengths . . . . .	96
5.3 Bragg Spectroscopy . . . . .	98
5.4 Dispersion Relation for a Rydberg Dressed BEC . . . . .	101
5.4.1 Realizing Rydberg Dressing - Some Limitations . . . . .	105
5.4.2 Bragg Spectroscopy - Results . . . . .	108
5.5 Outlook . . . . .	112
<b>6 Conclusion</b>	<b>115</b>
<b>A Matlab Code</b>	<b>118</b>
<b>Bibliography</b>	<b>131</b>

# Illustrations

1.1	Physical origin of Rydberg blockade. a.) Two identical two-level atoms under the influence of resonant light. b.) Rydberg-Rydberg interactions shift the doubly excited state out of resonance for closely spaced atoms. . . . .	4
1.2	Schematic diagram of typical two-photon excitation scheme. . . . .	6
2.1	Partial level diagram of Sr showing all transitions for laser trapping and cooling. . . . .	14
2.2	Example measurement of the vertical trap oscillation frequency. Data (red dots) is fit with a decaying sinusoid (blue dashed line) which yields an excellent fit. The slow decay of the envelope allows the observation of many oscillation periods yielding high sensitivity of the fit to the frequency. . . . .	22
2.3	Example data of Rabi oscillation used to calibrate the intensity of the 689 nm laser. . . . .	25
2.4	Schematic layout of laser system used to generate 319 nm light for excitation to the $^3S_1$ Rydberg series. A small fraction of the 638 nm light is used to lock the laser via an optical transfer cavity, while the remainder is frequency doubled and delivered to the atoms. . . . .	27
2.5	Autler-Townes spectra at various detunings of the 319 nm laser. As a function of 319 nm laser detuning, the relative weight and position of the peaks varies and can be used to find resonance. . . . .	30

2.6	Autler-Townes spectra are used to accurately find the $^3P_1 \rightarrow 24s^3S_1$ resonance and measure the Rabi frequency of the 319 nm laser. . . . .	31
2.7	Autler-Townes spectra with 319 nm laser on resonance with the $^3P_1 \rightarrow 24s^3S_1$ transition. Here we see symmetric loss peaks spaced by the Rabi frequency, $\Omega_{12}$ . . . . .	32
2.8	Schematic diagram of transfer cavity used to lock 319 nm laser. 689 nm light stabilized to the $^1S_0 \rightarrow ^3P_1$ transition provides an absolute frequency reference for this system. . . . .	33
2.9	Spectroscopic measurement showing that excitation to a Rydberg state causes loss of atoms from the ODT. Repumping atoms from the $^3P_2$ state shows that radiative decay to metastable dark states is at least partially responsible for this loss. Note the same normalization is used for both data sets. . . . .	38
2.10	Schematic cross section of chamber (not to scale). When not in use, the MOT coils sit at a voltage of 5.6 V. Applying a voltage to the plate between one MOT coil and the glass window allows limited control of the electric field in the chamber. . . . .	40
2.11	Measurement of the quantum defect of the $ns^3S_1$ Rydberg series in Sr. The observed energies are fit extremely well using the Rydberg formula. . . . .	43
3.1	(Left) Atom-loss spectra and (Right) calculated potentials and wavefunctions, $R\chi_\nu(R)$ , for n=30 (top), 33 (middle), and 36 (bottom). The bars at the top of the molecular spectra indicate the positions of the theoretically-predicted binding energies of states bound by $> 1$ MHz and the curves at the bottom indicate their calculated excitation strength. The origin of each frequency axis is set to the center of the atomic excitation spectrum (see text). . . . .	51

3.2	Scaling of observed molecular binding energies, showing $1/(n - \delta)^6$ scaling for higher quantum numbers and more deeply bound levels. . . . .	57
3.3	a.) Cartoon layout of geometry used in experiment. 689 nm and 319 nm lasers copropagate with orthogonal linear polarizations. b.) Simplified level diagram of transitions probed in experiment yielding an effective one photon transition to the Rydberg state. . . . .	59
3.4	Example of a narrow atomic spectra taken with during the course of the Rydberg molecule experiment. The obtained spectrum is well described by a gaussian with a full width at half max (FWHM) of 550 kHz. This is limited by the linewidth of the 319 nm laser, and gives confidence that stray magnetic fields do not cause significant problems in our magnetically sensitive excitation scheme. . . . .	61
3.5	Measurement of the polarizability of an $n = 36$ Rydberg atom and a ground state Rydberg molecule at $n = 36$ . Both show the same polarizability within experimental uncertainty. . . . .	62
4.1	Simplified level diagram of the three level system under consideration.	67
4.2	Effects of a constant $V$ or $\Gamma$ on Autler-Townes spectra. While increasing $V$ causes asymmetry in the strength of the peaks and shifts their position, increasing $\Gamma$ causes a broadening and eventually a strong loss feature at zero detuning. . . . .	68
4.3	Excitation strength for exciting two $30s^3S_1$ Rydberg atoms as a function of internuclear distance. Of primary importance here is that the interatomic potential is clearly not well behaved for internuclear spacings less than 750 nm. Calculation performed and figure prepared by Dr. Yoshida. . . . .	73
4.4	Interaction energy as a function of density for a few principal quantum numbers . . . . .	75

4.5	Histogram of shifts for a homogeneous gas of $10^4$ particles at varying $\rho/\rho_B$ . In appropriately scaled units, the data collapses onto a common curve for large $\rho/\rho_B$ .	76
4.6	Timing diagram for taking Autler-Townes spectra. Details in text.	83
4.7	Timing diagram for taking time evolution. Details in text.	84
4.8	Blue squares: Experimental data of ground state population after a single pulse of excitation with initial peak density, $\rho_0 = 1.9 \times 10^{12} \text{ cm}^{-3}$ . Details in text. Red lines: Theoretical calculation using LDA for varying strengths $V_{Ryd}$ and $\Gamma_{2Ryd}$ . $\alpha$ and $\beta$ are defined in text.	87
4.9	Blue squares: Experimental data of ground state population after a single pulse of excitation with initial peak density, $\rho_0 = 1 \times 10^{13} \text{ cm}^{-3}$ . Details in text. Red lines: Theoretical calculation using LDA for varying strengths $V_{Ryd}$ and $\Gamma_{2Ryd}$ . $\alpha$ and $\beta$ are defined in text.	88
4.10	Blue circles: Experimental data of ground state population after a single variable length pulse with initial peak density, $\rho_0 = 1 \times 10^{13} \text{ cm}^{-3}$ and $\Omega_{01} = 20.14 \text{ kHz}$ . Details in text. Red lines: Theoretical calculation using LDA for varying strengths $V_{Ryd}$ and $\Gamma_{2Ryd}$ . $\alpha$ and $\beta$ are defined in text.	89
4.11	Blue squares: Experimental data of ground state population after a single variable length pulse with initial peak density, $\rho_0 = 1 \times 10^{13} \text{ cm}^{-3}$ and $\Omega_{01} = 132.89 \text{ kHz}$ . Details in text. Red lines: Theoretical calculation using LDA for varying strengths $V_{Ryd}$ and $\Gamma_{2Ryd}$ . $\alpha$ and $\beta$ are defined in text.	90
4.12	Blue squares: Experimental data of time dependent ground state population after a single variable length pulse with initial peak density, $\rho_0 = 1.9 \times 10^{12} \text{ cm}^{-3}$ . Red lines: Theoretical calculation using LDA for $\alpha = 1$ and $\beta = 2$ .	91

4.13 Blue squares: Experimental data of time dependent ground state population after a single variable length pulse with initial peak density, $\rho_0 = 1 \times 10^{13} \text{ cm}^{-3}$ . Red lines: Theoretical calculation using LDA for $\alpha = 1$ and $\beta = 2$ .	92
4.14 Time evolution at $\Delta_{01} = 0$ with $\Omega_{01}/2\pi = 39.68 \text{ kHz}$ at various applied electric fields. There is no measurable difference in the time evolution yielding the conclusion that the presence of electric charges is not a likely source of dephasing.	93
5.1 a.) Cartoon representation of Bragg spectroscopy of a BEC. Counterpropogating laser beams with a small frequency difference create a moving optical lattice which can impart $2\hbar k$ momentum to the atoms which become spatially separated from the main cloud after a time of flight (TOF). b.) Energy level diagram of the three state system formed by the atoms and Bragg spectroscopy beams.	99
5.2 Depiction of how Rydberg dressing interactions modify the dispersion of a BEC with principal quantum number $n = 25$ and a peak density of $5 \times 10^{13} \text{ cm}^{-3}$ for various Rydberg fraction, $f$ . Note how the introduction of contact interactions yields a deviation from the free particle dispersion at all $k$ and Rydberg dressing only modifies the dispersion at low $k$ .	103
5.3 Dependence of dispersion of Rydberg dressed BEC on principal quantum number $n$ . The calculations use a constant Rydberg fraction, $f = 3 \times 10^{-3}$ and a peak density of $5 \times 10^{13} \text{ cm}^{-3}$ .	104
5.4 Cartoon of interactions between Rydberg dressed atoms. At large spacings, both atoms are dressed and experience the $1/r^6$ potential. However, at spacings less than one blockade radius, only one atom at a time can be dressed, leading to just a constant energy shift.	105

5.5 Example Bragg spectra for counter-propogating Bragg beams. Zero detuning corresponds to resonance for free particle dispersion. Inset: Absorption image of BEC and diffracted fraction. . . . .	109
5.6 Left Panel: Dependence of the width of Bragg spectra on exposure time. Right Panel: Example Bragg spectra for various exposure times. Data agree well with a gaussian (blue dashes) and appear slightly broader than expected from equation 5.3. This is evidence of broadening present in the system which ultimately limits the width to $\sim 2$ kHz. . . . .	110
5.7 Measurement of shift of Bragg peak as a function of peak density of the condensate. Data appears to agree well with shift expected from peak density rather than average density. . . . .	111
5.8 Example spectra for Bragg spectroscopy performed with beams crossed at ( $21^\circ$ ). Inset: Absorption image of BEC and diffracted fraction. Due to the overlap of Bragg peaks with opposite momentum, two diffracted clouds are visible in the image. . . . .	113

## **Tables**

2.1 Experimentally measured energies of selected levels of the ns <sup>3</sup> S <sub>1</sub> Rydberg series of <sup>84</sup> Sr. . . . .	44
---	----

# Chapter 1

## Introduction

Within the last 20 years, the study of quantum degenerate gases in atomic systems has grown to a booming industry. The extraordinary control afforded by this system has enabled great advances in the study of interacting many-body systems. Examples include the study of the BEC-BCS crossover [1], the creation of imbalanced Fermi superfluids [2] and the observation of the superfluid Mott-insulator phase transition in an optical lattice [3].

Despite the richness of this system and myriad of applications that exist, the scope of the physics we can access is ultimately limited. The interactions dominant in ultracold atom systems are short-ranged contact interactions that are relatively weak and simple in structure. Dipolar interactions, found in Rydberg atoms [4], polar molecules [5], and atoms with large magnetic moments [6, 7], are much stronger, long-ranged and in some cases anisotropic. This suite of features has led to the prediction that dipolar systems will exhibit a variety of fundamentally new and important phenomena. This includes phase transitions to strongly correlated classical crystals [8, 9, 10, 11, 12], roton-maxon excitations [9, 13], exotic spin and magnetic states [14], three-dimensional solitons [15] and supersolids [16, 17, 18, 11, 19, 13].

This thesis will focus on the use of Rydberg atoms as a dipolar interacting system. Strontium, with its divalent electron structure, yields advantages over alkali atoms for these purposes, however there is very little previous work done in exciting Rydberg

atoms in strontium. The work presented here represents a number of important first steps in studying Rydberg atoms in Sr, and hopefully builds a firm foundation for future work in the field.

## 1.1 Rydberg Atoms 101

We will begin with a brief overview of Rydberg atoms and their properties, which will help set the stage for the rest of this thesis. A Rydberg atom is simply an atom with an electron in a highly excited state characterized by the principal quantum number  $n$ . The first evidence of Rydberg atoms dates back to the late 1800's when it was realized that the wavelength of spectral lines (which corresponds to the binding energy of the excited states) of atomic hydrogen could be explained using a simple formula which we now know as the Rydberg formula [20].

Rydberg atoms are large in size and feature a number of exaggerated properties compared to ground state atoms. These properties scale with the principal quantum number, and a few useful scaling relations are given below for low angular momentum Rydberg atoms.

Property	n-scaling
Binding Energy $E_B$	$n^{-2}$
Orbital Radius	$n^2$
Lifetime	$n^3$
Polarizability	$n^7$

Rydberg atoms are not only confined to hydrogen, our simplest atom, and they have been studied in alkali and alkaline-earth metal atoms as well. Despite these

flavors of Rydberg atoms having much more complicated internal structure, it turns out that the binding energy is only slightly modified

$$E_B = \frac{R_y}{(n - \delta)^2} \quad (1.1)$$

where  $R_y$  is the Rydberg constant and  $\delta$  is the quantum defect. This quantum defect varies between atomic species and for a given species shows a strong dependence on  $l$ , the angular momentum quantum number, with the largest value for s states and decreasing for higher angular momentum states.

This observation tells us a lot about the nature of Rydberg atoms. The internal structure of the atom does not play a huge role in their properties. This makes sense as the majority of the atom's properties will come from the valence electron which will spend the majority of its time far away from the core. Since the quantum defect tells us about the interaction between the Rydberg electron and the core, it also makes sense that it is largest for s states as they have the largest overlap with the core. Higher angular momentum states will have a diminishing interaction with the core, so their quantum defect is smaller. Once we know the quantum defect, it is useful to define  $n^* = n - \delta$ , the effective principal quantum number. All of the above scaling relations hold for non-hydrogenic Rydberg atoms with the replacement of  $n$  by  $n^*$ .

So far we have only talked about the structure of Rydberg atoms, however we mentioned in the beginning that we are most interested in them for their interactions. At zero field, low  $l$  Rydberg atoms possess no permanent dipole moment. Therefore at long-range, the interaction between Rydberg atoms (at zero field and in the absence of a Forster resonance) is characterized by induced dipole-induced dipole (or van der Waals) interactions typically given as  $V = C_6/r^6$  where  $r$  is the internuclear spacing.

$C_6$  will vary from atomic species to atomic species and can be positive or negative yielding repulsive or attractive interactions respectively.  $C_6$  scales extremely strongly with principal quantum number as  $n^{11}$  and is on the order of  $1 \text{ GHz} \mu\text{m}^6$  at  $n = 25$ . This is an enormous energy scale in cold atoms systems so interactions in this system play a truly dominant role. It is also important to note that interactions between Rydberg atoms need not be isotropic. They are for s states owing to the spherical symmetry of the electron's orbit, however it is generally not the case for higher angular momentum states.

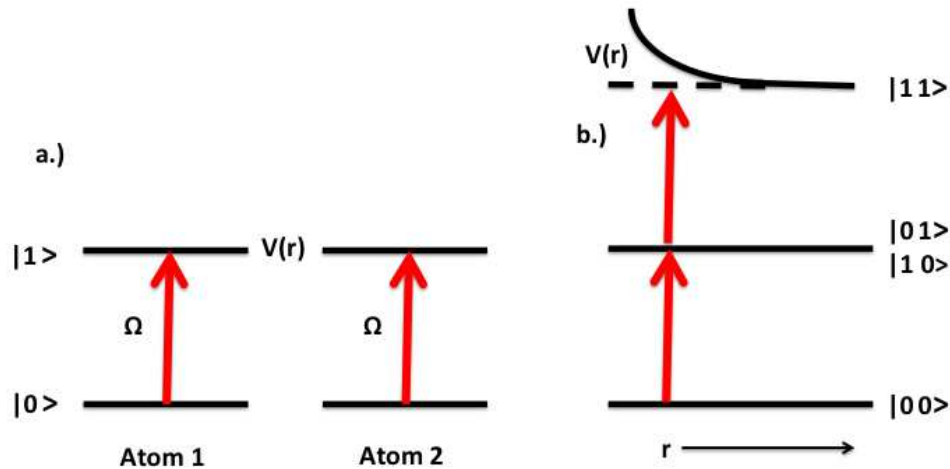


Figure 1.1 : Physical origin of Rydberg blockade. a.) Two identical two-level atoms under the influence of resonant light. b.) Rydberg-Rydberg interactions shift the doubly excited state out of resonance for closely spaced atoms.

A fascinating consequence of these strong interaction is the concept of Rydberg blockade. The concept of blockade is easily understood in just a two atom picture. As shown in figure 1.1, we begin by considering two, two-level atoms under the influence

of a laser coupling them to a Rydberg state. In the case of no interactions, our laser is resonant with transitions from  $|00\rangle \rightarrow |01\rangle, |10\rangle$  and  $|01\rangle, |10\rangle \rightarrow |11\rangle$ . However this is not the case if our upper state is interacting. Interactions shift the energy level of the  $|11\rangle$  state as a function of interatomic spacing. Therefore at close interatomic spacings, the laser is off resonant with the  $|01\rangle, |10\rangle \rightarrow |11\rangle$  transition. The effect of this is that if one atom is in a Rydberg state, the other atom cannot be excited within a certain radius known as the blockade radius. This effect makes spectroscopy of Rydberg atoms a rich field with many applications, and particularly close ties with quantum information and computing.

## 1.2 Why use Sr?

If you believe what I've said so far about Rydberg atoms and their properties, you are probably wondering why it matters that we are using strontium for our experiments. To understand the advantages that strontium affords us, we need to go beyond our basic treatment of Rydberg atoms.

The first advantage that Sr offers is variety. Single valence electron systems offer a number of Rydberg series with different values of  $l$ . However, divalent electron systems have both singlet and triplet configurations which each come different values of  $l$ , more than doubling the number of Rydberg states we have access to. Assuming we only want to restrict ourselves to s states with their isotropic interactions, Sr offers two flavors,  $ns^1S_0$  and  $ns^3S_1$  that feature attractive and repulsive interactions, respectively. So while an experiment dedicated to trapping and cooling of an alkali will be limited to either attractive or repulsive interactions, our strontium experiment

offers both.

A second major advantage comes from the way that we excite Rydberg atoms. Equation 1.1 implies that to excite a high  $n$  Rydberg atom from the ground state, we will need photon energies which are only slightly smaller than the ionization threshold for the atom. For most atomic species, single photon excitation to a Rydberg level requires a deep UV photon. Since the oscillator strength for a transition from the ground state to the Rydberg state is small, we also require a lot of power. High power CW UV lasers are difficult systems to come by, so this is only practical for certain atomic species. Also, with a single photon transition, one is forced to excite to p state Rydberg atoms. Two-photon excitation yields more flexibility (as one can couple to s or d states) and requires lower energy photons. This scheme is also preferable as it makes use of a strong intermediate transition and can yield improved coupling to the Rydberg state.

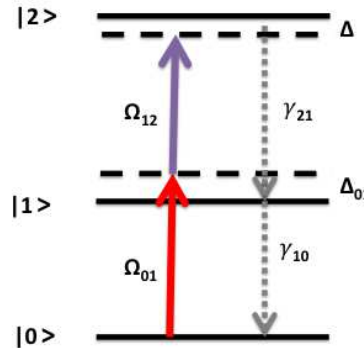


Figure 1.2 : Schematic diagram of typical two-photon excitation scheme.

However, two-photon excitation comes with a price. Atoms can be heated by the scattering of photons and two-photon excitation adds an additional channel for this

process to occur. For many applications, this heating is undesirable so we would like to minimize its effect. This is typically achieved by detuning the first laser far from the intermediate state as shown in figure 1.2. In the limit of far detuning and weak excitation, the total scattering rate due to the two lasers is given as

$$\gamma = \frac{\Omega_{01}^2}{4\Delta_{01}^2} \left[ \gamma_1 + \frac{\Omega_{12}^2}{4\Delta^2} \gamma_2 \right] \quad (1.2)$$

where  $\Omega_{ij}$  is the Rabi frequency of the laser driving the  $|i\rangle \rightarrow |j\rangle$  transition,  $\Delta_{01}$  is the detuning from the intermediate state,  $\Delta$  is the two-photon detuning from the Rydberg state, and  $\gamma_i$  is the decay rate from the state  $|i\rangle$ .

From equation 1.2, we see that the total scattering rate is the sum of scattering rates off of the two states involved, and therein lies the advantage of Sr. Narrow intercombination line transitions have decay rates which are orders of magnitude smaller than those of the usual electric dipole allowed transitions. So for the same coupling strength to a Rydberg level, Sr will suffer significantly less from off-resonant heating. On top of that, the value of  $C_6$  for an interacting pair of  $ns^3S_1$  Sr atoms [21] is almost twice that of a pair of  $ns^2S_{1/2}$  Rb atoms at the same principal quantum number. Overall, Sr promises a much more robust route to strong interactions.

Finally, there is a more subtle advantage that Sr offers. Again, due to the presence of two valence electrons in the atom, the Rydberg core remains optically active. Making use of this fact, one can actually directly image the core of the Rydberg atom as an alternate route of all optical detection of Rydberg atoms [22]. Also, this core provides necessary oscillator strength allowing for the creation of magic wavelength lattices where the ground state and Rydberg state see the same potential. The presence of doubly excited states allows for studies of auto-ionization [23] and can

strongly perturb Rydberg series. It has been postulated that these perturbations can lead to accidental degeneracies of Rydberg states and may allow stronger excitation rates of ultralong-range Rydberg molecules with large permanent dipole moments [24].

### 1.3 Rydberg Dressing

So far, I have focussed on the benefits of Rydberg atoms in allowing us to study strongly interacting dipolar gases. However, there is one tricky caveat which needs to be addressed in order to realize some of the more exciting proposals described in the introduction of this chapter. The  $n^3$  scaling of the lifetime of Rydberg atoms tells us that they can have a long lifetime. At  $n = 25$ , this corresponds to a few  $\mu\text{s}$ . While this is long compared to excited states we are used to working with, it is still unfortunately short on the timescale of typical dynamical timescales of ultracold atom experiments.

To overcome this challenge, an idea has been developed which is referred to as Rydberg dressing. A number of the proposals mentioned earlier make use of this idea. The basic principle is that rather than creating Rydberg atoms directly, we try to admix a small fraction of Rydberg character into the ground state, creating the state  $|\Psi\rangle \sim |g\rangle + \sqrt{f} |r\rangle$  where  $f$  is the fraction of Rydberg character. By working with this state, the lifetime can be greatly enhanced by a factor of  $1/f$ .

Consequently, the strength of the interactions also suffers by using this scheme. Interactions between Rydberg dressed atoms then take the form

$$V = \frac{f^2 C_6}{R_B^6 + r^6} \quad (1.3)$$

where  $R_B$  is the blockade radius and  $r$  is the interparticle spacing. However, recall that the bare Rydberg-Rydberg interactions are enormous (GHz) on the energy scale we are concerned with for ultracold atoms. Therefore, we only need  $f$  on the order of  $10^{-3}$  to make meaningful changes to the behavior of a gas, which extends the lifetime out to milliseconds. This simple picture breaks down if the density and fraction of Rydberg atoms is high enough such that there would be more than two Rydberg atoms per blockade volume in the absence of blockade effects as described in [25], but most experiments do not reach beyond this regime. As an added bonus, within this regime of validity, controlling the Rydberg fraction allows continuous tuning of the interaction strength, which is a powerful control knob to have on our experiment.

There are two schemes that can be used in order to implement Rydberg dressing. The first and more commonly referred to is off-resonant excitation. This method employs two-photon excitation with the first laser far detuned from the intermediate state to minimize off-resonant heating. The second laser is then tuned to the red (blue) of a repulsively (attractively) interacting Rydberg state respectively. This allows the creation of the desired dressed state. The fraction of Rydberg character is controlled by a combination of the two photon Rabi frequency  $\Omega$  and the two photon detuning,  $\Delta$  as  $f = \Omega^2/4|\Delta|^2$ . This is advantageous as the two control parameters allow more flexibility with which to find a regime of low loss.

Alternatively, one can use electromagnetically induced transparency, which for the parameters we work with in strontium results in Aulter-Townes splitting of the excitation spectrum. For this scheme, both lasers of the two photon transition are exactly resonant with the transitions they are driving. With a strong laser coupling on the intermediate to excited state transition, two dressed states are created that

are a superposition of the intermediate and excited state and are split by the Rabi frequency of the strong laser. If driven strongly enough, there will be negligible loss on resonance and the Rydberg fraction will be controlled as  $f = \Omega_{01}^2 / \Omega_{12}^2$ .

Of course, these schemes are not perfect and we have ignored possible issues with them. For off-resonant excitation, a major concern is the creation of ultralong-range Rydberg molecules. These are molecules comprised of one Rydberg and one or more ground state atom(s) that can be photoassociated when the lasers are detuned to the red of the atomic transition. Therefore it is essential that one measures the binding energy of these molecules so that enhanced loss due to creating molecules can be avoided. Autler-Townes splitting yields no concern for the creation of molecules, however one needs to be careful about how we apply our theory. Observed Autler-Townes spectra can be heavily influenced by interactions and dephasing, so the loss rates for an interacting Rydberg system are not as simple as expected from naive non-interacting theory.

So far, there have only been two reported experiments that have attempted to see the effects of Rydberg dressing. The first attempt was made in the group of Tilman Pfau with Rb [25]. Due to the loss rates that were seen in this experiment, they conclude that it is highly unlikely that Rydberg dressing will ever be observed in a bulk gas of Rb. The second was successful, however it avoided many of the complications described by only using a system of two atoms [26]. While this experiment is an important first step, it does not represent the realization of long range interacting many-body system as we would ultimately like to achieve.

## 1.4 Thesis Organization

With the ultimate goal of Rydberg dressing of a BEC in mind, we can understand the framework of this thesis. In chapter 2, I develop the experimental tools and tricks used in our system. I provide a brief introduction to laser trapping and cooling and the preparation of ultracold samples of  $^{84}\text{Sr}$ . Then a detailed description of the laser systems used to excite Rydberg atoms is given as well as an explanation of the methods we use to detect them. With the basics of how to perform an experiment in place, chapter 3 discusses our measurement of the binding energy of ultralong-range Rydberg molecules. This work aids in understanding how best to implement Rydberg dressing in the off-resonant scheme. Chapter 4 then discusses Autler-Townes spectroscopy and provides a minimal model in which to understand the extremely large loss rates we observe. Finally, in chapter 5, I discuss a plausible method with which one can eventually detect and measure the effects of Rydberg dressing in a BEC.

## Chapter 2

# Experimental Methods

### 2.1 Introduction

In our quest to create a Rydberg-dressed BEC, we need methods to produce a quantum degenerate sample of Sr, and methods to create and detect Rydberg atoms. My earliest experiments during my PhD career were creating BECs and degenerate Fermi gases of all of the isotopes of Sr, so between our work and that of Florian Schreck's group, the former has been well established [27, 28, 29, 30, 31, 32]. As such I will only provide a brief outline. The apparatus used here has been described in more detail in the PhD theses of Sarah Nagel, Natali Martinez de Escobar, Pascal Mickelson and Mi Yan. Note for all work described here, we work with the bosonic isotope  $^{84}\text{Sr}$ , so I will only discuss cooling and trapping of this isotope. For a discussion of the complications of working with fermionic  $^{87}\text{Sr}$ , refer to my master's thesis and Pascal Mickelson's PhD thesis.

Making and detecting Rydberg atoms is also not new territory. However, there are interesting peculiarities of working with Sr that demand attention. Also, as our apparatus was not originally intended for this application, we have found creative solutions to the detection of Rydberg atoms and molecules. These techniques are easily applicable and should be of interest to the Rydberg community at large.

## 2.2 Trapping and Cooling of Sr

### 2.2.1 461 nm Cooling and Magnetic Trapping

At room temperature, Sr is a solid metal. For laser trapping and cooling, we need to work with gaseous Sr, so we begin by heating a sample in an oven up to  $\sim 350^{\circ}\text{C}$  to obtain a significant vapor pressure. The resulting gas of atoms escapes the oven via an array of 0.4" long capillary tubes formed from size AWG-21 hypodermic needles. These tubes collimate the gas into a beam directed towards the main chamber. This nozzle is similar in design to the one described in the master's thesis of Francisco Camargo, however it has one key difference. Our nozzle does not use a heat shield and is therefore not able to achieve the same high temperature resulting in a reduced atom flux. Directly out of the nozzle, the atoms undergo a stage of two dimensional optical molasses to further collimate the beam. After the transverse cooling, the atoms are decelerated in a Zeeman slower to velocities suitable for capture in a magneto-optical trap (MOT).

These initial cooling stages, and our first stage MOT, utilize the  ${}^1\text{S}_0 \rightarrow {}^1\text{P}_1$  transition in Sr, which requires a laser operating at a wavelength of 461 nm. Until recently, diodes that directly generate 461 nm light were only available at low power. The broad linewidth of the transition results in a large saturation intensity,  $40.5 \text{ mW/cm}^2$ , so laser powers on the order of 100 mW are necessary for the initial cooling stages. Our system is based on frequency doubling of IR diode lasers, which can provide the power necessary. High powered 461 nm diodes are now available, and are used on the new apparatus in the Killian lab. For more information on the advantages (and headaches) of the all diode system, please refer to the master's thesis of Francisco

Camargo.

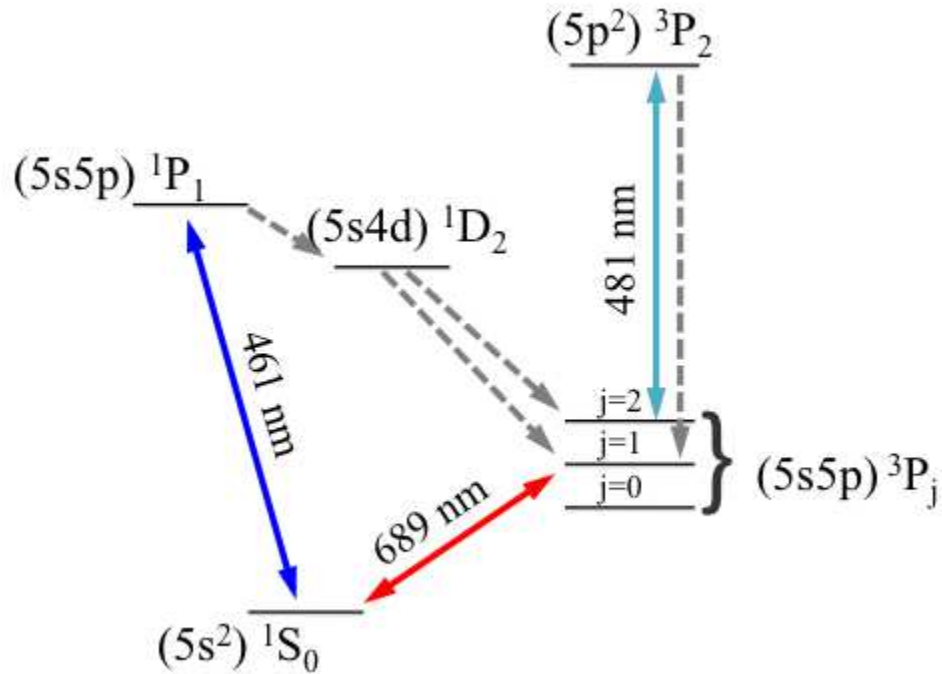


Figure 2.1 : Partial level diagram of Sr showing all transitions for laser trapping and cooling.

We use a 922 nm Littrow-configuration diode laser from Sacher Lasertechnik as a master laser for the system. Light from this diode is fiber coupled and then split with an acousto-optic modulator (AOM) into two separate tapered amplifiers (TA) from Eagleyard. Typically 20 - 25 mW of IR is used to seed each TA, which ultimately provides 300 - 350 mW. Light from each TA is then coupled into separate frequency-doubling cavities using potassium niobate as the non-linear medium for second harmonic generation. When well optimized, each cavity is capable of providing  $\sim$  100 mW of 461 nm light. All power from one cavity is dedicated to Zeeman slowing,

while the other is split using AOMs to create beams for the transverse cooling, MOT, imaging, and saturated-absorption spectroscopy.

We lock the laser to the zero crossing of an error signal from a magnetically tunable, saturated-absorption cell via feedback to the current of the master laser. A good description of the principles of the magnetically tunable saturated-absorption cell can be found in the undergraduate senior thesis of Mike Perron. As  $^{88}\text{Sr}$  is overwhelmingly the most abundant isotope, we always lock the laser to the error signal from this isotope. For trapping  $^{84}\text{Sr}$ , we use a combination of AOMs and the magnetic tuning of the cell to get the cooling beams on resonance with the isotope we are interested in trapping.

Laser cooling on the  $^1S_0 \rightarrow ^1P_1$  transition is ideal for the initial cooling stage owing to the fast cooling rate and large capture velocity which results from the short lifetime of the excited state and short wavelength of the transition. This lifetime yields a broad (30.5 MHz) linewidth. However, laser cooling on this transition also comes with the significant drawback that the Doppler temperature is high by ultracold atom standards,  $T_D = \frac{\hbar\gamma}{2k_B} \simeq 1 \text{ mK}$ . The lack of nuclear spin in bosonic Sr means that sub-Doppler cooling is not possible in this system. Therefore the temperature of the 461 nm MOT cannot be reduced below this limit. Even worse, the isotopic abundance of  $^{84}\text{Sr}$  is extremely small, only 0.6%. This means that for our best loading efforts, the steady state number of atoms in the MOT is only  $\sim 10^6$ , which is too small for our needs.

This obstacle can be overcome by taking advantage of a peculiar feature of the level structure of Sr. The  $^1S_0 \rightarrow ^1P_1$  transition is not completely closed, and atoms from the  $^1P_1$  state can decay via the  $^1D_2$  state to the  $^3P_2$  state with a probability

of  $1 \times 10^{-5}$ . This state is metastable and has a long lifetime, limited in experiment by blackbody radiation to about 25 s. Within the  ${}^3P_2$  manifold, atoms in low-field seeking  $m_j$  states can be magnetically trapped by the quadrupole field of the MOT where they remain for their lifetime while being dark to the cooling light [33]. The observed 25 s lifetime of this trap is orders of magnitude longer than the lifetime of the MOT, which allows us to use long loading times. While the loading rate of atoms into the magnetic trap is clearly reduced compared to the loading rate of the MOT (we need to scatter  $10^5$  photons for an atom to end up in the magnetically trapable state), the loss rate is reduced further. Therefore, for long load times we get an increase of overall number of atoms and can typically trap between  $10 - 15 \times 10^6$   ${}^{84}\text{Sr}$  atoms in this trap, which is sufficient for our purposes. It is also worthwhile to note that optimization of our system for number of atoms in the magnetic trap is not equivalent to optimization of number of atoms in the MOT, and in practice we use the former to collect the largest samples.

After this collection phase, the atoms are returned to the ground state via a repumping transition. Within the last few years, we have begun repumping along the  $(5s5p){}^3P_2 \rightarrow (5p^2){}^3P_2$  using a 481 nm laser. This transition has a few advantages over other schemes used so far for repumping Sr. Other schemes include using 497 nm [34] or 3  $\mu\text{m}$  [35], which require expensive laser systems for such an uninteresting purpose. Another popular choice is the combination of 707 nm and 679 nm. While these are less expensive diode lasers, the requirement of two independent laser systems makes this scheme more complicated than desired. By using the  $(5s5p){}^3P_2 \rightarrow (5p^2){}^3P_2$  transition, only a single diode laser is necessary.

Another advantage to this repumping transition is the relative ease of stabilizing

the laser. It is difficult to prepare a large number of atoms in the  ${}^3P_2$  state in a reference cell, so it is challenging to directly lock the laser to a transition from this state. However, it is a fortunate coincidence that there is an absorption line in ground state tellurium within  $0.01\text{ cm}^{-1}$  of the transition in Sr [36, 37]. The laser can then be referenced to the tellurium transition which is easily driven in a vapor cell and detuned to be on resonance with Sr by a number of means. Details on the reference cell and spectroscopy done in our lab can be found in the undergraduate senior thesis of Pakorn Wongwaitayakornkul.

Since the Doppler-broadened line in a  $\text{Te}_2$  vapor cell overlaps the transition we want to drive in Sr, we use a low-bandwidth side-of-peak lock to the Doppler-broadened line while rapidly dithering the laser over many MHz to cover a broad frequency range. As the repumping laser is currently shared between the three experiments in the Killian lab (which at any given time might be working with any isotope of Sr), this allows us to repump multiple isotopes simultaneously. Unfortunately, as temperature drifts in the vapor cell cause the lock point to move, the repumping efficiency can change. While the temperature of the cell is controlled, it has been found that it is not stable enough for our purposes. As such, we monitor the wavelength of the laser on a wavemeter to make sure the laser does not drift too far, and we change the lock point on the circuit to adjust for the drift, however, this is far from ideal. With the laser being dithered over such a broad range, repumping is slow. We typically repump atoms for 50 ms to return them to the ground state where they can be recaptured in the 461 nm MOT and are prepared for further cooling.

A future improvement to this scheme would use use Doppler-free  $\text{Te}_2$  spectroscopy to eliminate sensitivity to temperature changes and hopefully stop the drift. With this

improved laser stabilization, we would be able to perform more precise spectroscopy on the  $(5s5p)^3P_2 \rightarrow (5p^2)^3P_2$  transition for all isotopes of Sr, and use a combination of AOMs to directly address each transition individually, which should improve the repumping rate.

### 2.2.2 689 nm Laser Cooling

With the atoms retuned to the ground state, we employ a second MOT operating on the  ${}^1S_0 \rightarrow {}^3P_1$  transition which features a narrow 7.5 kHz linewidth. This significantly reduces the Doppler temperature to a few hundred nK and in practice we regularly obtain samples between 1 - 2  $\mu$ K after 200 ms of laser cooling. It should be noted that for  ${}^{84}\text{Sr}$ , with its low abundance, the transfer from the magnetic trap to the  ${}^1S_0 \rightarrow {}^3P_1$  MOT is essentially lossless. This is not the case for more abundant isotopes as light-assisted collisions limit the number of atoms in the  ${}^1S_0 \rightarrow {}^3P_1$  MOT.

Light for driving the  ${}^1S_0 \rightarrow {}^3P_1$  transition is derived from a homebuilt Littman-Metcalf configuration diode laser and a series of injection-locked slave lasers (3 dedicated to forming MOT beams for various isotopes and 1 for generating spectroscopy beams). To get the full benefit of the narrow linewidth transition we are driving, it is important to have a narrow laser source. Even in Littman-Metcalf configuration, a typical extended cavity diode laser will still have a linewidth on the order of a few hundred kHz. To improve on this, we stabilize the master to a high finesse cavity with a high bandwidth servo on the laser current. This allows narrowing of the laser spectrum to approximately 30 kHz. A low bandwidth lock on the PZT voltage is used to keep the correction voltage to the current small to prevent the system from unlocking.

The high finesse cavity mirrors are mounted on PZTs to allow a variation of the length of the cavity. With the laser locked to the cavity, light from an injection-locked slave is then sent to a saturated absorption cell which produces an error signal. The length of the cavity is then locked to the zero crossing of this error signal, which keeps the laser on resonance with the atoms. As was the case for the 461 nm light, we always lock the laser to the error signal from  $^{88}\text{Sr}$  and use AOMs to make up the isotope shift for working with other isotopes

As mentioned, our laser system is still broad with respect to the transition. For all applications we have found so far, this is not much of a limitation. However, a narrower laser should lead to more precise spectroscopy and laser cooling to colder temperatures. As such, at the time of this writing, a Toptica DL Pro is being installed on the experiment as a new master laser. This system should provide a narrower intrinsic linewidth and higher bandwidth for feedback to allow further narrowing of the spectrum.

### 2.2.3 Optical Dipole Trap

Following this cooling stage, we load atoms into a crossed optical dipole trap (ODT). The ODT is derived from a multimode 18 W IPG fiber laser at 1064 nm. The trap is formed by two cylindrically focussed beams with waists  $300\ \mu\text{m}$  ( $65\ \mu\text{m}$ ), and  $440\ \mu\text{m}$  ( $38\ \mu\text{m}$ ) in the horizontal (vertical) dimension respectively. These beams propagate in the horizontal plane and are crossed at a  $90^\circ$  angle. Each beam is controlled by an independent AOM that provide a 5 MHz frequency difference between the beams to minimize interference effects, which can distort the shape of the trap. Interference effects are also mediated by using orthogonal polarizations on the two

beams. Independent AOMs also allow for more freedom when designing an effective evaporation trajectory. After a 1 s hold in the ODT, we typically have trapped  $2 - 4 \times 10^6$  atoms at a temperature of 700 nK. Evaporative cooling for 5-6 seconds in this trap produces pure condensates of  $3 - 5 \times 10^5$  atoms. This trap was initially designed for creating BECs of  $^{86}\text{Sr}$ , which requires low densities for evaporation due to the high three-body loss rate of this isotope. While other trap geometries we have available might produce condensates of  $^{84}\text{Sr}$  faster or in larger numbers, this trap allows us to easily make low density samples, which is more important for the studies at hand.

For the experiments described here, we halt the evaporation before a BEC forms. It is essential for us to know the density distribution of the atoms in the trap, and this boils down to knowing the number and temperature of the atoms in the trap as well as the trap oscillation frequencies. Absorption imaging after a long time of flight allows us to measure the atom number and temperature accurately, so all that remains is measuring the trap oscillation frequencies.

In previous versions of our ODT, we used a recycled a beam though the chamber to form the crossed beam trap. While this makes good use of the laser power and creates deep traps, it limits the options available for accurately measuring trap frequencies. Specifically, we were forced to rely on the method of parametric heating for our measurements. Using this technique, one modulates the intensity of the laser beams to heat atoms out of the trap. When the modulation frequency matches the trap oscillation frequency, one sees a large heating and loss of atoms from the trap. This technique has a few problems. As atoms can be excited at harmonics and subharmonics of the trap frequency, there is a bit of detective work that goes

into truly extracting the trap frequencies. This was complicated by the fact that our trap was nearly spherical resulting in almost degenerate trap frequencies. Strange lineshapes also make determination of the line center difficult, so a large amount of data is usually needed to get a good measurement.

However, with the ODT used here, measuring trap oscillation frequencies is a breeze. Two things work to our advantage here: First, the independent control of each beam allows more degrees of freedom to excite modes than just intensity modulation. Second, as the beams are perpendicular to one another and mutually orthogonal to gravity, the principal axes of the trap are aligned with gravity and the propagation direction of the beams. Using this, we can measure the trap oscillation frequencies by simply initiating a sloshing motion along a principal axis in the trap and fitting the time dependent position to a decaying sinusoid. For the vertical direction, this is done by briefly turning off one or both of the ODT beams for 1 ms, which is long enough for the atoms to acquire some velocity but not displace too far from the center of the trap. For the horizontal axes, we abruptly change the driving frequency of one of the AOMs creating the arms of the ODT. This translates the beam slightly in the horizontal direction and starts the motion. As the motion in the trap is small, it is helpful to look at the atoms after a time of flight. This amplifies the motion as a change in velocity results in a change in final position and makes it easier to resolve the motion.

A typical measurement of the vertical axis trap oscillation frequency is shown in figure 2.2 with a fit to the data. As can be seen, the agreement between the data and the fit is excellent. Typically, we measure our trap frequencies at the conclusion of an experiment to calibrate the density and obtain agreement with the model developed

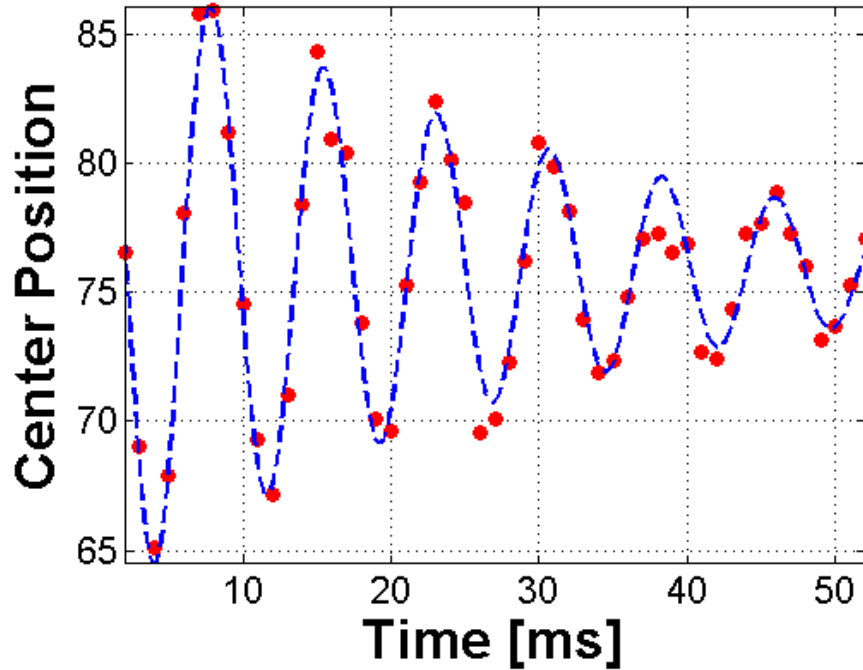


Figure 2.2 : Example measurement of the vertical trap oscillation frequency. Data (red dots) is fit with a decaying sinusoid (blue dashed line) which yields an excellent fit. The slow decay of the envelope allows the observation of many oscillation periods yielding high sensitivity of the fit to the frequency.

in [38] to within 20%. Deeper traps typically show better agreement as they are less sensitive to misalignment and gravity. However, whenever there is a disagreement between the model and the measurement, we use the measured values.

### 2.3 Creating Rydberg Atoms

With an ultracold sample prepared, we now need to excite the atoms to a Rydberg state. As discussed in the introduction, there are many flavors of Rydberg states to

choose from in Sr. For the work described here, we will be exciting atoms exclusively to the  $^3S_1$  Rydberg series. This state provides isotropic repulsive interactions and is accessed via the narrow  $^1S_0 \rightarrow ^3P_1$  transition.

### 2.3.1 689 nm Photon Source

The first photon for our two-photon excitation comes from a source that we have already discussed, the 689 nm laser. Depending on the specifics of the experiment we are performing, we have very different needs for this laser source. For excitation far off resonance with the intermediate state, we need large detunings and high intensities. However, for Autler-Townes spectroscopy, we need on-resonance low intensity beams. To allow this flexibility, we find it useful to have an injection-locked slave dedicated entirely to this purpose. With a combination of AOMs on the light used to injection lock the slave as well as AOMs on the output of the laser, we can achieve detunings between -70 and + 250 MHz. For all applications, we couple the beams into single-mode, polarization-maintaining fibers and typically obtain about 6-10 mW of light to deliver to the atoms.

Fiber coupling is useful for a number of reasons. First, it cleans up the spatial mode of the laser, which is important if one wants to have a reliable and smooth laser intensity pattern. More importantly, fiber coupling is extremely helpful for aligning the laser to the atoms. A typical technique is to use atom loss from the ODT to aid in alignment, however, for far-off-resonance light, this is not practical. By using fiber coupled light, we are able to first use light resonant with the atoms to align the output of the fiber, and then couple in the light we need for our application.

As the 689 nm system is locked to an atomic reference and all beams derived from

it come from AOMs driven by stable RF sources, we know the detuning of our laser extremely accurately. However, to understand the dynamics of the system, we will also need to know the Rabi frequency of the light. Recall that the Rabi frequency is defined as  $\Omega_{ij} = \frac{eE}{\hbar}\mu_{ij}$  where  $e$  is the charge of the electron,  $E$  is the magnitude of the oscillating electric field, and  $\mu_{ij}$  is the matrix element connecting states  $|i\rangle$  and  $|j\rangle$ . The  $^1S_0 \rightarrow ^3P_1$  transition has been extensively studied, so the matrix element of the transition is well known [37]. Therefore, we only need to know the intensity of the beam (and therefore the magnitude of the electric field) accurately to calculate the Rabi frequency. For small beams, this is easily achieved. We measure the profile of the laser beam on a rotating slit beam profiler and calibrate the power with a photodiode. However, for experiments on Autler-Townes spectroscopy, we need very low Rabi frequencies, which requires the use of very large beams. As the waist of these beams are too large to measure on a beam profiler, we need an alternative method.

This can be done by recalling a classic result which is taught in any AMO class worth its salt, Rabi oscillations. A two-level atom that is subject to on-resonance light will oscillate between states  $|1\rangle$  and  $|2\rangle$  at a frequency exactly equal to the Rabi frequency. If we are able to detect the state of the atom and drive our atoms on resonance, we should be able to see this effect. As Rabi oscillations are a coherent phenomenon, it is important to have a sense of decoherence rates that will damp the oscillations. One primary concern is the finite lifetime of the excited state. Fortunately for us, the  $^3P_1$  state has a  $21 \mu s$  lifetime, which yields a long coherence time during which we can see Rabi oscillations.

To perform this measurement we begin with a cold, trapped sample of  $^{84}\text{Sr}$  in the ODT. We release the atoms from the trap and then immediately expose the atoms

to a pulse of 689 nm light. Within a few  $\mu s$  of the excitation we then image the atoms using 461 nm light. Atoms in the  $^3P_1$  state will not absorb light from the 461 nm laser, so we expect that the number of atoms measured via absorption imaging will oscillate as the population oscillates between the ground and excited state. The results of one such experiment are shown in figure 2.3.

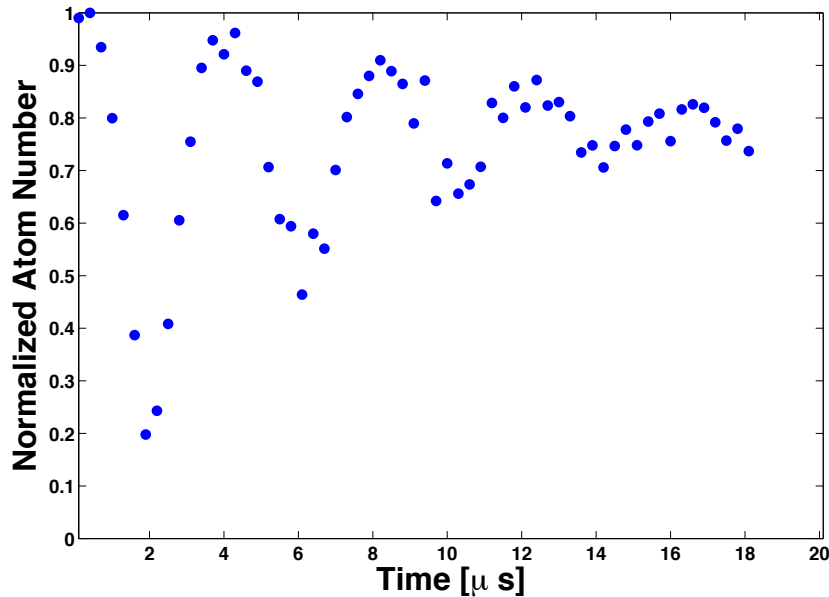


Figure 2.3 : Example data of Rabi oscillation used to calibrate the intensity of the 689 nm laser.

There are a few important things to note about the data shown in figure 2.3. First, the finite time necessary to image the atoms (a few  $\mu s$ ) allows some population to return to the ground state, which results in a less than 100% contrast of the oscillations. Second, as we need to image the atoms within the 21  $\mu s$  lifetime of the excited state, the optical depth of the sample is very high which causes problems for

absorption imaging. For high densities, the optical depth causes us to undercount the number of atoms in the cloud. In the data above, this is apparent as the population in the ground state does not tend to 50% of the original population. While this skews the data, it only affects the amplitude of the oscillations and final steady state value, but does not affect the measured frequency. There are ways around this issue, such as using far-detuned imaging light to reduce the optical depth or using a blow away pulse to clear out atoms in the ground state and then image the remaining atoms after a long time of flight. However, here we are only concerned with measuring the Rabi frequency so our imperfect measurement will suffice. Finally, it should be noted that the decay rate of the oscillations is significantly faster than the spontaneous decay rate of the excited state. This implies that something other than spontaneous emission is causing decoherence in the system. The most likely candidate is the linewidth of the laser, as it was previously known that the laser had a 30 kHz linewidth and the observed decay rate matches this timescale well.

### 2.3.2 319 nm Photon Source

To drive the second leg of the two-photon transition, we need a 319 nm photon source. As this laser is coupling to a Rydberg state, the specifications for this laser are no less demanding than those of our 689 nm laser. The wave functions of the  $(5s5p)^3P_1$  state and the  $^3S_1$  Rydberg series have relatively small overlap, so the oscillator strength of these transitions is small. To overcome this hurdle, it is necessary to drive the transition with a significant amount of laser power. Also, similar to our concerns with driving the  $^1S_0 \rightarrow ^3P_1$  transition, the long lifetime of Rydberg states ( $\sim 5\mu s$  near  $n = 25$ ) necessitates using a narrow-linewidth laser. High output power and narrow

linewidth usually do not go hand in hand, and it is only through a complicated multistage laser system that we are able to meet these needs. A schematic layout of the system is shown in figure 2.4.

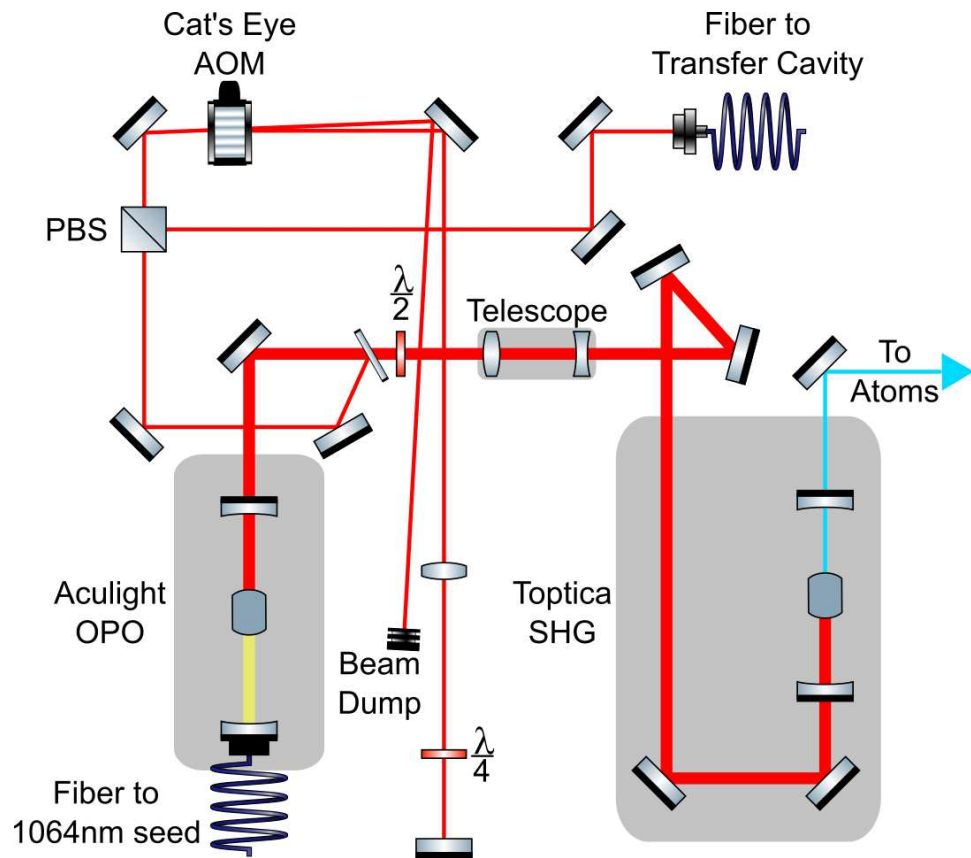


Figure 2.4 : Schematic layout of laser system used to generate 319 nm light for excitation to the  $^3S_1$  Rydberg series. A small fraction of the 638 nm light is used to lock the laser via an optical transfer cavity, while the remainder is frequency doubled and delivered to the atoms.

Our system begins with an Argos Orange system from Lockheed-Martin (originally provided by Acculight before the company was purchased by Lockheed-Martin). This system uses a fiber-laser seed at 1064 nm which is amplified in an IPG fiber amplifier

to 8W. This light is then coupled to a bow-tie cavity that contains two sections of non-linear crystal. The first performs frequency down conversion whereby the 1064nm photon is down converted into signal and idler photons of  $\sim 1.5 \mu\text{m}$  and  $3 \mu\text{m}$  respectively. In the second section of crystal, the signal and 1064 nm photons are then summed to create 638 nm. The output power depends on the exact wavelength used, but is typically between 0.8 - 1.2 W.

To achieve efficient conversion efficiency to 638 nm, one needs to temperature tune the crystal to satisfy the phase matching condition for both nonlinear processes. For the crystal in our system, this was found to be near 33 °C. Unfortunately, the temperature control of the Argos system is designed to only heat, and with the heat load due to the high-power pump, the system cannot maintain this temperature on its own. To work around the problem, we have affixed a water-cooling block to the cavity housing which provides additional cooling such that the Argos system can maintain the temperature needed. It should also be noted that while the system can be run with much higher pump powers (up to 12 W), it is difficult to keep the laser single mode at these high powers. Therefore, we always opt to run at 8 W of pump power or lower. The system is temperamental and prone to mode hops, however with time and patience, it can be mastered.

The 638 nm light passes through a window to pick off a small fraction of the beam that is used to lock the laser, while the remainder is beam shaped via a telescope and directed into a Toptica SHG Pro frequency doubling cavity to create 319 nm light. The Toptica system works well and can provide a conversion efficiency of up to 20%. When the system was first installed, we found the alignment of the 638 nm into the SHG Pro needed to be adjusted every other day. It was later determined that

this instability was caused by the beam passing very near the edge of the non-linear crystal inside the cavity. By translating the crystal, the output power of the cavity is much more stable and can run for weeks without readjustment, unless the desired wavelength is changed.

There has not been much spectroscopy done on the  $^3S_1$  Rydberg series, and so there is not as much information available on these transitions. Again, we need a technique to directly measure the Rabi frequency. Measuring Rabi oscillations is not practical here, but Autler-Townes spectroscopy provides a direct route to this. In a later chapter, we will see that Autler-Townes spectroscopy with large densities of Rydberg atoms leads to very complicated spectra. But, as long as we keep the initial density low, the excitation time short and the Rabi frequency of the probe beam small, then we can essentially see non-interacting Autler-Townes spectra that are easy to interpret.

The classic picture of the Autler-Townes spectrum is easy to understand in the dressed state picture. We can begin by just thinking about a two level atom under the influence of near resonant light with a Rabi frequency  $\Omega$  and a detuning  $\Delta$ . Within the rotating wave approximation Hamiltonian for this system is  $H = H_{atom} + H_{int}$  where

$$H_{atom} = \hbar\Delta |1\rangle\langle 1| \quad (2.1)$$

$$H_{int} = \frac{-\hbar}{2}(\Omega |2\rangle\langle 1| + \Omega^* |1\rangle\langle 2|). \quad (2.2)$$

Clearly the states of the atom  $|0\rangle$  and  $|1\rangle$  are not the eigenstates of this system. We can diagonalize the Hamiltonian to find its eigenstates, which are the so called dressed

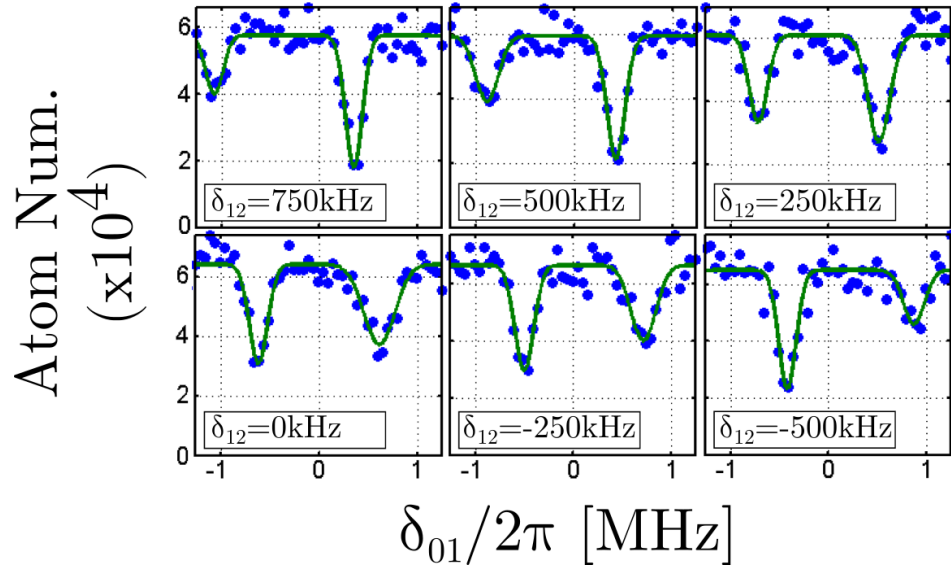


Figure 2.5 : Autler-Townes spectra at various detunings of the 319 nm laser. As a function of 319 nm laser detuning, the relative weight and position of the peaks varies and can be used to find resonance.

states  $|+\rangle$  and  $|-\rangle$  and have the eigenenergies

$$E_{\pm} = \frac{-\hbar\Delta}{2} \pm \frac{\sqrt{\Omega^2 + \Delta^2}}{2} \quad (2.3)$$

From this equation we can see that on resonance, the dressed states are split in energy by exactly the Rabi frequency.

To see Autler-Townes splitting in our system, we need a strong coupling laser on the  ${}^3P_1 \rightarrow ns {}^3S_1$  transition with a weak probe on the  ${}^1S_0 \rightarrow {}^3P_1$  transition. To measure the Rabi frequency accurately, we also need to know that the UV laser is directly on resonance. This is done by taking a series of Autler-Townes spectra and measuring the spacing between the peaks. Examples of the obtained spectra are seen in figure 2.5. As the detuning of the UV laser varies, the relative weight of the peaks

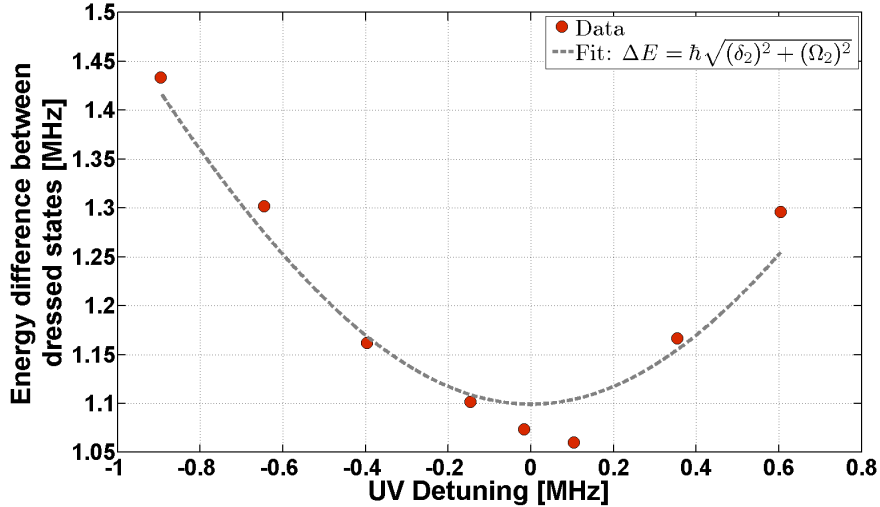


Figure 2.6 : Autler-Townes spectra are used to accurately find the  ${}^3P_1 \rightarrow 24s\,{}^3S_1$  resonance and measure the Rabi frequency of the 319 nm laser.

varies. However, the spacing between these peaks is always  $\sqrt{\Omega^2 + \Delta^2}$ . By fitting the data we can determine the resonance position, as shown in figure 2.6. On resonance the loss peaks are symmetric and their spacing is exactly the Rabi frequency, so this method serves as a direct measurement of the Rabi frequency. An example spectrum on resonance is shown in greater detail in figure 2.7.

### 2.3.3 Locking the Laser

So far, I have not described how we actually lock the 319 nm laser. As the light is resonant with a transition from a metastable state, there is no absorption feature that we can easily use to derive an error signal. Instead, we stabilize the laser with an optical transfer cavity.

The transfer cavity is a non-degenerate optical cavity with highly reflective mirrors

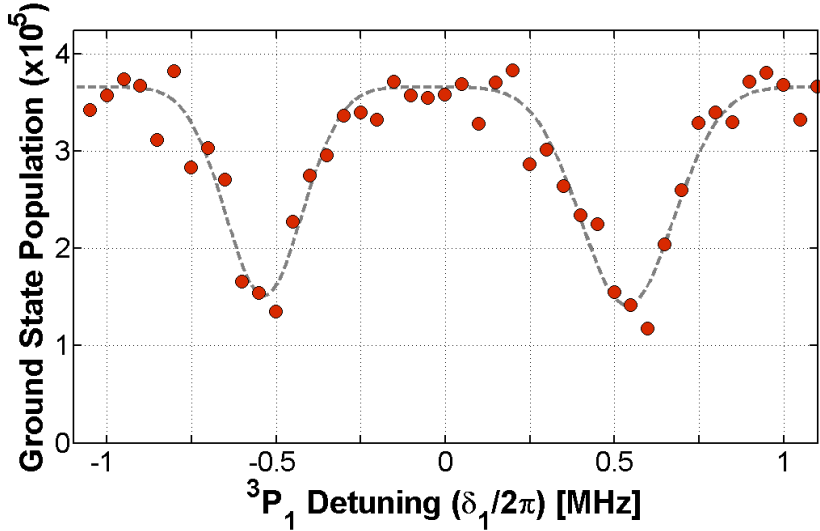


Figure 2.7 : Autler-Townes spectra with 319 nm laser on resonance with the  ${}^3P_1 \rightarrow {}^2S_1$  transition. Here we see symmetric loss peaks spaced by the Rabi frequency,  $\Omega_{12}$ .

for both 689 nm and 638 nm mounted on an invar spacer. The linewidth of the cavity for these two wavelengths is 7.3 MHz and 5.1 MHz respectively. Since the 689 nm light is stabilized to the  ${}^1S_0 \rightarrow {}^3P_1$  transition, this serves as an absolute frequency reference. The mirrors of the cavity are mounted on PZTs which allow control of the length of the cavity. On one side, a stack of 4 PZTs are driven with a static voltage of 0 - 350 V to allow scanning over 3-4 free spectral ranges of the cavity (1 FSR = 735 MHz). The other side uses only 2 PZTs driven with 0-150 V which are used for fast timescale feedback. We use the Pound-Drever-Hall method [39] to generate an error signal and feedback to the shorter stack PZTs to stabilize the length of the cavity to the 689 nm light.

As depicted in figure 2.4, light from the 638 nm laser is passed through a 200

MHz AOM in a double pass configuration and fiber coupled to the transfer cavity setup. The output of the fiber is mode matched to the cavity and combined with the 689 nm light via a dichroic mirror. We again use the Pound-Drever-Hall method to generate an error signal for the 638 nm light and lock the laser. Fine tuning of the laser frequency is then achieved by modifying the driving frequency of the double pass AOM, and more coarse tuning is achieved by locking the laser to a different transmission peak. This system is shown schematically in figure 2.8.

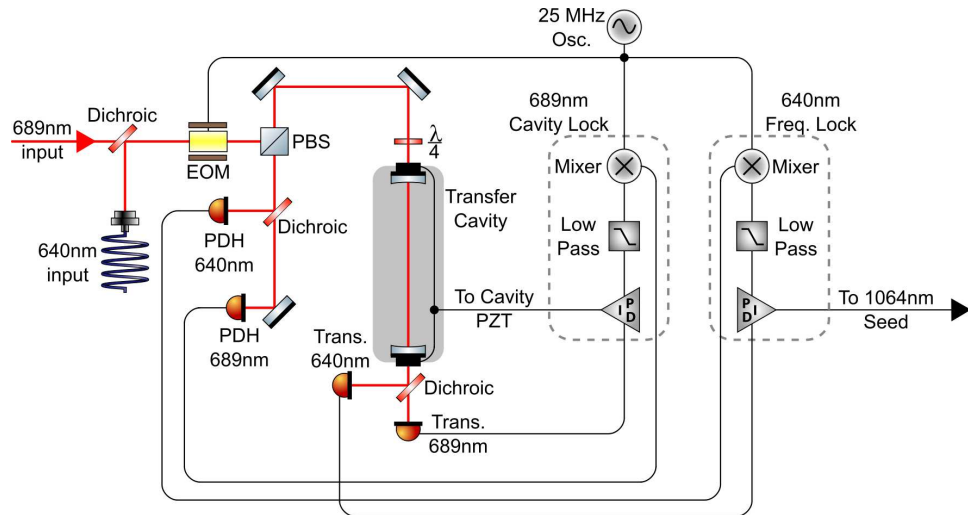


Figure 2.8 : Schematic diagram of transfer cavity used to lock 319 nm laser. 689 nm light stabilized to the  ${}^1S_0 \rightarrow {}^3P_1$  transition provides an absolute frequency reference for this system.

Achieving a high-bandwidth lock of this laser has been a challenge, and we have ultimately succeeded using a two stage system. The fundamental problem is with the tuning characteristics of the fiber-laser seed. Of the methods available to tune the wavelength of the 638 nm laser, the fastest response comes from tuning the PZT on

the fiber laser seed. However, there is a significant phase shift that appears in the frequency response of the PZT starting around 1 Hz. This limits the bandwidth of our feedback to only a few Hz resulting in a very weak lock and linewidth of 550 kHz.

To improve this, we have placed an AOM directly after the Argos module. By using the 1st diffracted order of the AOM, we can now feedback to the drive frequency of the AOM to lock the laser with kHz feedback bandwidth. One problem with this scheme is that changing the drive frequency will change the angle of the beam which is undesirable. As this angle changes, we see a change in the conversion efficiency of 638 nm to 319 nm. To mitigate this effect, our circuit only allows the frequency to change by a few hundred kHz so the resulting power changes are relatively small. Also, the UV light passes through another AOM before entering the chamber, and we then use the UV AOM to power control that beam and remove the intensity fluctuations. Large, slow-timescale drifts are compensated by a low-bandwidth lock on the fiber laser PZT. The scheme is more complicated than one might desire, but it has allowed us to narrow the laser to 300 kHz. Replacing the fiber-laser seed with another laser with better tuning characteristics should also be able to solve the problems that we have had.

One last note of importance is that we have found it essential to isolate the cavity from pressure fluctuations. The differing indices of refraction of air at 689 nm and 638 nm makes the relative position of the transmission peaks sensitive to pressure changes in the lab. The simple act of opening or closing a door was seen to shift the lock point of the 638 nm light by about 1 MHz, which is too large for precision spectroscopy. To mitigate this problem, we have sealed the cavity by affixing caps on either end of the invar spacer to create an airtight seal. This has reduced the

frequency fluctuations to below our measurement resolution.

## 2.4 Detecting Rydberg Atoms

Now that we have a method to excite Rydberg atoms, we need a way of detecting them. The most common technique of detecting Rydberg atoms is field ionization followed by charged-particle detection. Rydberg atoms are so weakly bound that it is possible to apply an electric field large enough to detach the Rydberg electron from the core. Using smaller guiding electric fields, either the ion or electron is deflected towards a detector and the charge deposited on the detector heralds that a Rydberg atom was created.

Our apparatus does not have electric field plates inside of the chamber or a charge sensitive detector, so an alternate method is needed. It turns out, due to the level structure of Sr, measuring ground state atom loss will give us a signal proportional to the number of Rydberg atoms created.

There are a few different reasons why the creation of a Rydberg atom would lead to the loss of a ground-state atom. The first is that the excitation has given the atom enough energy to leave the trap. The recoil energy of a 689 nm photon plus that of a 319 nm photon combined is  $1.36 \mu\text{K}$  with the recoil energy defined as  $\frac{\hbar^2 \vec{k}^2}{2m}$ . This is sufficient to eject an atom from a shallow trap; however for deep traps, it is not enough. Subsequent emission of the photons can add up to double this energy, but only for atoms which emit photons in a direction opposite that of the absorbed photon. Another reason for loss is that Rydberg atoms can decay into metastable dark states. This is more useful because loss in this channel works equally well at all trap depths.

Atoms in a  ${}^3S_1$  Rydberg state can radiatively decay via many channels to lower lying states, however for simplicity we'd like to only consider the dominant decay paths. From a semiclassical treatment, the rate of spontaneous emission for a dipole allowed transition is given by

$$\Gamma_{J_i, M_i \rightarrow J_f, M_f} = \frac{\omega_{i,f}^3}{3\pi\epsilon_0\hbar c^3} \sum_{M_f} |\langle J_f, M_f | \vec{d} | J_i, M_i \rangle|^2 \quad (2.4)$$

where  $\omega_{i,f}$  is the frequency difference between the initial and final states and  $\vec{d}$  is the dipole operator. The  $\omega_{i,f}^3$  dependence in the above equation tells us that the rate of spontaneous emission is largest when the energy difference between the states is the largest. The dominant decay channels in our case are from the Rydberg state to the lowest lying states connected via dipole allowed transitions, the  $(5s5p){}^3P_{0,1,2}$  states.

All three of the states are metastable as they cannot decay to the ground state via dipole-allowed transitions. However, we know from the fact that we drive the  ${}^1S_0 \rightarrow {}^3P_1$  transition that it is possible to break these selection rules. This is due to the fact that the spin-orbit interaction breaks down the LS coupling scheme such that the  ${}^3P_1$  state actually has some  ${}^1P_1$  character, so the transition becomes weakly allowed. However, transitions from the  ${}^3P_2$  and  ${}^3P_0$  state are forbidden by two dipole-selection rules and have lifetimes of minutes. As a result of this, atoms that decay from the Rydberg state to the  ${}^3P_1$  state will subsequently decay to the ground state within  $21 \mu s$ , while Rydberg atoms that decay to the  ${}^3P_2$  or  ${}^3P_0$  state will not return to the ground state on the timescale of our experiment and are seen as loss of ground state atoms when we image, even after a long time of flight.

It turns out that the polarizability of the  ${}^3P_2$  state at 1064 nm is similar to that of the ground state, therefore these atoms actually remain trapped in the ODT. To

verify that our loss is coming from the creation of metastable atoms, we perform the following experiment. In the first scan, we use our two-photon excitation far off resonant with the intermediate state to excite atoms to the Rydberg state for 6 ms and count the number of ground-state atoms after a long time of flight, confirming that our excitation shows ground-state atom loss. We then repeat the same sequence, except immediately after the Rydberg excitation we illuminate the cloud with resonant 461 nm light for 3 ms, which is longer than the lifetime of the Rydberg state used as well as the  $^3P_1$  state. This rapidly clears out remaining ground state atoms while leaving  $^3P_2$  atoms unaffected. After this clearout pulse we expose the repump laser for 15 ms before releasing the atoms from the trap and imaging. With this procedure, we will only see atoms which were in the  $^3P_2$  state during the clearout pulse. Figure 2.9 shows that the loss of atoms from the trap coincides with the creation of  $^3P_2$  atoms as expected. Atoms should also decay to the  $^3P_0$  state and remain trapped, however we do not have the necessary repump laser available to detect these atoms.

From figure 2.9, we know that a significant fraction of Rydberg atoms decay to the  $^3P_2$  state, but it is difficult to be quantitative about the number of Rydberg atoms created. We need to know the trap depth for  $^3P_2$  atoms as well as the efficiency of repumping to make quantitative statements, and this is difficult to do. So instead, we will use atom loss as our probe, and turn to theory to figure out the number of Rydberg atoms which will decay back to the ground state and which will end up in metastable states. Using equation 2.4, we can calculate the branching ratio of decay to these three states.

The states we are concerned about are only separated in energy by a small amount, so the effect of differing  $\omega_{i,f}^3$  for these states is relatively small. Instead the dominant

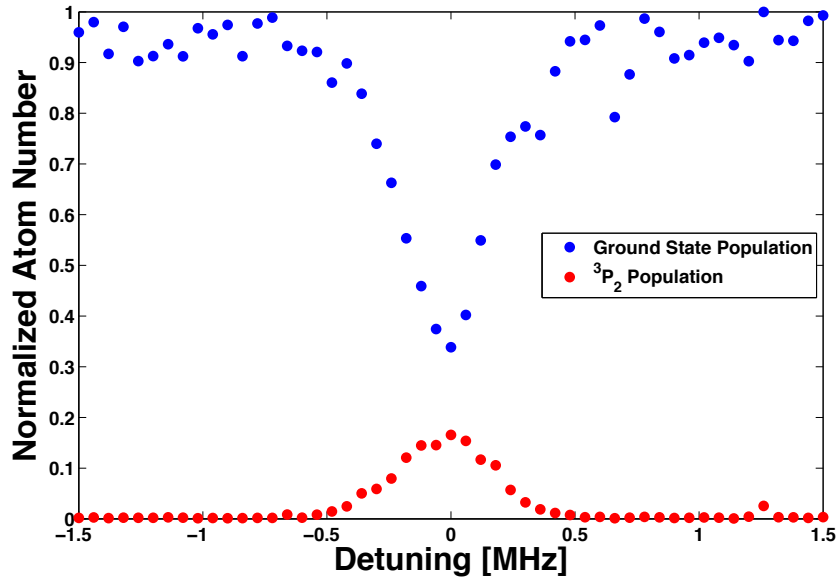


Figure 2.9 : Spectroscopic measurement showing that excitation to a Rydberg state causes loss of atoms from the ODT. Repumping atoms from the  $^3P_2$  state shows that radiative decay to metastable dark states is at least partially responsible for this loss. Note the same normalization is used for both data sets.

source of the difference in decay rates comes from evaluating the dipole matrix element. To simplify our calculation of the branching ratio, we make use of the reduced dipole matrix element. Using the Wigner-Eckart theorem [40], the relevant matrix element can be rewritten as

$$\langle J_f, M_f | e\vec{r}_q | J_i, M_i \rangle = \langle J_f | |e\vec{r}| |J_i \rangle (-1)^{J_i-1+M_f} \sqrt{2J_f+1} \begin{pmatrix} J_i & 1 & J_f \\ M_i & q & -M_f \end{pmatrix} \quad (2.5)$$

where  $\langle J_f | |e\vec{r}| |J_i \rangle$  is the reduced matrix element,  $q$  labels the polarization of the emitted photon, and the brackets denote the Wigner 3J symbol. This can be further

simplified by expressing the reduced matrix element as

$$\langle J_f | \vec{e} \cdot \vec{r} | J_i \rangle = \langle L_f | \vec{e} \cdot \vec{r} | L_i \rangle (-1)^{J_i + L_f + 1 + S} \sqrt{(2J_i + 1)(2L_f + 1)} \left\{ \begin{matrix} L_f & L_i & 1 \\ J_i & J_f & S \end{matrix} \right\} \quad (2.6)$$

where L labels the orbital angular momentum quantum number of the state, S labels the spin, and the curly brackets denote the Wigner 6J symbol. By combining these equations, the matrix element can be expressed as a number we can calculate multiplied by a reduced matrix element which depends only on L. Since all states we are interested in are p states, the reduced matrix element cancels out in the calculation of branching ratios. All that remains is careful book keeping to appropriately sum over the possible  $M_f$  values for each  ${}^3P_J$  manifold and look up the appropriate Wigner 6J and 3J symbols. Neglecting the energy difference of the emitted photons, we find that the population will decay from the  ${}^3S_1$  state to the  ${}^3P_2({}^3P_1)[{}^3P_0]$  state with a probability of  $5/9(1/3)[1/9]$ , respectively. If the energy difference is taken into account we obtain 58.8% to the  ${}^3P_2$ , 32.6% to the  ${}^3P_1$  and 8.6% to the  ${}^3P_0$  manifolds.

This calculation tells us that there is a significant probability of an atom decaying to a metastable state and not returning to the ground state, so atom loss is a useful technique in this system to detect the creation of a Rydberg atom.

## 2.5 Electric Field Control

As mentioned previously, Rydberg atoms are sensitive to electric fields, so it is important to have some control over the field in the chamber. Unfortunately, our apparatus was not designed with this application in mind, so our control over fields is limited.

The primary limitation is the design of our chamber. The top and bottom flanges of the UHV chamber where the experiment takes place feature recessed windows that

sit approximately 1 inch from the atoms. Glass is particularly troubling as patch charges can develop on the glass yielding inhomogeneous fields in the chamber. To reduce our sensitivity to this, we choose to work at low principal quantum number where the DC polarizability of the Rydberg atoms is smaller (recall this scales as  $n^7$ ). Fortunately, for the level of sensitivity we have for Rydberg levels near  $n = 30$ , the field inside the chamber is relatively stable from day to day.

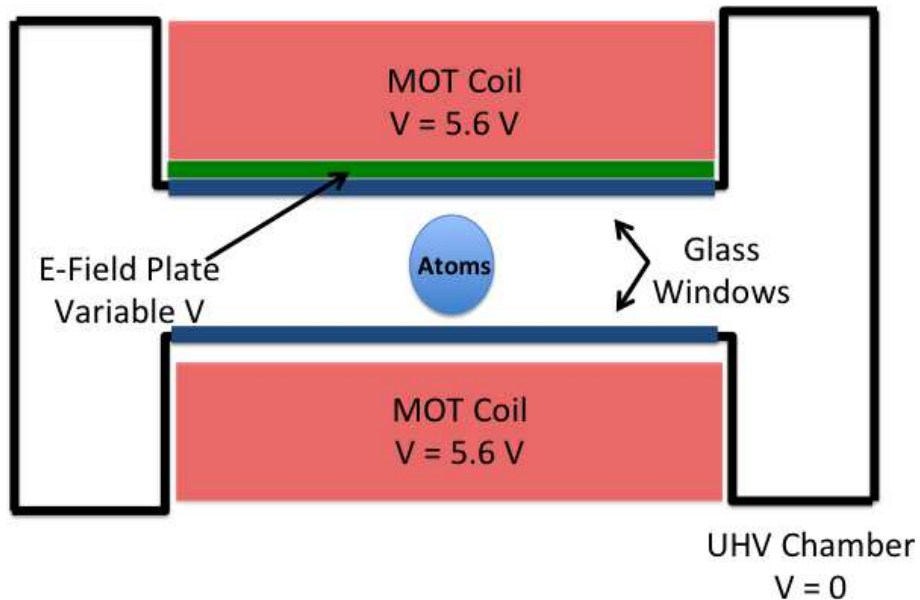


Figure 2.10 : Schematic cross section of chamber (not to scale). When not in use, the MOT coils sit at a voltage of 5.6 V. Applying a voltage to the plate between one MOT coil and the glass window allows limited control of the electric field in the chamber.

To control the field inside the chamber, we place an annular ring between one of the MOT coils and the glass window as shown in figure 2.10, and apply a voltage to

it. This only allows control of the field in one dimension which severely limits our ability to make quantitative measurements of the polarizability of Rydberg atoms. However, as will be shown later it is sufficient to make relative measurements of the polarizability of Rydberg atoms and molecules. Also, it can give us a lower bound on the field experienced by any ions which might be created to allow estimation of the timescale it takes them to leave the trap.

It is noticed that the absolute value of the voltage we apply to the ring must remain below 8 V otherwise a charging effect is evident on the glass and the field can no longer be controlled. However, if this occurs, we have seen that the charging of the glass dissipates over the course of a few hours. Due to the limitations of charging of the glass and the potential of the MOT coils, it should be noted that there is an asymmetry in the value of the field we can apply.

## 2.6 Finding a Rydberg Line

This final section is dedicated to the art of finding a Rydberg line. As I previously mentioned, there has been limited spectroscopy on the triplet Rydberg series in Sr, so there is not much data to guide the hunt. Therefore one needs to be willing to be patient and persistent when looking for a new line. In the spirit of full disclosure, it took about two weeks of constant searching to find the first Rydberg line on our experiment. I hope that the knowledge I pass on here helps other grad students avoid that particular trauma.

Between previous work [41, 42] and calculations from knowledge of the quantum defect [21], it is easy to get within a few GHz of the line position. Assuming you

know the position of the line within this range there are a few ways to proceed. First, you can try two-photon excitation of atoms trapped in the 461 nm MOT, however this technique is only efficient for  $^{88}\text{Sr}$ . As  $^{88}\text{Sr}$  is the most abundant isotope, it is easy to create a large MOT with a few  $10^8$  atoms in steady state. With that many atoms fluorescing, the fluorescence can be monitored on a photodiode as the MOT is loaded continuously. With both laser beams aligned to the MOT, one will see a decrease in fluorescence as the UV laser scans across resonance. Unfortunately, we cannot create large enough MOTs of the other isotopes to monitor the fluorescence, so this technique is not useful for other isotopes.

A second technique, which can be applied to all isotopes, is to excite atoms from the 689 nm MOT. This only requires the UV laser as the first photon of the two-photon transition will come from the MOT beams. Typically, we manually scan the UV laser frequency by changing the voltage to the seed PZT with the laser unlocked. While monitoring the number of atoms at the end of the 689 nm MOT, we can identify the approximate position of the line and note the wavelength that is read on the wavemeter. We then find the transmission mode of the transfer cavity which allows us to lock the laser to as close to that value as possible and scan the laser using the double pass AOM as usual. This allows determination of the line position to MHz accuracy. Finally, to get the most accurate spectra, we use a low temperature sample in the ODT excited using our typical two-photon excitation scheme.

Using these techniques, we have successfully found eleven Rydberg levels in the  $ns^3S_1$  Rydberg series of  $^{84}\text{Sr}$ . Combining our measurements of the photon energy required to excite the transition with previous measurements of the ionization energy and energy of the  $^3P_1$  state [37], we are able to extract an accurate measurement of the

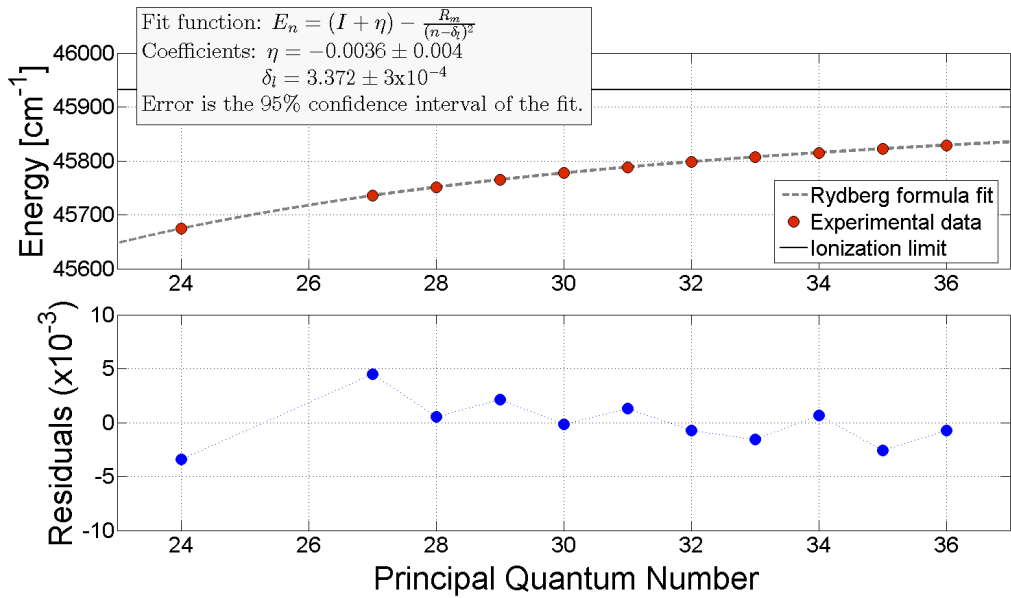


Figure 2.11 : Measurement of the quantum defect of the  $ns^3S_1$  Rydberg series in Sr.

The observed energies are fit extremely well using the Rydberg formula.

quantum defect. As shown in figure 2.11, we obtain an excellent fit and our measured result agrees very well with the prediction of 3.371 from [21]. The dominant source of uncertainty in our measurement is from our wavemeter, which we use to measure the energy of the 638 nm (which is then up converted to our 319 nm) photon. Using our fit value now usually gives us an even better starting point from which to look for a new resonance, greatly reducing the amount of time we need to spend hunting. As seen in the data, the excellent fit to the Rydberg formula shows no evidence of perturbations of this Rydberg series within the range of principal quantum numbers we have measured. For the interested reader, below is a table listing the measured energies for convenience.

Principal Quantum Number	Total Energy [ $cm^{-1}$ ]
24	45674.289
27	45735.626
28	45751.260
29	45765.105
30	45777.416
31	45788.418
32	45798.284
33	45807.169
34	45815.201
35	45822.478
36	45829.101

Table 2.1 : Experimentally measured energies of selected levels of the  $ns^3S_1$  Rydberg series of  $^{84}\text{Sr}$ .

## Chapter 3

### Ultralong-Range Rydberg Molecules

#### 3.1 Introduction

The first experiment we will discuss is the study of ultralong-range Rydberg molecules. This work was originally performed over a year ago and through fruitful collaboration with a number of theorists has resulted in the following submitted paper which I will include here verbatim. At the time of this writing, the paper is under review.

For the work presented in the paper, all experimental work was performed by myself and Jim Aman under the supervision of Drs. Killian and Dunning. All theoretical calculations have been carried out by our collaborators, Drs. Yoshida, Burgdorfer and Sadeghpour. The actual writing of the paper has been a shared duty, with the introduction, experimental details and conclusion written collaboratively by myself and Dr. Killian, figures prepared by Jim Aman, and the theory section written by Drs. Yoshida and Sadeghpour.

## 3.2 Submitted Publication: Ultralong-Range Rydberg Molecules in a Divalent-Atomic System

### 3.2.1 Abstract

We report the creation of ultralong-range  $\text{Sr}_2$  molecules comprising one ground-state  $5s^2 \text{}^1\text{S}_0$  atom and one atom in a  $5sns \text{}^3\text{S}_1$  Rydberg state for  $n$  ranging from 29 to 36. Molecules are created in a trapped ultracold atomic gas using two-photon excitation near resonant with the  $5s5p \text{}^3\text{P}_1$  intermediate state, and their formation is detected through ground-state atom loss from the trap. The observed molecular binding energies are fit with the aid of first-order perturbation theory that utilizes a Fermi pseudopotential with effective  $s$ -wave and  $p$ -wave scattering lengths to describe the interaction between an excited Rydberg electron and a ground-state Sr atom.

### 3.2.2 Main Body

Low-energy scattering of the nearly free, excited electron in a Rydberg atom from a ground-state atom can bind the two atoms into an ultralong-range Rydberg molecule [43, 44]. The resulting internuclear spacing is on the order of the size of the Rydberg atom, which scales with the principal quantum number,  $n$ , as  $n^2$  and can exceed one micrometer. This class of molecules has attracted significant attention because it demonstrates a new mechanism for chemical bonding and the molecules possess surprising features, such as the presence of a permanent electric dipole moment, even in the homonuclear case [24]. Here, we report the creation and theoretical description of ultralong-range  $\text{Sr}_2$  molecules involving a  $5sns \text{}^3\text{S}_1$  Rydberg atom.

Ultralong-range molecules were originally predicted theoretically [43] and were

subsequently observed in Rb [44] and Cs [45]. The original observations were of dimers involving spherically symmetric  $S$  Rydberg states [44], but now measurements have been extended to anisotropic  $P$  [46, 47] and  $D$  [48, 49] Rydberg states and to molecules comprising one Rydberg atom and as many as four ground state atoms [50].

There has been increasing interest in ultracold Rydberg gases of alkaline-earth metal atoms because of several new possibilities introduced by their divalent electronic structure. The principal transition of the Rydberg core is typically in the visible range and can be used to drive auto-ionizing transitions [51], to image Rydberg atoms or ions [22], and to provide oscillator strength for magic-wavelength optical trapping of Rydberg atoms [52]. Doubly excited states serve as strong perturbers of Rydberg states, creating a much richer assortment of electronic configurations than found in alkali-metal atoms. The existence of triplet and singlet excited levels provides many Rydberg series, giving access to attractive and repulsive interactions [21]. Two-photon excitation to triplet Rydberg levels via the intermediate  $^3P_1$  state, as used here, can also reduce the overall decoherence from light scattering for a given strength of optical coupling to the Rydberg level as compared to two-photon transitions available in alkali-metal atoms [13]. The results reported here represent the first experiments involving ultracold Rydberg atoms excited via intermediate triplet excited states.

Within the framework of a two-active-electron approximation, one of the two valence electrons can be excited to a Rydberg state. The interaction between the excited Rydberg electron and a neighboring ground-state atom can be described using the Fermi pseudopotential [53, 54]

$$\begin{aligned}
V_{pseudo}(\mathbf{r}_1, \mathbf{r}_2, \mathbf{R}) = & \sum_{i=1}^2 \frac{2\pi\hbar^2 A_s[k(\mathbf{R})]}{m_e} \delta(\mathbf{r}_i - \mathbf{R}) \\
& + \frac{6\pi\hbar^2 A_p^3[k(\mathbf{R})]}{m_e} \vec{\nabla} \delta(\mathbf{r}_i - \mathbf{R}) \vec{\nabla},
\end{aligned} \tag{3.1}$$

where  $\mathbf{r}_i$  and  $\mathbf{R}$  specify the positions of the Rydberg-atom valence electron and ground-state atom, respectively, measured from the Rydberg core. The momentum dependent  $s$ -wave and  $p$ -wave scattering lengths are  $A_s(k)$  and  $A_p(k)$ . The Rydberg-electron momentum in a semiclassical approximation is  $\hbar k(\mathbf{r}) = \sqrt{2m_e(e^2/(4\pi\varepsilon_0\mathbf{r}) - E_b)}$ , where  $E_b$  is the binding energy of the unperturbed Rydberg atom. This approximation is justified for highly excited  $^3S_1$  Rydberg states for which the hydrogenic approximation is valid at large  $r$ . Since only one of the two valence electrons interacts strongly with the ground-state atom, the molecular potential can be calculated using effective one-electron wavefunctions similar to alkali atoms. The electron-electron interaction contributes to the quantum defect affecting the behavior of the wave function at large  $r$ . When the molecular potential forms an attractive well, ground-state atoms can be bound to a Rydberg atom yielding a Rydberg molecule.

The creation of ultralong-range molecules requires ultracold temperatures so that thermal energies are lower than their small binding energies ( $\sim 10$  MHz). Also, high-density samples are necessary to ensure a sizeable probability of finding two atoms with separations less than the radial extent of a Rydberg electronic wavefunction. We obtain these conditions using  $^{84}\text{Sr}$  atoms confined in an optical dipole trap (ODT). This isotope has collisional properties favorable for evaporative cooling and the creation of high phase-space-density samples [55]. Details of the cooling and trapping are given in Ref. [27].

At the start of the excitation time, the atoms are held in a pancake-shaped ODT formed by two crossed 1064-nm laser beams both having horizontal and vertical waists of about  $370\text{ }\mu\text{m}$  and  $40\text{ }\mu\text{m}$  respectively. The trap oscillation frequencies are 12 and 158 Hz. Typically  $7 \times 10^5$  atoms are trapped at a temperature of 200 nK yielding a peak density of  $\rho = 2.7 \times 10^{12}\text{ cm}^{-3}$ . This corresponds to an average interparticle spacing of  $1/\rho^{1/3} = 0.7\text{ }\mu\text{m}$ , which is about  $10\times$  the distance from the nucleus to the outer lobe of the Rydberg electron wave function  $2n^{*2}a_0 \simeq 75\text{ nm}$  for  $n = 30$  and  $n^* = n - \delta$ . We determine the  $5sns\text{ }^3S_1$  state quantum defect  $\delta = 3.372 \pm 0.001$  by fitting observed Rydberg lines between  $n = 24$  to 36, and this value agrees well with the value  $\delta = 3.371$  from Ref. [21].

Atoms are promoted to Rydberg states through two-photon  $5s^2\text{ }^1S_0$ - $5s5p\text{ }^3P_1$ - $5sns\text{ }^3S_1$  excitation. The 689 nm laser for the first step is detuned 170 MHz to the blue of the intermediate state to avoid scattering from the atomic line and associated molecular resonances. Rydberg states with  $n = 29 - 36$  are reached with photons at 319 nm generated by frequency doubling the red output of a fiber-based optical parametric oscillator laser. Approximately 200 mW of UV power is available. The intensities of the red and UV light on the atoms are  $2.2 \times 10^3\text{ W/m}^2$  and  $2.3 \times 10^5\text{ W/m}^2$  respectively. The UV and 689 nm lasers co-propagate with orthogonal linear polarizations. This configuration excites a superposition of  $m = +1$  and  $m = -1\text{ }^3S_1$  Rydberg states.

The frequency of the UV light is controlled by locking the 638 nm fundamental to an optical cavity stabilized to the 689 nm laser, which is locked to the  $5s^2\text{ }^1S_0$ - $5s5p\text{ }^3P_1$  atomic transition. The UV frequency is scanned using an acousto-optic modulator in a double-pass configuration in the path of the 638 nm light en route to the stabilization cavity. The excitation time is precisely controlled using an acousto-optic modulator

on the 689 nm beam, while the UV light is controlled by a slower mechanical shutter. After excitation, the atoms are released from the trap and the ground-state atom population is measured with time-of-flight absorption imaging on the  $5s^2 \ ^1S_0$ - $5s5p \ ^1P_1$  transition at 461 nm. Excitation to atomic Rydberg or molecular levels is detected as ground-state atom-loss. The exposure time is held constant for the molecular spectrum for a given quantum number and is approximately  $\sim 2\text{s}$ . This results in approximately 50% peak loss for excitation to the most deeply bound molecular level. For atomic resonances (data not shown), 50% peak loss is obtained for  $\sim 10\text{ms}$  excitation. The ODT is left on during excitation, and we assume the AC Stark shift is the same for the atomic and molecular transitions in our quoted results.

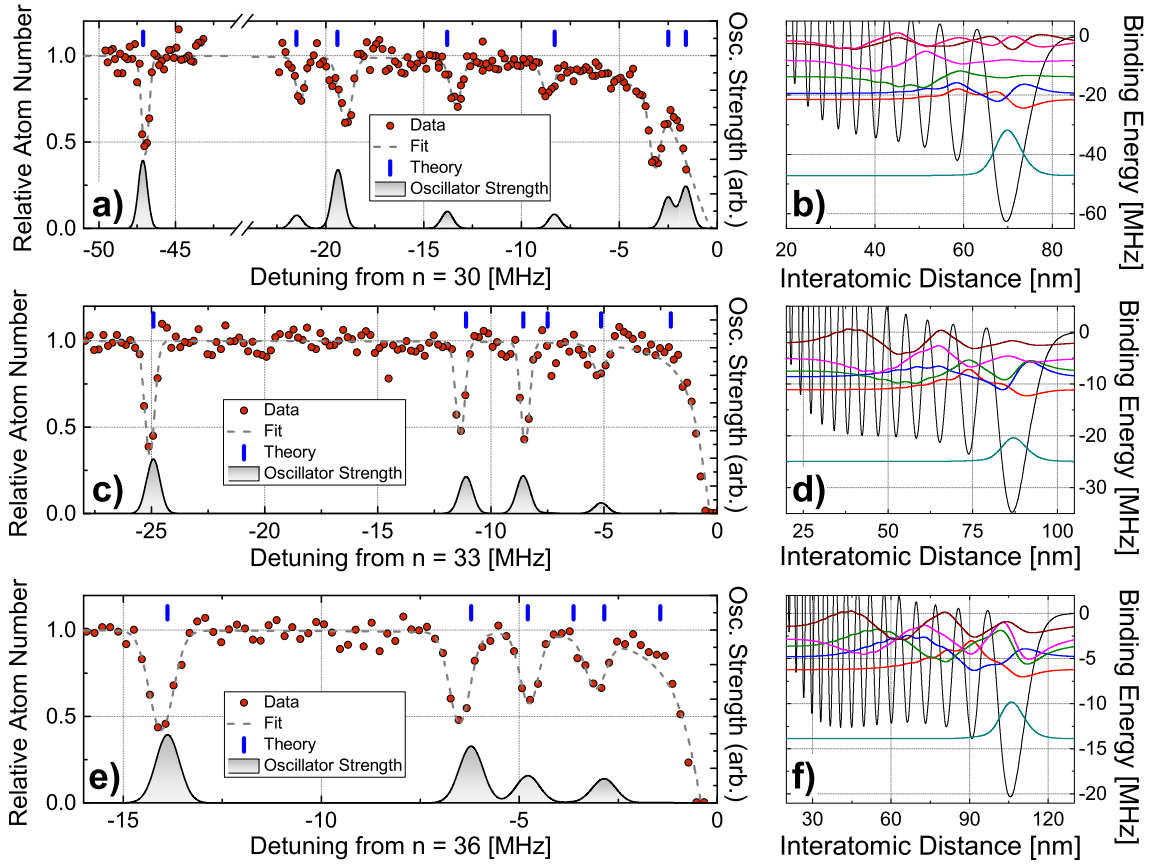


Figure 3.1 : (Left) Atom-loss spectra and (Right) calculated potentials and wavefunctions,  $R\chi_\nu(R)$ , for  $n=30$  (top), 33 (middle), and 36 (bottom). The bars at the top of the molecular spectra indicate the positions of the theoretically-predicted binding energies of states bound by  $> 1$  MHz and the curves at the bottom indicate their calculated excitation strength. The origin of each frequency axis is set to the center of the atomic excitation spectrum (see text).

Typical atom-loss spectra are shown in Fig. 3.1. The spectra are relatively simple because of the closed-shell  $^1S_0$  electronic-ground state and lack of nuclear spin for  $^{84}\text{Sr}$ . Atom loss is an indirect method of detecting excitation as compared to the

traditional technique of pulsed-field ionization and charged-particle detection [44, 45, 46, 48, 50], but it can still yield a high signal-to-noise ratio. A comprehensive understanding of the decay channels of ultralong-range molecules is still lacking, but it is clear that a large fraction of excitations should lead to measurable ground-state atom loss. Fluorescent decay after either atomic or molecular excitation has a sizable probability, approximately two-thirds, of creating long-lived  $^3P_0$  or  $^3P_2$  atoms. Such atoms may remain trapped but they are invisible to absorption imaging. The recoil energies of  $\hbar^2/2m_{84}\lambda_{689}^2k_B = 0.24\ \mu\text{K}$  and  $\hbar^2/2m_{84}\lambda_{320}^2k_B = 1.1\ \mu\text{K}$  are smaller than the  $1.9\ \mu\text{K}$  depth of the ODT. However, collisional processes involving ground-state atoms and tunnelling to small internuclear separation can reduce the molecular lifetime significantly compared to the atomic lifetime for conditions similar to ours [56]. Such tunnelling should release enough energy to eject one or both atoms from the trap. For atomic excitation, it is possible that the density of Rydberg atoms becomes high enough for inelastic Rydberg-Rydberg collisions to lead to atom loss [57]. The density of molecules, however, is low enough that such processes are negligible.

The threshold for the molecular-binding energy for each principal quantum number is determined by measuring the resonance position for atomic excitation to the  $5sns\ ^3S_1$  state. This is done with a 10 ms excitation time to avoid saturating the transition, and it results in a  $\sim 800\ \text{kHz}$  FWHM linewidth, which is likely limited by the UV laser linewidth. For such short excitation times, no molecular transitions are visible. For excitation times on the order of 1 s, however, clearly resolved resonances corresponding to molecular bound states appear to the red of the (highly-saturated) atomic line. No transitions are observed to the blue or further to the red of the regions shown. Data are fit to the wing of a Lorentzian to describe the atomic background

plus a gaussian for each molecular line. Molecular-binding energies are determined by the frequency difference between molecular and atomic lines.

Typical molecular linewidths are 800 kHz FWHM, again limited by the UV laser linewidth. Several spectra were recorded for each principal quantum number, alternating between measurement of atomic and molecular lines. The uncertainties in the molecular line positions with respect to the atomic line are the statistical  $1\sigma$  uncertainties in the mean for each group of measurements. The typical value is  $\pm 150 \text{ kHz}$ . DC Stark shifts of the transitions were measured for  $n = 36$  by applying DC electric fields of up to about 0.5 V/cm. The extracted atomic and molecular DC polarizabilities were equal at our level of precision  $\pm 0.5 \text{ MHz}/(\text{V/cm})^2$  and calculated theoretically to be  $-4.5 \text{ MHz}/(\text{V/cm})^2$ .

For the present range of  $n$  and our relatively low densities, the production rate for trimers is expected to be much lower than for dimers [58, 50] and therefore difficult to detect with our current methods. The most deeply bound level observed for each principal quantum number is assigned to the vibrational ground state of one atom in the potential well formed by the outermost lobe of the Rydberg electron wavefunction. This is confirmed by calculations of the potentials and molecular wavefunctions (Fig. 3.1(Right)), which show that this state is well localized in this well. The more weakly bound levels correspond to vibrationally excited states, which are delocalized across several lobes of the electron probability density.

The electron wave function  $\Psi(\mathbf{r}_1, \mathbf{r}_2)$  of the  ${}^3S_1$  Rydberg atom can be calculated by numerically diagonalizing the Hamiltonian within the two-active-electron model. Spin-orbit interaction is included, but its effects are small [59]. The model potential is fitted to reproduce the measured energy levels in the singlet sector [60], and yields

the quantum defect  $\delta = 3.376$  for  $^3S_1$  states, which agrees well with the more precise measured value. The calculated wave functions for  $^3S_1$  Rydberg states with  $n \sim 30$  are dominated by a single configuration

$$\Psi(\mathbf{r}_1, \mathbf{r}_2) \simeq \frac{1}{\sqrt{2}} (\phi_{5s}(\mathbf{r}_1)\psi_{ns}(\mathbf{r}_2) - \psi_{ns}(\mathbf{r}_1)\phi_{5s}(\mathbf{r}_2)) \quad (3.2)$$

where  $\phi_{5s}(\mathbf{r})$  and  $\psi_{ns}(\mathbf{r})$  are the wave functions of the  $5s$  state for  $\text{Sr}^+$  ions and the Rydberg  $ns$  state for Sr atoms, respectively. The contributions from the other configurations are smaller than 0.01%. Using the first-order perturbative approximation the molecular potential around  $R \simeq 1000$  a.u. can be evaluated

$$V(R) \simeq \frac{2\pi\hbar^2 A_s(k)}{m_e} |\psi_{ns}(\mathbf{R})|^2 + \frac{6\pi\hbar^2 A_p^3(k)}{m_e} |\nabla\psi_{ns}(\mathbf{R})|^2. \quad (3.3)$$

Since the second valence electron in the  $5s$  state is rather localized (i.e.  $\phi_{5s}(\mathbf{r}) \simeq 0$  for  $r > 20$  a.u.), it does not affect the molecular potential at large  $R$  and, therefore,  $V(R)$  becomes similar to that for effective one-electron systems.

By solving the Schrödinger equation associated with the molecular potential, the binding energies and the wave functions for Rydberg molecules are obtained. The effective scattering lengths are taken to be

$$A_s(k) = A_s(k=0) + \frac{\pi}{3}\alpha k^2 \quad A_p(k) = A_p(k=0). \quad (3.4)$$

The measured value,  $\alpha = 186a_0^3$ , is used for the polarizability [61]. It is known [58] that a non-perturbative Green's function calculation correctly reproduces the measured molecular energy levels using the true zero-energy s-and p-wave scattering lengths. Within the first-order perturbative approximation, however, good agreement can be

obtained by considering the scattering lengths as effective fitting parameters. For strontium, while the calculated *s*-wave scattering length is  $A_s(k = 0) = -18 a_0$  [62], an effective scattering length of  $A_s(k = 0) = -13.2 a_0$  for  $n = 30$  to  $-13.3 a_0$  for  $n = 36$  yields good agreement with the measured energy levels, especially the most deeply bound molecular states. Although the depth of the deepest well in the molecular potential linearly scales with  $A_s(k = 0)$  (Eq. 3.3), the additional contribution from *p*-wave scattering becomes non-negligible around the nodes (i.e.  $|\psi_{ns}(\mathbf{R})| \simeq 0$ ) and affects the energies of the weakly bound levels and their density of states. They are optimally fitted using the value of  $A_p(k = 0) \simeq 8.4 a_0$ .

The molecular formation rate can be calculated as  $\Gamma_\nu \propto |\langle \Psi, \chi_\nu | T | \Psi_0, \chi_0 \rangle|^2$  where  $T$  is the transition matrix for two-photon absorption, and  $\Psi_0, \chi_0, \chi_\nu$  are the ground-state-electron wavefunction, the initial state, and the  $\nu$ -th vibrational wavefunction of the Rydberg molecule, respectively. Within first-order perturbation theory, the electronic part of the transition matrix is independent of the molecular states. Therefore, the excitation rate is reduced to the Franck-Condon factor

$$\Gamma_\nu \propto \left| \int dR R^2 \chi_\nu(R) \chi_0(R) \right|^2. \quad (3.5)$$

In the present case  $\chi_0$  can be approximated as the square root of the pair distribution of two unbound ground-state Sr atoms. The latter can be taken to be approximately constant for the large  $R$  values contributing to the integral Eq. 3.5. Using the excitation rate  $\Gamma_\nu$  the excitation spectrum can be derived as  $f(E) = \sum_\nu \Gamma_\nu \delta(E - E_\nu)$ . The spectrum is convolved with a Gaussian distribution associated with the laser linewidth and plotted in Fig. 3.1. The agreement between the measured and calculated spectra is very good. The calculations reveal the existence of more molecular

levels, but their excitation strengths are too weak to detect in the measurements.

Figure 3.2 shows the  $n$  scaling of the observed binding energies together with the calculated values. The binding energies of deeply bound states follow the approximate  $1/(n - \delta)^6$  scaling seen in Rb [50]. Gaps in laser coverage prevented measurement of spectra for  $n = 31$  and  $n = 32$ . Deviations from the scaling are evident for weakly bound states and are clearly seen in high-quality spectra for  $n = 30$ . The energy scaling reflects the scaling of the probability density  $|\psi_{ns}(\mathbf{R})|^2$  of the Rydberg electron at the location of the unperturbed Sr atom. The wave functions of the most deeply bound states for  $29 \leq n \leq 36$  are confined in the most outer well of the molecular potential (Fig. 3.1). Therefore, the corresponding binding energies scale with the depth of the well by  $1/(n - \delta)^6$  as the quantum number  $n$  varies. When the first-excited state of this potential well is nearly degenerate with the lowest energy state of the adjacent well, the coupling between two states yields an energy splitting,  $\Delta$ . If a molecular state confined in a single well for a given  $n$  experiences tunneling to an adjacent well for another value of  $n$ , the molecular energy does not scale with the potential depth showing a deviation  $\sim \Delta$  from the  $1/(n - \delta)^6$  scaling. Such a transition in the wave function is seen for some excited vibrational levels (Fig. 3.1). For example, although the first excited vibrational state's wave function is rather confined within the first two outer wells for the given range of  $n$ , the second-excited state tunnels ever deeper into inner wells as  $n$  increases. Thus the deviation from the scaling is prominent for the latter (Fig. 3.1). Note that data obtained for  $n = 29$  were of inferior quality, but we were able to identify the three lines indicated in Fig. 3.2.

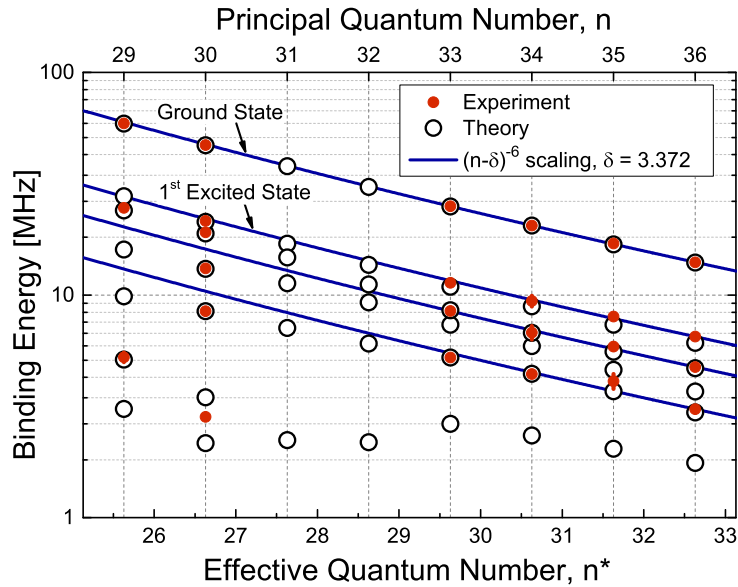


Figure 3.2 : Scaling of observed molecular binding energies, showing  $1/(n-\delta)^6$  scaling for higher quantum numbers and more deeply bound levels.

We have presented the first observation of ultralong-range Rydberg molecules in  $\text{Sr}_2$  formed by photoexcitation to the  $5sns\ ^3S_1$  Rydberg state for  $29 \leq n \leq 36$ . The observed lines are well described using a Fermi pseudopotential approach to calculate perturbative molecular potentials and yield the effective  $s$ -wave and  $p$ -wave  $e^-$ -Sr scattering lengths  $A_s = -13.2a_0$  and  $A_p = 8.4a_0$ .

This work represents the first study of ultralong-range Rydberg molecules in a divalent-atomic system, and it opens new directions in this emerging research area. Doubly excited electronic states give rise to dramatic perturbations of the Rydberg states in divalent atoms. This should lead to new types of ultralong-range molecules with mixed electronic character that arise from degeneracies of pairs of Rydberg levels of different angular momenta. This may also lead to very strong transition strengths

for production of molecules with large dipole moments. If one can form Rydberg molecules with high electronic angular momenta, it might be possible to optically trap them using the oscillator strength of the ionic core [52]. High densities of atoms in metastable triplet levels can be created in these systems [63], allowing the formation of Rydberg molecules in which triplet atoms serve as the “ground-state” atoms. Spectroscopy of these molecules will probe the low-energy scattering of electrons from the metastable states including measuring the electron-triplet scattering length, which should be sensitive to the greater polarizability compared to closed-shell, ground-state atoms.

Detection of ultralong-range molecules with atom loss, as demonstrated here, greatly simplifies the required experimental apparatus compared to charged particle detection, which may open the way for study of these exotic molecules in many other species of atomic gases. The measurements reported here also represent an important step towards future experiments with interacting alkaline-earth Rydberg atoms because molecular excitations represent loss channels that need to be avoided.

### Acknowledgements

Research supported by the AFOSR under grant no. FA9550-12-1-0267, the NSF under grants nos. 1301773 and 1205946, and the Robert A. Welch Foundation under grants nos. C-0734 and C-1844, and by the FWF (Austria) under grant no P23359-N16 and by the SFB-NextLite. The Vienna Scientific Cluster was used for the calculations.

### 3.3 Additional Material

In this section, I will include additional supplemental material that was not included in the paper.

#### 3.3.1 Rydberg Excitation

While described in the text, it is helpful to show the geometry of the system and discuss the details of our method of excitation of Rydberg atoms and molecules. Figure 3.3 shows the relative propagation directions and polarizations of the laser used as well as a simplified level diagram.

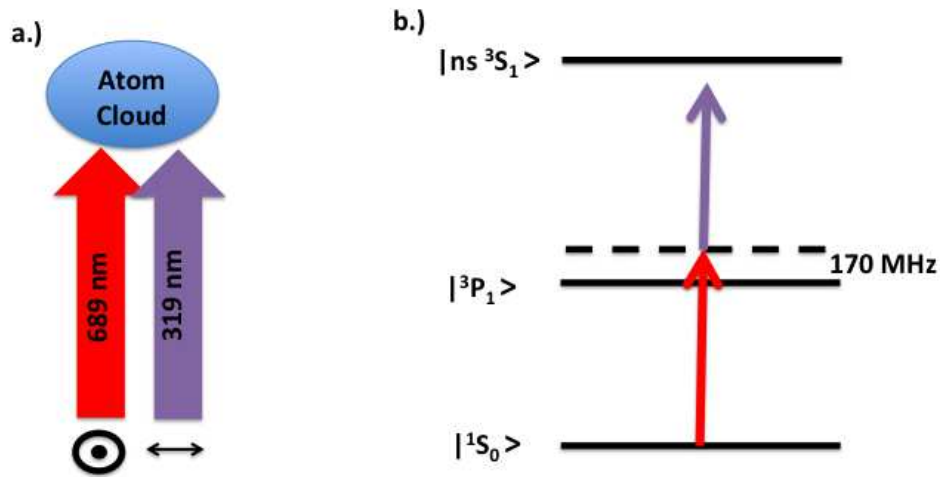


Figure 3.3 : a.) Cartoon layout of geometry used in experiment. 689 nm and 319 nm lasers copropagate with orthogonal linear polarizations. b.) Simplified level diagram of transitions probed in experiment yielding an effective one photon transition to the Rydberg state.

As we see, the lasers are far off resonance with the intermediate state, so we can

think of this as an an effective one-photon transition with an effective Rabi frequency. With a near zero magnetic field, all three  $m_j$  levels of the Rydberg state are degenerate, so by choosing the polarization we can couple to any  $m_j$  state at the same frequency. We use copropogating laser beams with mutually orthogonal linear polarizations. By choosing a quantization axis aligned with one of the lasers polarizations, the polarization of the other laser can be described as an equal superposition of left and right circular polarization. Therefore our lasers will couple to the  $m_j = \pm 1$  states equally.

At first glance, this seems like a strange choice as typically we are interested in exciting only a single Rydberg level. However, with copropogating beams and linear polarization, this is the only choice that will work. The linear polarization of the 689 nm laser will drive the transition  ${}^1S_0(m_j = 0) \rightarrow {}^3P_1(m_j = 0)$ . With aligned polarizations, the 319 nm laser would unsuccessfully try to drive the  ${}^3P_1(m_j = 0) \rightarrow ns {}^3S_1(m_j = 0)$  transition, which has a matrix element of 0. Owing to optical access considerations at the time of the experiment, using copropogating beams made the best use of space and therefore crossed polarizations were used to yield a non-zero coupling to the Rydberg state.

One downside of simultaneously exciting to  $m_j = \pm 1$  states is that both are sensitive to magnetic fields and will experience equal and opposite shifts. Non-zero magnetic fields can broaden and eventually split the measured line leading to difficulties in accurately measuring the line center. However, as we see in figure 3.4, even in this configuration we are able to obtain narrow linewidth spectra which confirms that the magnitude of stray magnetic fields in the experiment is small. As described in the main body of the text, the width measured here is consistent with the linewidth

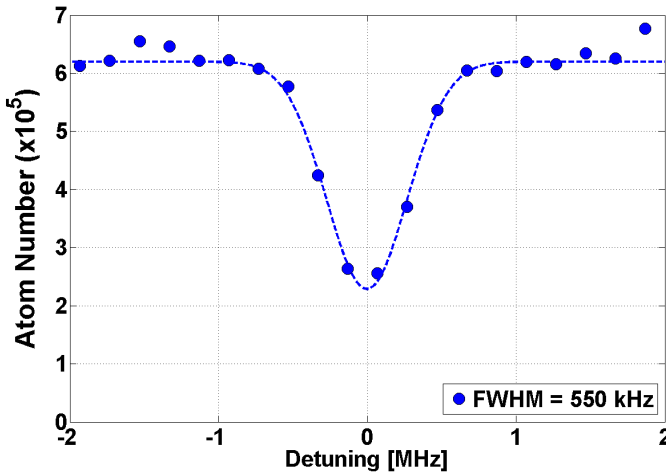


Figure 3.4 : Example of a narrow atomic spectra taken during the course of the Rydberg molecule experiment. The obtained spectrum is well described by a gaussian with a full width at half max (FWHM) of 550 kHz. This is limited by the linewidth of the 319 nm laser, and gives confidence that stray magnetic fields do not cause significant problems in our magnetically sensitive excitation scheme.

of the 319 nm laser at the time of the experiment (it has since been improved with the aid of our high bandwidth lock described in chapter 2).

### 3.3.2 Stark Shift Measurements

As discussed in chapter 2, our control over electric fields is limited, so in absolute terms it is difficult to extract the DC polarizability of a Rydberg state. However, for the purposes of this work, it is sufficient to measure the relative polarizabilities of the Rydberg atoms and molecules.

To measure the DC polarizability, we excite Rydberg atoms and molecules in varying electric fields to see how the resonance position shifts with the applied field.

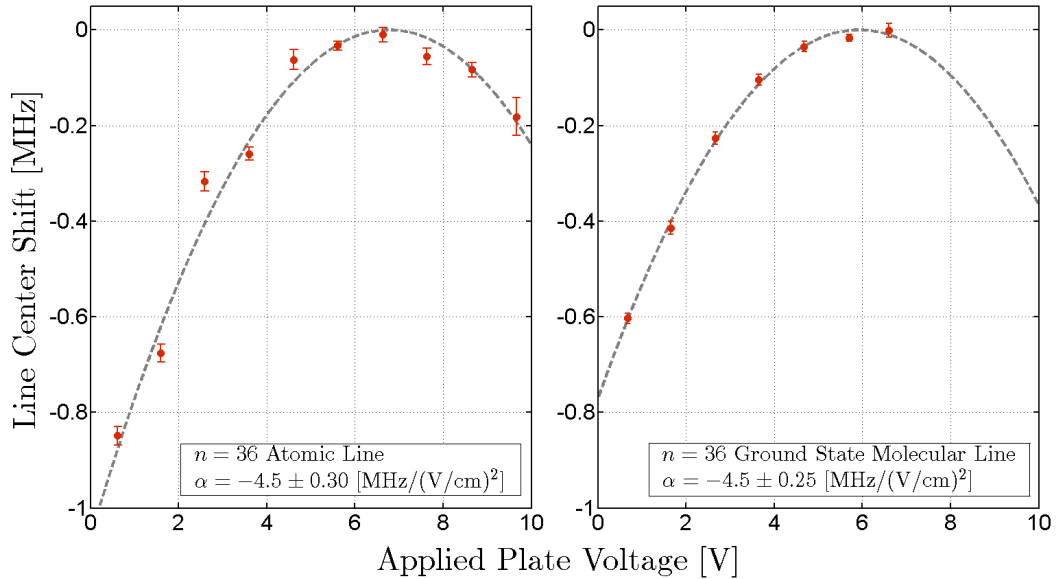


Figure 3.5 : Measurement of the polarizability of an  $n = 36$  Rydberg atom and a ground state Rydberg molecule at  $n = 36$ . Both show the same polarizability within experimental uncertainty.

From simple modeling of the fields in the chamber done by Francisco Camargo using the software SimIon, we know that the electric field varies linearly with the applied voltage with a conversion factor of  $0.9 \text{ V}/(\text{V/cm}^2)$ . This disagrees with a calibration using the calculated DC polarizability of the  $36s^3S_1$  state, which yields a conversion factor of  $1.16 \text{ V}/(\text{V/cm}^2)$ . For our measurement here, we use the latter calibration.

Figure 3.5 shows that we see the expected quadratic dependence of both the atomic and ground state molecular resonance with applied electric field. It should be noted that zero field does not correspond to zero voltage. As shown in figure 2.10, during the excitation time the MOT coils are held at a non-zero potential in this case of 5.6 V. From geometry, we see that the zero of the electric field should occur near where

the voltage on the electric field plate is equal to the voltage on the MOT coils. Since our calibration uses the calculated value of the polarizability, this does not constitute an independent measurement of the absolute value of the polarizability. But, within the error of the fit, the atom and molecular polarizabilities are equal.

## Chapter 4

# Rydberg Blockade Effects on Autler-Townes Spectra in an Ultracold Dense Gas

### 4.1 Introduction

The study of ultracold gases of Rydberg atoms has grown into a vast field in recent years. As discussed in the first chapter of this thesis, this is driven by the many novel effects and potential applications that may arise from the strong, long-range interactions between Rydberg atoms and the Rydberg-blockade phenomenon [64, 65, 4]. Major themes in this research include quantum information [66], quantum optics (e.g. [67]), dynamics of driven dissipative systems [14, 68, 69, 70, 71, 72], and many-body physics with long-range interactions. The latter category includes phase transitions to strongly correlated classical crystals [73, 11, 12, 74], realization of spin-models on optical lattices [75, 76], and phenomena in bulk gases such as three-dimensional solitons [15], roton-maxon excitations [13], and super-solids [18, 11, 19, 13]. The use of Rydberg dressing to control the strength and character of Rydberg interactions [77, 78, 25, 26] figures prominently in most of these proposals.

In spite of some prominent advances [74, 26], in general the novel many-body states predicted for strongly interacting Rydberg gases remain elusive because of large loss and dephasing rates observed experimentally [79, 25]. Much remains to be understood, especially on how complex dynamics in dense Rydberg gases (beyond

the ideal quantum optics description) affect these systems, such as plasma formation [80, 81, 79], non-adiabatic level-crossings at short-range [71], and superradiance [82, 83, 84, 85]. The correct description of Rydberg blockade and Rydberg dressing in very dense gases with strong Rydberg excitation is also an active area of study [78, 25].

Many of these open questions are probed with experiments studying quantum interference effects in the optical excitation of interacting, ultracold Rydberg gases, including coherent population trapping (CPT) [86, 87], electromagnetically induced transparency (EIT) [83, 88, 89, 87], and Autler-Townes (AT) spectra [90, 91, 92]. This is important background for the work presented in this thesis, and I will discuss the details of these various experiments later in this chapter.

## 4.2 Theoretical Groundwork

### 4.2.1 Interaction Effects

In chapter 2, we discussed the classic picture of Autler-Townes splitting. For our observable of ground-state atom loss, we found two symmetric loss peaks split by the Rabi frequency of the strong driving field,  $\Omega_{12}$ . However, for the case of ultracold Rydberg atoms in a dense gas, this solution will certainly not always be the case. The natural question that arises is: How do interactions modify the spectra? To answer this question, need to modify our treatment.

In the absence of interactions and decoherence, it was sufficient to write down the Hamiltonian and diagonalize it to find the eigenstates. We did this using only two states, but it is possible to extend that treatment to the three level problem. However, interactions and decoherence need to be handled separately and we turn to

solving for the time evolution of the density matrix,  $\rho$ . Formally, non-unitary terms such as spontaneous decay and decoherence can be described using the Lindblad superoperator,  $\mathcal{L}(\rho)$ . The exact form of  $\mathcal{L}(\rho)$  depends on the problem at hand, however in general one is able to use this method to solve for the dynamics of the density matrix by solving the master equation,

$$\dot{\rho} = \frac{i}{\hbar}[\rho, H] + \mathcal{L}(\rho). \quad (4.1)$$

For our system, including spontaneous decay, finite laser linewidths, and a modified mean-field treatment of energy-level-shift and dephasing terms affecting the Rydberg state,  $|2\rangle$ , this yields the following system of equations known as the optical Bloch equations [93, 85].

$$\begin{aligned} \dot{\rho}_{00} &= \Gamma_{10}\rho_{11} - \tilde{\Omega}_{01}Im(\rho_{01}) \\ \dot{\rho}_{11} &= -\Gamma_{10}\rho_{11} + \Gamma_{21}\rho_{22} + \tilde{\Omega}_{01}Im(\rho_{01}) - \tilde{\Omega}_{12}Im(\rho_{12}) \\ \dot{\rho}_{22} &= -(\Gamma_{21} + \Gamma_{2Loss})\rho_{22} + \tilde{\Omega}_{12}Im(\rho_{12}) \\ \dot{\rho}_{01} &= -\left(\frac{\Gamma_{10} + \Gamma_1}{2} + i\Delta_{01}\right)\rho_{01} - \frac{i\tilde{\Omega}_{01}}{2}(\rho_{11} - \rho_{00}) + \frac{i\tilde{\Omega}_{12}}{2}\rho_{02} \\ \dot{\rho}_{12} &= -\left[\frac{\Gamma_{10} + \Gamma_{21} + \Gamma_{2Loss} + \Gamma_{2Laser} + \Gamma_{2Ryd}(n)\rho_{22}}{2} + i(\Delta_{12} - V_{Ryd}(n)\rho_{22})\right]\rho_{12} \\ &\quad - \frac{i\tilde{\Omega}_{12}}{2}(\rho_{22} - \rho_{11}) - \frac{i\tilde{\Omega}_{01}}{2}\rho_{02} \\ \dot{\rho}_{02} &= -\left[\frac{\Gamma_1 + \Gamma_{21} + \Gamma_{2Loss} + \Gamma_{2Laser} + \Gamma_{2Ryd}(n)\rho_{22}}{2} + i(\Delta_{01} + \Delta_{12} - V_{Ryd}(n)\rho_{22})\right]\rho_{02} \\ &\quad + \frac{i\tilde{\Omega}_{12}}{2}\rho_{01} - \frac{i\tilde{\Omega}_{01}}{2}\rho_{12} \end{aligned} \quad (4.2)$$

where  $\Gamma_{ij}$  denotes the spontaneous decay rate from  $|i\rangle \rightarrow |j\rangle$ ,  $\Gamma_{2Loss}$  denotes spontaneous decay from  $|2\rangle$  that results in a loss of atoms, and  $\Gamma_1$  and  $\Gamma_{2Laser}$  are the

dephasing rates due to laser linewidth of  $|1\rangle$  and  $|2\rangle$ , respectively. Note that we have defined  $\tilde{\Omega}_{ij} = \Omega_{ij}\Theta(\tau_{ij} - t)$  using the Heaviside theta function to accommodate non-simultaneous laser turn off times. For visualization purposes, a simplified level diagram, including all terms except dephasing, is included in figure 4.1.

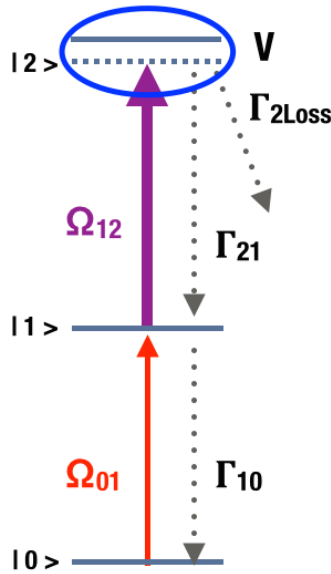


Figure 4.1 : Simplified level diagram of the three level system under consideration.

$V = V_{Ryd}(n)\rho_{22}$  describes energy level shifts and  $\Gamma = \Gamma_{2Ryd}(n)\rho_{22}$  describes dephasing. As written, the influence of each will depend on the density of Rydberg atoms through the factor  $\rho_{22}$ , but to first understand the effects of these terms on the spectra, let's ignore that and see what happens when  $V$  and  $\Gamma$  are constants. In the right panel of figure 4.2, we see that increasing  $V$  behaves in a qualitatively similar way to making  $\Delta_{12} \neq 0$ . This makes sense as this term shifts the energy of  $|2\rangle$ . It is important to note that this term can give rise to loss at two-photon resonance ( $\Delta_{01} = 0$ ), however, this loss is strongly suppressed. In our system, loss

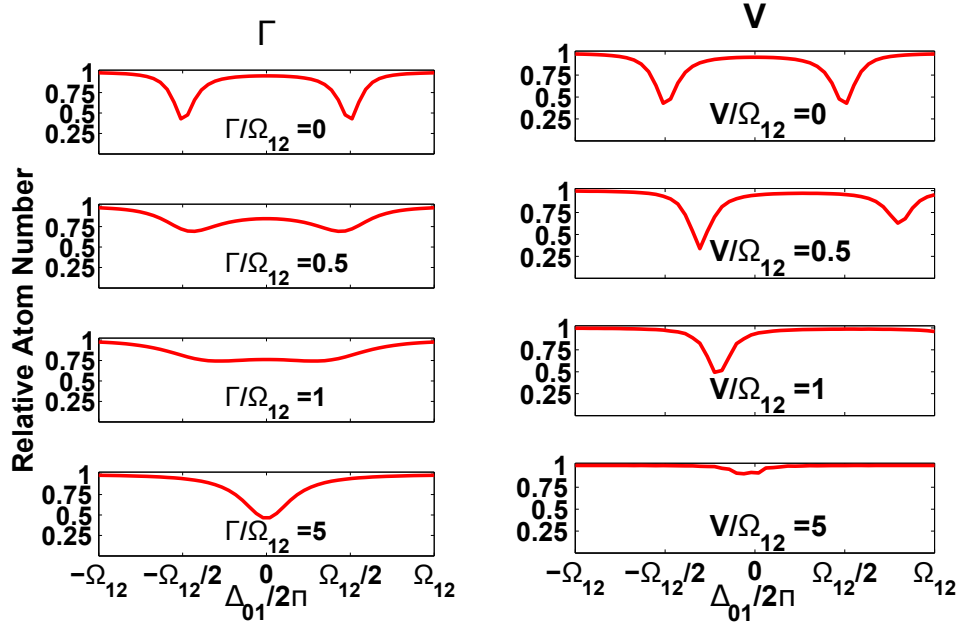


Figure 4.2 : Effects of a constant  $V$  or  $\Gamma$  on Autler-Townes spectra. While increasing  $V$  causes asymmetry in the strength of the peaks and shifts their position, increasing  $\Gamma$  causes a broadening and eventually a strong loss feature at zero detuning.

only occurs from the Rydberg state, as previously discussed, and for the eigenstate with an eigenenergy moving closer to two-photon resonance, the amount of Rydberg character in the state diminishes.

In the left panel, we see the effects of increased dephasing are markedly different from those of  $V$ . There is no apparent shift in the positions of the loss features, and at low values of  $\Gamma$  only a broadening of the peaks is evident. On the other hand, for large values of  $\Gamma$ , a very strong loss feature arises at two-photon resonance implying a large fraction of Rydberg character. This can be understood in the limit of extremely large dephasing, where one can think of the intermediate state as being coupled to

a broad, decaying continuum. In this picture, excitation to the intermediate state results in loss without introducing the Autler-Townes structure. From these plots, it is evident that the effects of  $V$  and  $\Gamma$  are different in Autler-Townes spectra, and this fact allows us to disentangle the two as we look at experimental spectra.

#### 4.2.2 Rydberg-Rydberg Interactions

To go forward with our analysis, we need to consider the functional form of Rydberg-Rydberg interactions. A detailed treatment of this problem can be found in [4], but for our purposes it is sufficient to discuss the highlights. In the limit of a large separation ( $\vec{R} = R\vec{n}$ ) between two atoms, the interaction term of the Hamiltonian can be written as

$$H_{12} = \frac{\vec{\mu}_1 \cdot \vec{\mu}_2 - 3(\vec{\mu}_1 \cdot \vec{n})(\vec{\mu}_2 \cdot \vec{n})}{4\pi\epsilon_0 R^3} \quad (4.3)$$

where  $\mu_i$  the dipole moment of atom  $i$ . This Hamiltonian will only connect initial and final states of two atoms if the initial and final state of each atom individually are connected according to dipole selection rules.

Let us first consider a two-atom system in a state  $|r_1, r_2\rangle$  close in energy to a single state  $|r'_1, r'_2\rangle$  connected by matrix elements of equation 4.3. We can rewrite the Hamiltonian in the convenient form

$$H_{int} = \begin{pmatrix} \hbar\Delta & V_{dip} \\ V_{dip}^\dagger & 0 \end{pmatrix} \quad (4.4)$$

where we have defined  $V_{dip} = \langle r'_1, r'_2 | H_{12} | r_1, r_2 \rangle$  and  $\hbar\Delta = (E_{r'_1} + E_{r'_2}) - (E_{r_1} + E_{r_2})$  is the Förster energy defect with  $E_r$  denoting the energy of the single atom Rydberg state. As we see,  $V_{dip}$  will couple states of opposite parity and its value is related

to  $C_3$ . If for example,  $|r_1, r_2\rangle = |n_1S, n_2P\rangle$ , then  $|r'_1, r'_2\rangle = |n_2P, n_1S\rangle$  and  $\Delta = 0$ . This leads to a strong flip-flop interaction. If  $|r_1, r_2\rangle = |n_1S, n_1S\rangle$ , then we may have  $|r'_1, r'_2\rangle = |n_2P, n_3P\rangle$  and  $\Delta \neq 0$ .

It is clear that the atomic pair states we have mentioned are not the eigenstates of the Hamiltonian, but by diagonalizing we find the position dependent eigenvalues

$$E_{\pm}(R) = \frac{\hbar\Delta \pm \sqrt{(\hbar\Delta)^2 + 4V_{dip}(R)^2}}{2}. \quad (4.5)$$

For the case of two interacting s-state Rydberg atoms in the limit of small separation or small detuning, this reduces to  $E_{\pm} = \pm C_3/R^3$ , resulting in dipole-dipole interactions. However, for large separations, a Taylor expansion of equation 4.5, or application of second-order perturbation theory, shows that the leading contribution to the energy level shift is of van der Waals type,  $E_- = \frac{-(C_3/R^3)^2}{\hbar\Delta} = -C_6/R^6$ . As can be seen, the sign of the interaction is then dependent on the sign of the Förster energy defect, which depends on the the energy of the nearest level. The spacing of Rydberg levels comes down to knowing the quantum defect of the Rydberg states involved, so at a simple level, the quantum defects tell us all we need to know.

To illustrate this further (and see where this treatment fails), let's consider a few examples of atomic species of Rydberg atoms. Rubidium has a quantum defect of 3.131 for s states and 2.655 for p states [94] which yields a negative Förster energy defect for  $|ns, ns\rangle \rightarrow |(n+3)p, (n-3)p\rangle$  causing repulsive van der Waals interactions for the s states. However, it should be noted that due to the presence of a p wave shape resonance, interactions between Rb Rydberg atoms are more complicated than this simple treatment. For Sr, we can consider both the singlet and triplet Rydberg series. In the singlet series the  ${}^1S_0({}^1P_1)$  quantum defects are 3.269(2.729)[21] that

yields a positive Förster energy defect and attractive interactions between s states. The triplet series, with quantum defects for the  $^3S_1(^3P_j)$  of 3.371(2.88)[21], we again obtain repulsive interactions. For the triplet s states of Sr, the energy defect is smaller than that for Rb, overall yielding a larger value of  $C_6$  for the same principal quantum number. Also in the case of Sr, there is no p wave shape resonance so this description accurately captures the interactions between Sr Rydberg atoms. As a final example, we note the complicated case of Cs. With an s state quantum defect of 4.049 [95], there is a near degeneracy of  $|ns\rangle$  and  $|(n+4)g\rangle$  yielding mixing of levels. As such interactions between Cs Rydberg s states are very complicated and beyond the capabilities of this simple approach.

#### 4.2.3 Mean-Field Theory and Beyond

With the basic machinery and some intuition in place to treat level shifts and dephasing, we now will develop an approach to appropriately handle these interactions for an ultracold Rydberg gas. The Rydberg atoms under discussion are s-state Rydberg atoms, with repulsive isotropic van der Waals interactions,  $V = \frac{C_6}{\hbar} \frac{1}{|r|^6}$ .

Looking at this form, from dimensional analysis we expect a scaling of  $V \propto \rho^2$ , where  $\rho$  is the density. However, to get quantitative agreement we will need to go further. A natural first step is to apply mean field theory.

In mean-field theory, one approximates the real system of many interacting atoms by simplifying the problem to one atom interacting with some external potential that captures the average effect of the other particles. Formally, the effective field is calculated as

$$V_{eff} = \int d\mathbf{r}' V(\mathbf{r}') \langle n_2(\mathbf{r}') \rangle \quad (4.6)$$

Since our system is translationally invariant,  $\langle n_2(\mathbf{r}') \rangle$  is just the average density of Rydberg atoms, and can be taken out of the integral. This simplifies the problem and allows us to solve it.

$$\begin{aligned} V_{eff} &= \int_0^\infty d\mathbf{r} \frac{C_6}{\hbar r^6} \langle n_2(\mathbf{r}) \rangle \\ &= \frac{C_6 \rho_{22} \rho}{\hbar} 4\pi \int_0^\infty dr r^{-4} = \infty \end{aligned} \quad (4.7)$$

Unfortunately, this solution is not very useful to us. The integral diverges at short range and this mean-field approach fails to provide a finite prediction. Additionally, we will see in the following sections that our data does not agree with the  $\rho^2$  scaling expected from dimensional analysis.

Mean-field theory is a powerful technique with widespread use in the field, so it is worth discussing why it fails in the case of interacting Rydberg gases. The first and most obvious is the short-range divergence of the above integral. In this case, it is the particular form ( $\frac{1}{r^6}$ ) of the interactions which causes the problem. In some sense, this is not too concerning for us. At short-range, van der Waals interactions do not accurately capture the physics of interacting Rydberg atoms. Other Rydberg levels can contribute to the interatomic potentials, so the real potential might not diverge as it approaches  $r = 0$ . A more subtle and interesting reason mean-field fails is the effect of correlations. In applying mean-field, we completely wash out the effect of correlations when we try to calculate the effective potential. For strongly interacting Rydberg gases, we know Rydberg blockade plays an important role when interparticle spacings are on the order of the blockade radius. This adds in an important length scale for correlations to the system that is not accounted for in a mean field treatment. If we are to have any hope in describing this complicated system, we need a more

sophisticated approach.

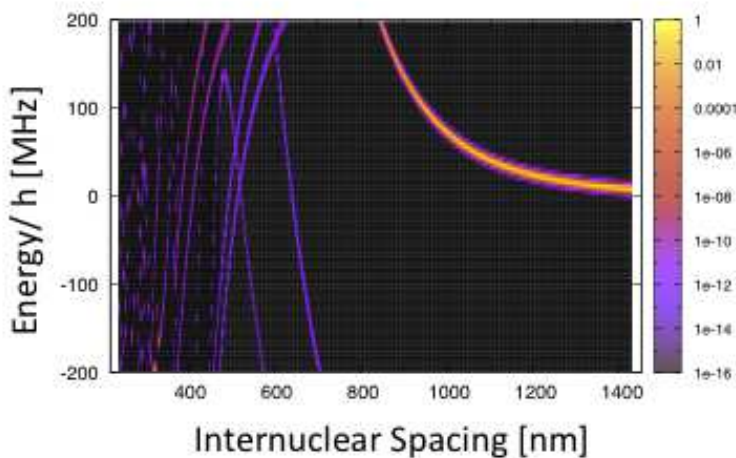


Figure 4.3 : Excitation strength for exciting two  $30s^3S_1$  Rydberg atoms as a function of internuclear distance. Of primary importance here is that the interatomic potential is clearly not well behaved for internuclear spacings less than 750 nm. Calculation performed and figure prepared by Dr. Yoshida.

Both of these problems imply that the problem of the mean-field treatment comes from our treatment of the short range physics of closely spaced atoms, but which effect is more important? For Rydberg atoms under our conditions, the blockade radius is greater than  $1 \mu\text{m}$ , which is larger than the typical length scale on which we need to consider the effects of other Rydberg levels on the interatomic potential. Figure 4.3 shows a calculation from Dr. Yoshida of the relative excitation strength of exciting atom pairs of  $30s^3S_1$  Rydberg atoms as a function of internuclear distance. The actual excitation strength is not of concern here, but it is clear that the interatomic potential remains relatively well behaved for spacings larger than 750 nm, and below

that threshold becomes more complicated. Therefore, it is most important to concern ourselves with the effect of correlations coming from the Rydberg blockade.

There are two methods we can use to build blockade physics into our treatment, and we will describe them both. The first is to alter the potential by introducing a soft core as  $V = \frac{C_6}{\hbar} \frac{1}{R_B^6 + |r|^6}$ , which reflects the fact that a second atom cannot be excited within a blockade radius of an atom in a Rydberg state [77, 13, 78]. For the case at hand, the blockade radius is defined as  $R_B = (C_6/2\hbar\Omega_{12})^{1/6}$ . Following our previous treatment,

$$\begin{aligned} V_{eff} &= \int_0^\infty d\mathbf{r} \frac{C_6}{\hbar} \frac{1}{R_B^6 + r^6} \langle n_2(\mathbf{r}) \rangle \\ &= \frac{C_6 \rho_{22} \rho}{\hbar} 4\pi \int_0^\infty dr \frac{r^2}{R_B^6 + r^6} \\ &= \frac{2\pi^2 C_6}{3R_B^3} \rho_{22} \rho. \end{aligned} \tag{4.8}$$

Alternatively, we can use our usual form of the interactions and add a short range cutoff to the integral.

$$\begin{aligned} V_{eff} &= \int_{R_B}^\infty d\mathbf{r} \frac{C_6}{\hbar r^6} \langle n_2(\mathbf{r}) \rangle \\ &= \frac{C_6 \rho_{22} \rho}{\hbar} 4\pi \int_{R_B}^\infty dr r^{-4} \\ &= \frac{4\pi C_6}{3R_B^3} \rho_{22} \rho. \end{aligned} \tag{4.9}$$

Both techniques are successful in rendering the integral finite and predict a linear density scaling in contrast to the quadratic dependence expected from dimensional analysis. The results of these two techniques only differ in the numerical pre-factor,

and this difference is of order unity. This slight difference is not of concern for this work as our initial goal is to simply understand the density scaling of the effects we see. Therefore, for the sake of concreteness, we will use the results of equation 4.9 from here on. This yields  $V_{Ryd} = \frac{4\pi C_6}{3R_B^3} \rho$  in equation 4.2.

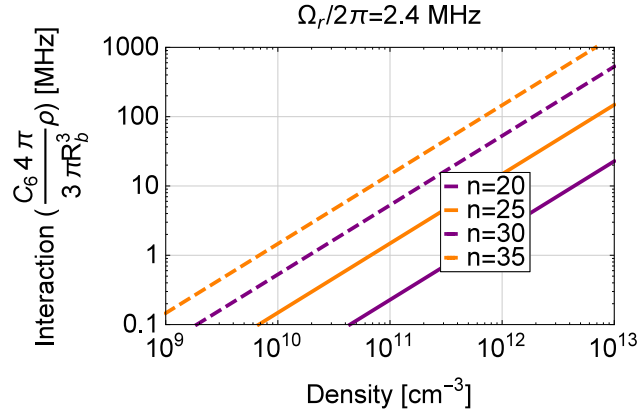


Figure 4.4 : Interaction energy as a function of density for a few principal quantum numbers

#### 4.2.4 Density Scaling

Before even turning on our experiment, we can look at the density scaling of interactions via simulation to know that we are on the right track with our simple approach. It is important to realize that even in the case of a homogeneous gas, there exists a distribution of interparticle spacings and therefore a distribution of interactions felt by given particles. Our goal is to explore how this varies with density in the experimentally relevant regime, where  $\rho > \rho_B$  with  $\rho_B = \frac{1}{4\pi R_B^3}$ .

Using Matlab, we randomly distribute  $10^4$  particles within a cubic box and define length to yield a density of 1. For every particle i, we then calculate the interaction

felt as a result of all of the other particles in the box greater than one blockade radius away. Explicitly, we calculate

$$V_i = \sum_{j \neq i} \frac{C_6}{\hbar} \frac{1}{|r_{ij}|^6} \Theta(|r_{ij}| - R_B) \quad (4.10)$$

where  $\Theta$  is the Heaviside theta function, used to cut off the sum for particles spaced closer than one blockade radius apart. This is done for a number of blockade radii with values chosen to vary  $\rho/\rho_B$  from 1 to 50.

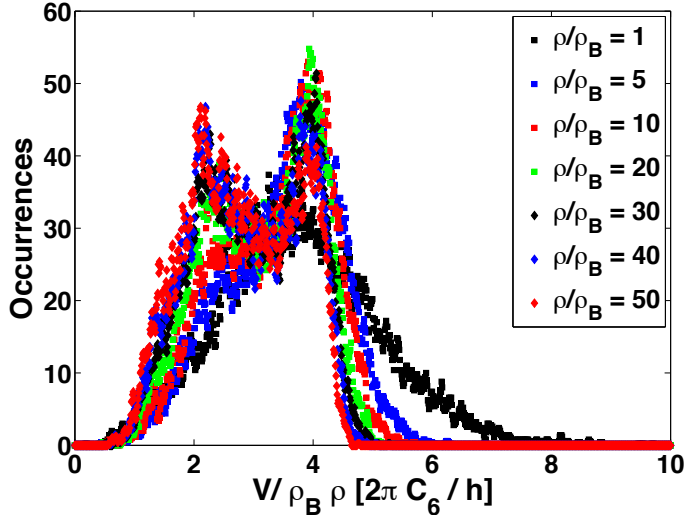


Figure 4.5 : Histogram of shifts for a homogeneous gas of  $10^4$  particles at varying  $\rho/\rho_B$ . In appropriately scaled units, the data collapses onto a common curve for large  $\rho/\rho_B$ .

To explore the scaling, we create a histogram of  $V_i$  with the x axis scaled by the expected factor and look for the data to collapse onto a single curve. This is plotted in figure 4.5 and we see that the scaling needed to get the data to collapse is  $\frac{C_6 \rho_B}{\hbar} \rho^2$ . Note that the scaling is not perfect as the width of the distribution in scaled units is

decreasing as we increase  $\rho/\rho_B$ , however the peak of the distribution remains fixed. This result confirms that in the regime of  $\rho > \rho_B$  we expect to see the linear density scaling that was derived in the previous section.

#### 4.2.5 Local Density Approximation

For all derivations so far, we have assumed a gas of homogeneous density. However, this is not the case in a real experiment. Our Sr atoms are trapped in a harmonic trap with a distribution of densities inside where dynamics may proceed differently in different parts of the trap. One way to handle this density inhomogeneity is to employ the local density approximation (LDA).

Within the LDA, atoms behave as if they are in a gas of a homogeneous density which is given by the local density at the position of the atom. Each local density is then appropriately weighted and then a sum or integral is performed over all contributing densities to calculate the result we will see in our experiment.

Formally, we are interested in calculating some observable,  $I$ , from our inhomogeneous gas of atoms. First, we solve for the observable as a function of density assuming the density is constant to obtain  $I(\rho)$ . To calculate what we will see in the experiment, we perform the following integral

$$I = \int_0^{\rho_0} I(\rho)g(\rho) d\rho \quad (4.11)$$

where  $g(\rho)$  is the weighting function and  $\rho_0$  is the peak density.

We now need to calculate  $g(\rho)$ , which satisfies the relation  $N = \int_0^{\rho_0} g(\rho)d\rho$  where  $N$  is the total number of particles. This is easily done for a thermal gas of atoms in

a harmonic trap. For the sake of clarity in this derivation, I will assume spherical symmetry.

$$\begin{aligned} N &= \int \rho(\mathbf{r}) d^3\mathbf{r} \\ &= 4\pi \int r^2 \rho(r) dr \end{aligned} \quad (4.12)$$

For thermal atoms in a harmonic trap,  $\rho(r) = \rho_0 e^{-\chi r^2}$  where  $\chi = \frac{m\omega^2}{2k_B T}$ ,  $\omega$  is the harmonic trap oscillation frequency,  $m$  is the mass of a strontium atom,  $k_B$  is the Boltzmann constant and  $T$  is the temperature. Taking the log of both sides of the equation for density, we obtain

$$r^2 = \frac{1}{\chi} \ln\left(\frac{\rho_0}{\rho}\right) \quad (4.13)$$

$$r = \frac{1}{\sqrt{\chi}} \left[ \ln\left(\frac{\rho_0}{\rho}\right) \right]^{1/2} \quad (4.14)$$

$$dr = -\frac{1}{\sqrt{\chi}} \frac{1}{2\rho} \left[ \ln\left(\frac{\rho_0}{\rho}\right) \right]^{-1/2} d\rho \quad (4.15)$$

Using these relations, we can change the variable of integration from  $r$  to  $\rho$  and obtain

$$N = 2\pi \left[ \frac{2k_B T}{m\omega^2} \right]^{3/2} \int_0^{\rho_0} [\ln(\frac{\rho_0}{\rho})]^{1/2} d\rho \quad (4.16)$$

By comparing equation 4.16 to our definition of  $g(\rho)$ , we can recognize that

$$g(\rho) = 2\pi \left[ \frac{2k_B T}{m\omega^2} \right]^{3/2} [\ln(\frac{\rho_0}{\rho})]^{1/2} \quad (4.17)$$

In the case of an anisotropic potential, the following can also be derived

$$g(\rho) = \frac{2\pi}{\omega_1 \omega_2 \omega_3} \left[ \frac{2k_B T}{m} \right]^{3/2} [\ln(\frac{\rho_0}{\rho})]^{1/2} \quad (4.18)$$

where  $\omega_{1,2,3}$  are the respective harmonic trap oscillation frequencies.

A natural question to ask at this point is whether the LDA is an appropriate approximation for our system. It is obvious that in the case of infinitely long range interactions, this approximation will break down. It is essential that the dynamics for one particle only depend on nearby neighbors and not every other particle in the trap. In typical atomic systems with contact interactions this is usually satisfied. However it is not exactly clear that this is correct in our case. While the Rydberg-Rydberg interactions are long-ranged, the  $1/r^6$  potential falls off rapidly such that the interaction is dominated by nearest neighbors.

Formally, for the LDA to be valid, the length scale for density variation in the trap (given by the density distribution) should be long compared to the other relevant length scales (i.e. the blockade radius, the interatomic spacing and the distance the Rydberg atom travels in its lifetime). The largest of these scales in our experiment is the blockade radius ( $\sim 1\mu m$ ), and the spatial extent of our cloud is only slightly larger in the tight axis of the trap ( $\sim 6\mu m$  1/e radius). As we will see in the next section, while our system is not deep within the regime where we expect the LDA to hold, we are still able to get good agreement between theory and experiment.

#### 4.2.6 A Quick Word on $\Gamma$

In this discussion of treating shifts and dephasing, we have focussed entirely on the shifts and ignored dephasing. The reason for this is simple, we understand the microscopic origin of  $V$  but we don't know the microscopic origin of  $\Gamma$ . The following section will convince you of the necessity of including this term even though we don't understand its origin, and from the spectra you will see it is clear that the magnitude of the dephasing is at least on the order of the magnitude of  $V$ . For that reason, we

choose to treat  $\Gamma$  in the same manner as  $V$ , that is with a linear scaling with density and within the LDA, yielding  $\Gamma_{Ryd} = \beta \frac{4\pi C_6}{3R_B^3} \rho$  in equation 4.2.

#### 4.2.7 Previous Work

There is great variation in the results and theoretical treatments for experiments involving interacting Rydberg atoms, and it is important to consider our approach in this context. This risks introducing some confusion because of the often contradictory conclusions, but it also highlights the need for more study.

Our treatment of level shifts and dephasing draws upon previous work. The Adams group introduced a level shift proportional to Rydberg population ( $V = V_{Ryd}\rho_{22}$ ) as a mean field treatment of interactions in a master equation describing the observation of optical bistability in a Rydberg system [84]. The scaling of  $V_{Ryd}$  with density was not specified. The same group also introduced a dephasing rate proportional to Rydberg population ( $\Gamma = \Gamma_{Ryd}\rho_{22}$ ) as a mean field treatment of dephasing that was suggestive of superradiance in an interacting Rydberg system [83]. Again, the scaling of  $\Gamma_{Ryd}$  was left unspecified. More recently, the Pfau group used a dephasing rate proportional to Rydberg population as a mean field treatment of dephasing of Rabi oscillations for Rydberg excitation in a thermal vapor. They found a linear scaling with density and the numerical value is identical to our treatment within factors of order unity. They do not discuss the microscopic origin of the dephasing, but they note that the scaling breaks down at higher density. None of the groups perform any density averaging when comparing experiment and theory.

One should note recent work at densities (below a few times  $10^{10} \text{ cm}^{-3}$ ) studying coherent effects in interacting, ultracold Rydberg gases excited in a ladder configu-

ration. Different arrangements lead to coherent population trapping (CPT) [86, 87], electromagnetically induced transparency (EIT) [83, 88, 89, 87], and Autler-Townes (AT) spectra [90, 91, 92]. They all use alkali atoms. The AT configurations use a strong laser driving the principal S-P transition and probe with a weaker laser tuned near resonance with the transition to the Rydberg level, which differs from our excitation scheme and leads to relatively broad lines. Fixed dephasing rates (not dependent upon  $\rho_{22}$ ) are used in a master-equation description of experiments in refs. [88, 91, 92], and no resonance shifts are observed. Level shifts and no appreciable broadenings are observed in AT spectra in ref. [90], and they are described with a two-particle density matrix explicitly putting in a value for the shift of the doubly-excited Rydberg state with no additional dephasing. This is similar to the treatment of EIT in [89], however in this configuration a loss of EIT transmission is seen with no shift or broadening. Ref. [86] similarly sees a reduced contrast but no shift or broadening of CPT signals. Ref. [87] provides a unified description of EIT [89] and CPT [86] results based on a Monte-Carlo treatment of interacting three-level atoms [96] and a cluster expansion of the density matrix treatment for  $N$ -atoms that is extended to second (two-atom) order while retaining some terms for three-atom correlations [86]. These are more advanced treatments explicitly putting in a value for the shift of the doubly-excited Rydberg state with no additional dephasing. Agreement is good, but some discrepancy is observed between theory and experiment in high density and strong excitation EIT spectra. The authors argue that a mean-field description is not valid because it leads to shifts and broadenings that are not seen in the data. No averaging over density appears to have been done in any of these papers.

## 4.3 Autler-Townes Spectra: Comparison of Experiment and Theory

### 4.3.1 Experimental Details

With a firm groundwork of theory laid, we now turn on our experiment and see what happens in real life. The basics of exciting Rydberg atoms and the tools used to detect them were laid out in chapter 2, so here we will only cover the details specific to the measurement of Autler-Townes spectra.

We begin with atoms trapped in an optical dipole trap. Using the trim coils on our apparatus, we apply a magnetic field along gravity which shifts the frequency of the  $^1S_0 \rightarrow ^3P_1(m_j = 1)$  transition approximately 3 MHz from its unperturbed frequency. This field serves as a quantization axis and through a choice of polarization allows us to couple to only one  $m_j$  Rydberg state. In order to rapidly remove any charged particles which may be formed from ionizing Rydberg atoms, we also apply an electric field of 0.8 V/cm in the same direction as the magnetic field using our electric field plate.

We use circularly polarized 689 nm light along the axis of the field to drive the  $^1S_0 \rightarrow ^3P_1(m_j = +1)$  with a variable Rabi frequency between  $\Omega_{01} = 2\pi \cdot 26$  and 133 kHz and detuning between  $\Delta_{01} = -2$  and 2 MHz. The excitation time and power of the 689 nm laser is precisely controlled with an acousto-optic modulator.

The 319 nm light propagates perpendicular to the magnetic field with a linear polarization aligned with the field in order to drive the  $^3P_1(m_j = +1) \rightarrow 5s24s\ ^3S_1(m_j = +1)$  transition. For all experiments performed here, the Rabi frequency remains constant at  $\Omega_{12} = 2\pi \cdot 2.4$  MHz with detuning  $\Delta_{12} = 0$ . The timing and power of this

laser is also precisely controlled with an acousto-optic modulator.

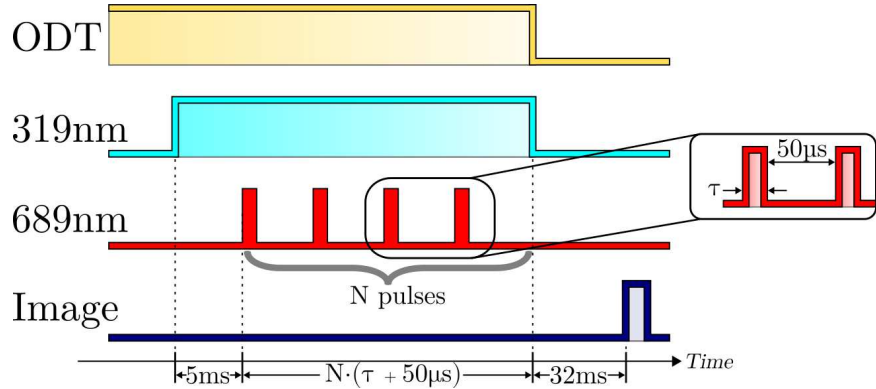


Figure 4.6 : Timing diagram for taking Autler-Townes spectra. Details in text.

For taking spectra data, we employ a pulsed excitation scheme. We first turn on the 319 nm laser for 5 ms before rapidly pulsing the 689 nm laser a number of  $N$  times to yield approximately 50% peak loss. After the pulse sequence, the atoms are released from the trap and imaged after a 32 ms time of flight. This timing is illustrated in figure 4.6.

The pulse sequence is chosen to have a short on time followed by 50  $\mu$ s of off time which is essential to investigate the time dynamics of the spectra. Since our method of detection is counting ground state atoms, shot to shot fluctuations and other technical sources of noise make it hard for us to detect small numbers of Rydberg atoms. By employing a pulsed scheme with an off time that is long compared the lifetime of both the  $^3P_1$  and  $5s24s\ ^3S_1$  state, we can assume each pulse is independent. By then using  $N$  pulses we can amplify the loss per pulse out of the noise to get a better signal to noise ratio. To then compare the data to theory, we use the known number of pulses to calculate the loss per pulse and subtract that from the initial number of atoms

before normalizing the spectra to 1. This allows us to only calculate the dynamics for a single pulse and compare to the experiment.

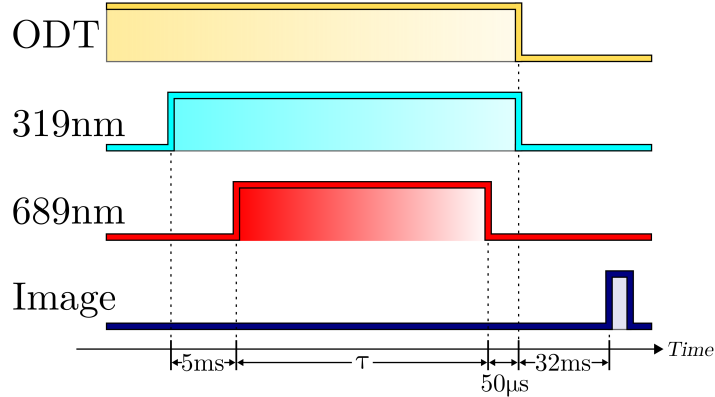


Figure 4.7 : Timing diagram for taking time evolution. Details in text.

For taking time evolution data, we again first turn on the 319 nm light for 5 ms, and then apply a single pulse of 689 nm light. This pulse is then followed by 50  $\mu$ s of just 319 nm light before both the 319 nm and ODT are extinguished and the atoms are allowed to fall for a 32 ms time of flight being imaged. This is shown in figure 4.7. The data are then normalized to 1 for comparison to theory.

#### 4.3.2 Calculation Details

In this section, I will provide a bit more detail about the way we have implemented the previously discussed theory. The solutions to the optical Bloch equations are not analytic and we have developed code in Matlab to solve the equations and implement the LDA. As with any computer code, we have made a few choices in our implementation in the interest of calculation speed which I will detail here.

Our ultimate observable from the experiment is the number of ground state atoms after a time of flight which is long compared to timescale of the dynamics. To save time on computation, we only solve the optical Bloch equations until the 319 nm light is extinguished. At that point there is, in general, population in all three states. However, we know that prior to imaging, all population from the  $^3P_1$  state and 1/3 of the population of the  $5s24s\ ^3S_1$  state will eventually decay to the ground state and be imaged. Therefore we just add this population to  $\rho_{00}$ .

Looking back at equation 4.11 we have assumed that density is a continuous variable, but we do not treat it that way for our numerical simulations. Instead we solve the optical Bloch equations for 10 different densities,  $\rho_i$ , that are chosen such that

$$\int_{\rho_i}^{\rho_{i+1}} g(\rho) d\rho = N/10 \quad (4.19)$$

where  $N$  is the total number of particles. We use these densities to perform a 10 point trapezoidal-rule approximation of the integral in equation 4.11. This strategy allows us to get a good approximation of the integral while limiting the number of times we need to solve the optical Bloch equations.

### 4.3.3 Short Time Dynamics

First, we will test our theory against the spectra we have obtained for very short pulses, 2  $\mu s$ . Using the method described above, we have taken these short time spectra at two different peak densities,  $1.9 \times 10^{12} \text{ cm}^{-3}$  and  $1 \times 10^{13} \text{ cm}^{-3}$ . At  $n = 24$  with  $\Omega_{12} = 2.4 \text{ MHz}$ , the blockade density  $\rho_B = 4.2 \times 10^{11} \text{ cm}^{-3}$ . Therefore these densities correspond to  $\frac{\rho}{\rho_B} \sim 5$  and 25 respectively, and will from here on be referred to as low and high density. We note that both low and high density data are taken

in the same depth ODT and the variation in density was achieved by changing the length of the initial collection phase in the magnetic trap. This results in a change in number and a slight change in temperature which gives rise to the two densities mentioned above.

Recalling equation 4.2, it is clear that there are other parameters in the system which need to be accounted for. Fortunately, they are either known or easily measured. From analysis of our laser locks and the narrowest spectra we have obtained, we know that the linewidth of the 689 nm (319 nm) laser is 30 kHz (300 kHz) respectively. The decay rate of the  $^3P_1$  state is known very accurately as  $2\pi \cdot 7.5 \times 10^3 s^{-1}$ . However, there is a bit of uncertainty in the decay rate of the excited state as it has not been directly measured. We obtain the best agreement for low intensity Autler-Townes spectra using a decay rate of  $2\pi \cdot 50 \times 10^3 s^{-1}$ , which is slightly higher than expected from scaling the results of [42]. However, the error could also come from the fact that our calculation of decay branching ratios might be off as we did not consider all decay channels.

Since all other parameters in the system are well known, we are able to explore just the effects of level shifts and dephasing. To allow variation of these two effects, we have added a scale factor in front of the results of equation 4.5 to define  $V_{ryd} = \alpha \frac{4\pi C_6}{3R_B^3} \rho$  and  $\Gamma_{2Ryd} = \beta \frac{4\pi C_6}{3R_B^3} \rho$ .

First, let's focus on the low density data. It is clear that for higher excitation strength ( $\Omega_{01}$ ), the data contains a sizable shift and asymmetry, and this deviates from the non-interacting case,  $\alpha = \beta = 0$ .  $\alpha = 1$  gives a good agreement with the shift and asymmetry, however it slightly underestimates the width of the peaks. The case of  $\alpha = 1$  and  $\beta = 1$  slightly improves the fit by slightly broadening the peaks.

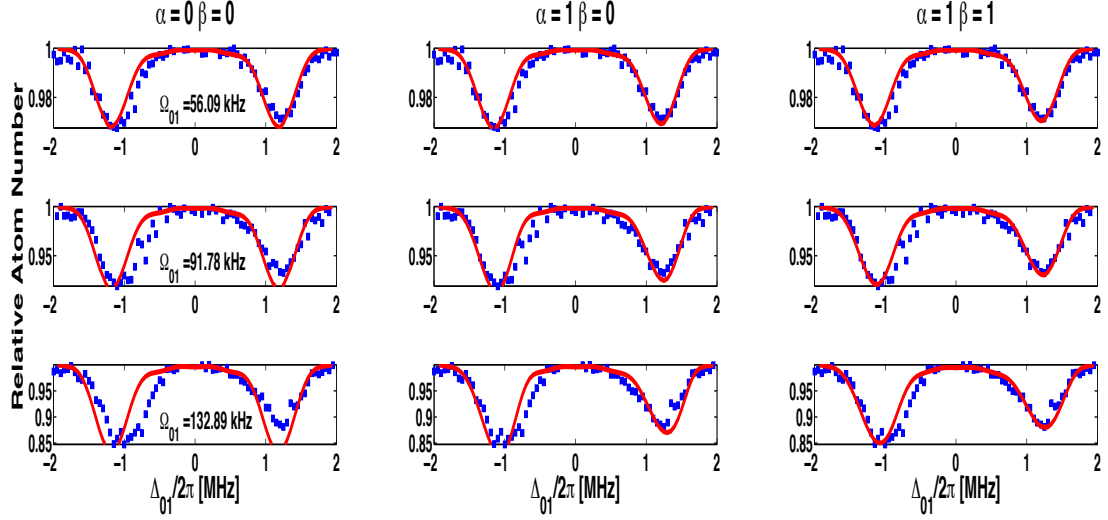


Figure 4.8 : Blue squares: Experimental data of ground state population after a single pulse of excitation with initial peak density,  $\rho_0 = 1.9 \times 10^{12} \text{ cm}^{-3}$ . Details in text. Red lines: Theoretical calculation using LDA for varying strengths  $V_{Ryd}$  and  $\Gamma_{2Ryd}$ .  $\alpha$  and  $\beta$  are defined in text.

The spectra are not too sensitive to the amount of dephasing at low density, but we can conclude that some amount is needed to improve agreement between theory and experiment. The blue detuned peak is well fit with  $\beta = 1$ , but the red detuned peak calls for a larger value.

For high density data, the spectra are very sensitive to both level shifts and dephasing. Again we see that  $\alpha = 1$  does a good job reproducing the shift seen in the data. However, it does not account for the widths or the loss that we see near  $\Delta_{01} = 0$ . Only by increasing  $\beta$  to 2 can we match the amount of loss seen here at zero detuning.

Taking the results at the two densities together, our results imply strongly that

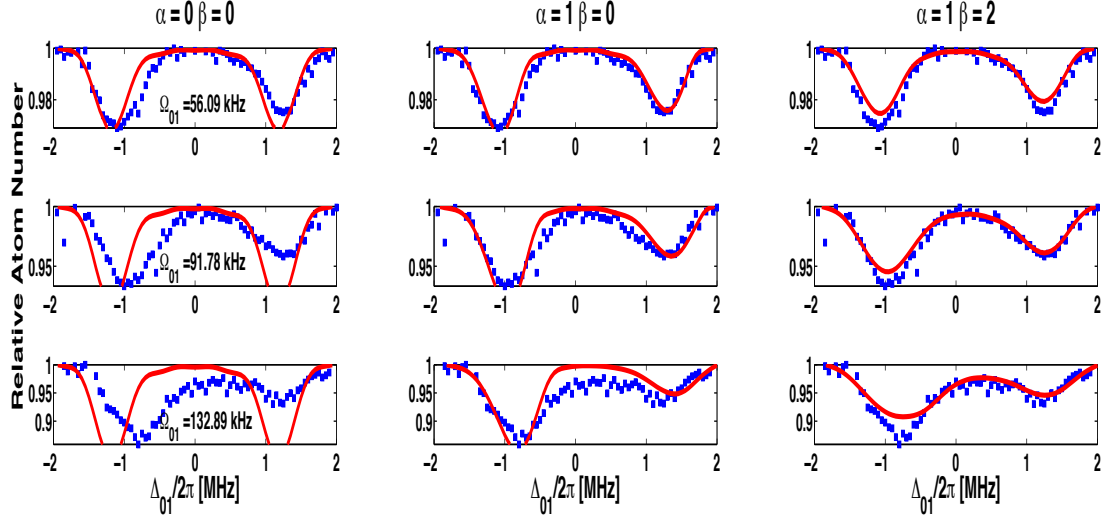


Figure 4.9 : Blue squares: Experimental data of ground state population after a single pulse of excitation with initial peak density,  $\rho_0 = 1 \times 10^{13} \text{ cm}^{-3}$ . Details in text. Red lines: Theoretical calculation using LDA for varying strengths  $V_{Ryd}$  and  $\Gamma_{2Ryd}$ .  $\alpha$  and  $\beta$  are defined in text.

our treatment of level shifts is correct because we get good agreement at two different densities with the same value of  $\alpha = 1$ . We note that quadratic variation of the level shift term is ruled out by our data.

$\Gamma$  is a different story. It is clear the term can be used to describe the spectra, but due to the lack of sensitivity at low density and the clear best fit value of  $\beta = 2$  at high density, it is difficult to determine if our density scaling is correct. However it is clear that dephasing is playing an important role here.

#### 4.3.4 Long Time Dynamics

As a more stringent test of our theory, we will see how the spectra evolves in time.

For this data, we have used only high density samples and chose a low and high Rabi frequency to see how the spectrum changes as we increase the pulse length from 2  $\mu\text{s}$ .

The results are plotted in figures 4.10 and 4.11.

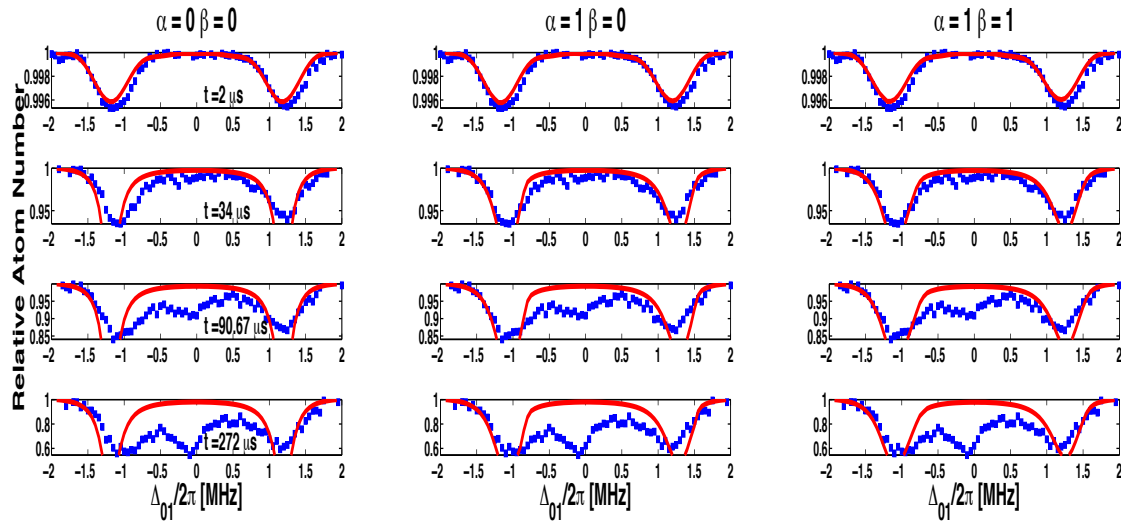


Figure 4.10 : Blue circles: Experimental data of ground state population after a single variable length pulse with initial peak density,  $\rho_0 = 1 \times 10^{13} \text{ cm}^{-3}$  and  $\Omega_{01} = 20.14 \text{ kHz}$ . Details in text. Red lines: Theoretical calculation using LDA for varying strengths  $V_{Ryd}$  and  $\Gamma_{2Ryd}$ .  $\alpha$  and  $\beta$  are defined in text.

Both data sets show the same trend: while we obtain good agreement at early times, there is a dramatic difference between theory and experiment at later times. While the amount of asymmetry in the Autler-Townes peaks seems well described even at late times, our theory vastly underestimates the loss near  $\Delta_{01} = 0$ .

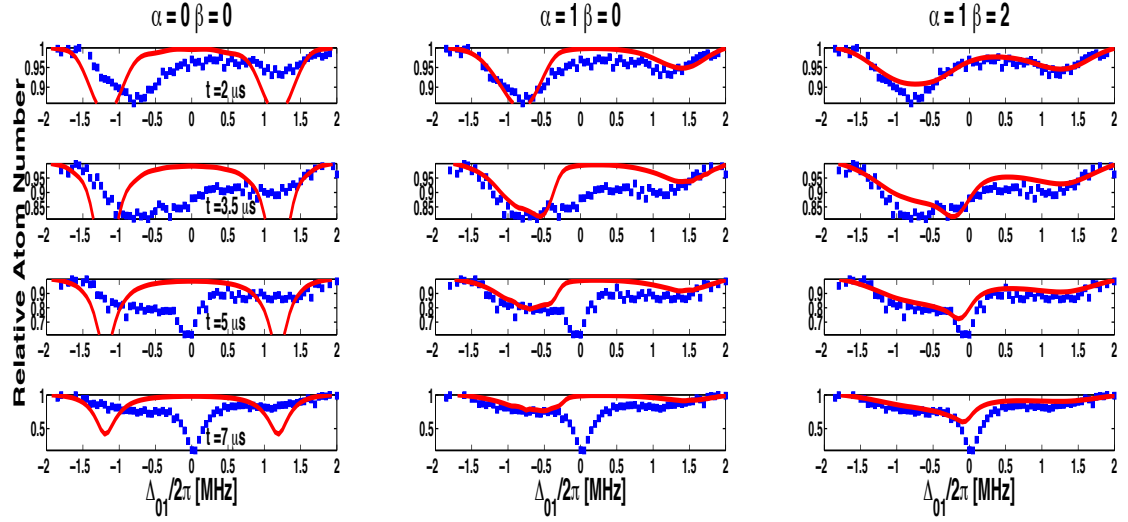


Figure 4.11 : Blue squares: Experimental data of ground state population after a single variable length pulse with initial peak density,  $\rho_0 = 1 \times 10^{13} \text{ cm}^{-3}$  and  $\Omega_{01} = 132.89 \text{ kHz}$ . Details in text. Red lines: Theoretical calculation using LDA for varying strengths  $V_{Ryd}$  and  $\Gamma_{2Ryd}$ .  $\alpha$  and  $\beta$  are defined in text.

Our time evolution data, figures 4.12 and 4.13, tells the same story and shows more explicitly where our calculations fall short of describing the data. We take data of the time evolution at varying  $\Omega_{01}$  at a few  $\Delta_{01}$ , corresponding to 0 and at the position of peak loss for the red and blue detuned Autler-Townes peaks observed in the short time data.

#### 4.4 Conclusions

As we mentioned in the beginning, the different effects of interactions and dephasing on the Autler-Townes spectra allow us to isolate one from the other when looking where our calculation deviates from theory. At early times, our theory is able to

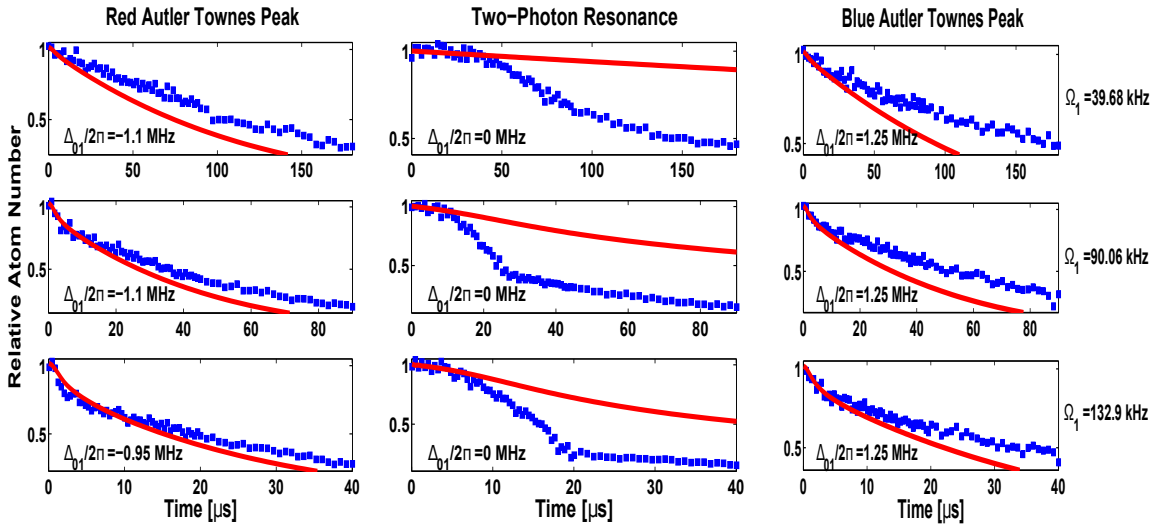


Figure 4.12 : Blue squares: Experimental data of time dependent ground state population after a single variable length pulse with initial peak density,  $\rho_0 = 1.9 \times 10^{12} \text{ cm}^{-3}$ . Red lines: Theoretical calculation using LDA for  $\alpha = 1$  and  $\beta = 2$ .

reproduce the dynamics over a wide variety of conditions. However, for long time dynamics, it fails by strongly underestimating the effects of dephasing, which gives rise to a strong loss feature at  $\Delta_{01} = 0$ .

This is not terribly surprising. As previously discussed, we were on firm theoretical ground for the derivation of the treatment of level shifts, and this part of the calculation does a good job describing the data. On the other hand, we have no microscopic description of what is causing the dephasing here, so it does not necessarily need to have the same form as  $V$ .

To belabor the point further, previous work uses a dephasing term in the optical Bloch equations to treat density inhomogeneity. Inhomogeneity leads to a distribution of  $V$  within the system which effectively broadens the transition and gives rise to an

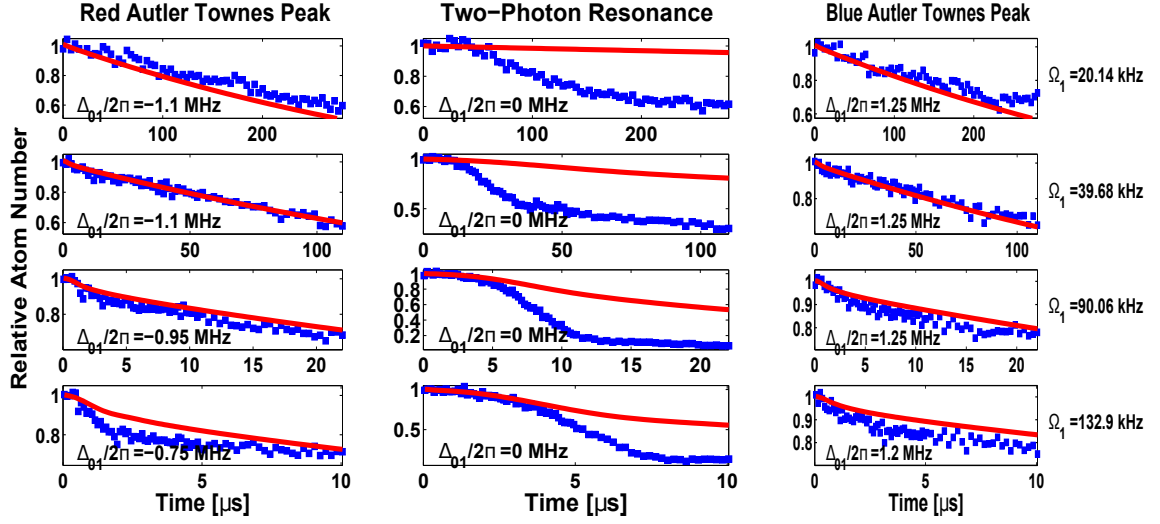


Figure 4.13 : Blue squares: Experimental data of time dependent ground state population after a single variable length pulse with initial peak density,  $\rho_0 = 1 \times 10^{13}$  cm $^{-3}$ . Red lines: Theoretical calculation using LDA for  $\alpha = 1$  and  $\beta = 2$ .

apparent dephasing. However, within the LDA the density inhomogeneity is handled separately. Therefore, the dephasing that we see is not some artifact of having a trapped gas, but a real effect. We do note that we have not accounted for the statistical spread of shift strengths that exists even in the case of a homogenous gas. As can be seen in figure 4.5, this is on the order of the value of the shift.

There are a few clues lurking in our data which shed some light on the possible source of real dephasing, but at this time we have no clear picture. The first clue lies in the time evolution of the system. As we fit the early time dynamics so well, and later time dynamics so poorly, it appears that the rate of dephasing is actually increasing in time. Even more curiously, using just our calculations with a dephasing as a constant, qualitatively matching the loss seen on resonance requires a dephasing

rate of  $\sim 75$  MHz. Even considering the distribution of shifts plotted in 4.5, this is too large of a dephasing rate to make any sense and would require extremely high Rydberg fractions on the order of a few percent.

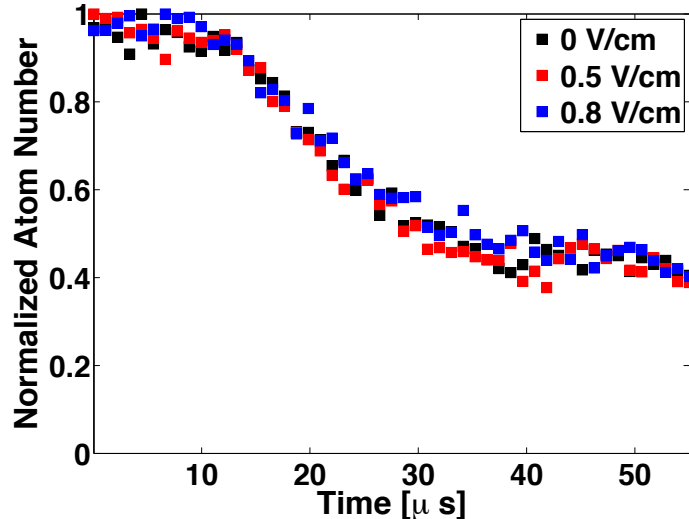


Figure 4.14 : Time evolution at  $\Delta_{01} = 0$  with  $\Omega_{01}/2\pi = 39.68$  kHz at various applied electric fields. There is no measurable difference in the time evolution yielding the conclusion that the presence of electric charges is not a likely source of dephasing.

More likely is that interactions stronger than van der Waals are at play. One possible culprit is the presence of electric charges. If a Rydberg atom is ionized, the resulting ion and electron might cause either ionizing or l-changing collisions with other Rydberg atoms leading to dephasing. Ionization can occur from photoionization from either the 689 nm, 319 nm or ODT laser, so we cannot get rid of all possible sources of seed ionization. However, we can change the timescale that an ion (or electron) would leave the system if it were created by varying the electric field on the sample.

To test this hypothesis, we repeated our measurement of the time evolution at a fixed detuning of  $\Delta_{01} = 0$  in the presence of a varying electric field. For this test, we chose  $\Omega_{01}/2\pi = 39.68$  kHz such that the at the largest field applied, an ion escapes the trap on timescales much faster than the dynamics. At 0.8 V/cm, this corresponds to 0.1  $\mu$ s, which is much faster than the loss timescale of tens of  $\mu$ s. However, as can be seen from the data plotted in figure 4.14, the applied electric field yields no measurable effect whatsoever on the data. This suggests that charged particles are not the cause of the dephasing we observe.

One final hypothesis is the effect of population in other Rydberg states. As mentioned, we have neglected the small but finite decay (both natural and blackbody driven) of the Rydberg state to other lower lying Rydberg states. Interaction between s and p Rydberg atoms feature long range dipole-dipole interactions connecting  $|s, p\rangle$  to  $|p, s\rangle$  and can be quite strong. This mechanism seems to be a promising candidate, however, we are currently unable to test whether it is the case. Another effect along these lines is the possibility of superradience, which will rapidly depopulate the Rydberg state [97]. With the additional tool of state selective field ionization on the new apparatus in the Killian lab, we will be able to test this hypothesis in the near future by measuring where the Rydberg population goes.

Even without the improved diagnostics of the new apparatus, there are features of the data which support this hypothesis. From our time evolution data, we see that on resonance, dephasing turns on to create a huge loss, but then turns off when the density drops too low. Stronger driving ( $\Omega_{01}$ ) leads to lower density before the loss turns off. This is strongly suggestive of a nonlinear process such as population of p states or superradience. It is possible that a system such as this could have a high

loss and low loss configuration. As a function of density and driving, such a system might have a region of instability which can display hysteresis. This type of behavior has been seen previously in Rydberg gases [97]. Currently, dephasing is the main hinderance to our ability to observe Rydberg dressing. If superradience or p state population is to blame for this, it may be possible to mitigate this effect by using microwave transitions to rapidly deplete the population of the p states, thus turning off the fast loss and allowing the observation of Rydberg dressing of a BEC.

To conclude, the role of level shifts and dephasing comes up in many contexts in Rydberg atom physics. In this section we have developed techniques to understand them in the context of Autler-Townes spectra. By using the LDA, we are able to disentangle the apparent dephasing which comes from inhomogeneous densities from a real dephasing in the system. Further investigations into this rich system are needed, but this work hopefully provides a useful starting point.

## Chapter 5

### Probing Rydberg Dressing

#### 5.1 Introduction

Back in chapter 1, we described the concept of Rydberg dressing as a method to add controllable long-range interactions to a quantum many-body system such as a BEC. By studying the formation of Rydberg molecules and dephasing, we then focused on learning about possible loss processes in this system that have hindered the realization of this goal. So far in our efforts, we have found loss time scales that are much faster than originally anticipated, however this does not completely rule out the possibility of ever realizing Rydberg dressing of a BEC. Therefore, in this section my aim is to lay out a plausible method of detecting and characterizing Rydberg dressing in a BEC, even in the presence of a fast time scale loss.

#### 5.2 Measuring Interaction Strengths

In ultracold quantum gas systems, short-range atom-atom interactions are characterized by a single parameter, the s-wave scattering length,  $a$ . For a given atomic species,  $a$  is a fundamental parameter that can be positive or negative (yielding repulsive and attractive interactions respectively) and is typically on the order of  $100 a_0$ , where  $a_0$  is the Bohr radius. Knowledge of the s-wave scattering length is essential for first determining a route to create a quantum degenerate gas and then for understanding

the way it will behave. As such, a number of techniques have been developed to measure this quantity accurately. By adapting these methods, one can also use them to detect Rydberg dressing.

The first technique is to measure the rate of thermalization in gas of atoms after inducing a quench. Typically, one induces heating or cooling in one dimension and measures the rate of cross dimensional thermalization [98]. With knowledge of the density profile in the ODT, this rate can be related to the scattering cross section from which we can extract the scattering length. For studying Rydberg dressing, this would be very difficult to use. Thermalization timescales are long, typically on the order of 100 ms or longer, and the lifetime our sample in the presence of Rydberg dressing is orders of magnitude to short ( $\sim 10\mu s$ ). Even if this challenge of timescales were overcome, a change in the rate of thermalization would only provide indirect evidence of Rydberg dressing, and would lack direct proof that the induced interactions are long-ranged.

A second technique is to modify the expansion of a BEC as it is released from the ODT. This is the technique we employed when measuring the optical Feshbach resonance in Sr [99], and is quite sensitive in the case of  $^{88}\text{Sr}$ , where the background scattering length is near 0. Still, this requires 1 to 10 ms of interaction time which is still too long for the loss timescales in the system. Careful analysis of the shape of the expanding BEC might yield evidence that the induced interactions are long-ranged; however, concerns over optical potentials formed by the dressing lasers might pose a challenge for this type of analysis. A similar technique was proposed in [77] and was attempted in [25] using Rb. Due to the strong optical potential formed by one of the lasers used in this experiment, this modified scheme required the BEC to come to

equilibrium before being released. This greatly increased the time the laser needed to be on for, which only allowed weak coupling to the Rydberg state. As such, no effect was observed.

A final technique is to use Bragg spectroscopy to probe the dispersion relation of a BEC [100]. Simply put, a moving optical lattice is used to impart a well defined momentum to the BEC. Measuring the probability of an atom receiving the momentum kick as a function of energy (controlled by the frequency difference between the beams making the optical lattice) allows a precise measurement of the dispersion relation,  $E(k)$ . As this is a spectroscopic technique, one can measure changes in the dispersion with RF accuracy making this technique extremely sensitive. Also, as I will show in the remainder of this chapter, this technique also provides a clear smoking gun of long range interactions in the BEC.

### 5.3 Bragg Spectroscopy

For a more quantitative picture of Bragg spectroscopy, it is useful to think of this process as a two-photon Raman process. As a starting point, consider a free but isolated two-level atom at rest that is subject to two counter-propagating laser beams. These two beams are far detuned from the excited state but only have a small frequency difference between them,  $\delta\omega$ . This situation is depicted in figure 5.1.

Considering the atom's motional degree of freedom, we know that a free isolated atom will obey the following dispersion relation

$$E_0 = \frac{\vec{p}^2}{2m} \quad (5.1)$$

where  $\vec{p}$  is the atoms momentum and  $m$  is the mass of the atom. For two counter-

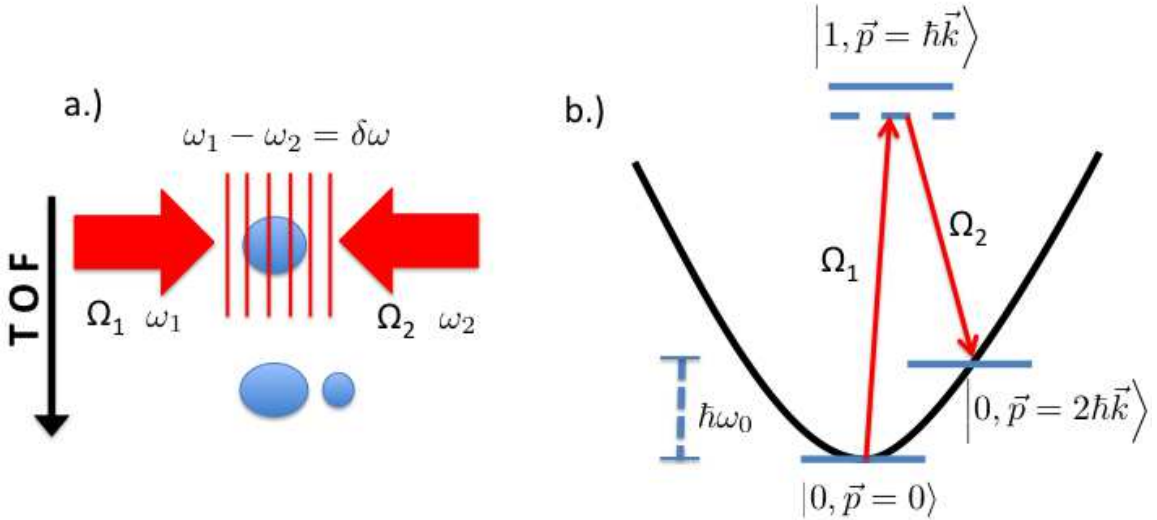


Figure 5.1 : a.) Cartoon representation of Bragg spectroscopy of a BEC. Counterpropagating laser beams with a small frequency difference create a moving optical lattice which can impart  $2\hbar k$  momentum to the atoms which become spatially separated from the main cloud after a time of flight (TOF). b.) Energy level diagram of the three state system formed by the atoms and Bragg spectroscopy beams.

propagating laser fields, the absorption of a photon from one beam with subsequent emission into the other would result in a net change in momentum of the atom of  $2\hbar\vec{k}_0$ . Using the dispersion relation we see that this two-photon Raman process is resonant when

$$\hbar\delta\omega_0 = \frac{2\hbar^2\vec{k}_0^2}{m}. \quad (5.2)$$

To analyze the probability of this process occurring, we can consider the system as a 3-level lambda system as shown in figure 5.1. Since our lasers are far-detuned from the excited state, we can adiabatically eliminate it and reduce the problem to a two-level Rabi problem with states  $|0, \vec{p} = 0\rangle$  and  $|0, \vec{p} = 2\hbar\vec{k}\rangle$  and effective Rabi

frequency  $\Omega = \frac{\Omega_1\Omega_2}{2\Delta}$ . Solving this two-level Rabi problem we arrive at the following result,

$$P = \frac{\Omega^2}{\Omega^2 + (\delta\omega_0 - \delta\omega)^2} \sin^2[\sqrt{\delta\omega_0 - \delta\omega)^2}t/2] \quad (5.3)$$

which peaks at  $\delta\omega = \delta\omega_0$ .

Therefore by scanning the frequency difference between the two lasers,  $\delta\omega$ , we can measure the resonant peak response in the probability of the atom receiving a momentum kick of  $2\hbar k_0$  to measure the dispersion at that momentum. It is also important to note that by changing the angle between the beams the imparted momentum can be continuously tuned from 0 to  $2\hbar k_0$ , limited only by available optical access.

This process works equally well for a BEC, where we can describe the condensate as a zero momentum plane wave. In practice, one applies the Bragg lasers and immediately releases the BEC from the trap. After a long enough time of flight, atoms that were excited by the process are spatially separated from the main part of the cloud and absorption imaging allows us to count atoms in both clouds and determine the fraction which were excited.

With long excitation times with the Bragg lasers and a stable RF source creating the frequency difference between the laser fields, we can very accurately measure the dispersion relation of the BEC [100, 101]. In the next section, we will explore how contact interactions and Rydberg dressing modify the simple non-interacting atom dispersion.

## 5.4 Dispersion Relation for a Rydberg Dressed BEC

A typical BEC can be well described with the theory of a weakly interacting Bose gas. To get the dispersion relation, the standard treatment involves starting from the Gross-Pitaevskii equation and applying the Bogoliubov transformation to study the low energy excitations of the BEC. For our purposes, the derivation is not necessary to understanding the results, so we will omit it. The inquiring reader can find a good treatment of the problem in ref [102], but I'll just state the results of that calculation here

$$(\hbar\omega_0)^2 = \frac{\hbar^2 k^2}{2m} \left[ \frac{\hbar^2 k^2}{2m} + 2g\rho \right] \quad (5.4)$$

where  $g = \frac{4\pi\hbar^2 a}{m}$  and  $\rho$  is the homogeneous density of the condensate.

Less rigorously we can realize an alternate route to get to the same result, and this will be more useful in the case of Rydberg dressing. Inspection of equation 5.4 reveals that the full dispersion of the BEC is just the free particle dispersion perturbed by a term owing to atom-atom interactions. I've mentioned previously that these interactions are described by an s-wave scattering length, but more formally we note that atom-atom scattering is well described with the use of the Fermi pseudo-potential

$$V_{Contact}(\mathbf{r}) = g\delta^3(\mathbf{r}) \quad (5.5)$$

where  $\delta^3(\mathbf{r})$  is the Dirac delta function. From this, we can realize that prefactor to  $\rho$  in the additional term in the dispersion is nothing more than the twice the Fourier transform of the interaction potential. By analogy, we can add in the effects of Rydberg dressing in the same manner,

$$(\hbar\omega)^2 = \frac{\hbar^2 k^2}{2m} \left[ \frac{\hbar^2 k^2}{2m} + 2\tilde{V}_{Contact}\rho_{avg} + 2\tilde{V}_{Ryd}\rho_{avg} \right], \quad (5.6)$$

where the tilde indicates the Fourier transform. Despite being rather cavalier in motivating this equation, our results agree with a more rigorous treatment of Rydberg dressing found in ref [13].

To be more quantitative, Rydberg dressed atoms interact via the real space potential,

$$V_{Ryd}(\mathbf{r}) = \frac{f^2 C_6}{r^6 + R_B^6} \quad (5.7)$$

where  $f$  is the Rydberg fraction. For the sake of readers like me who truly hate doing integrals, I'll take the Fourier transform for you here.

$$\tilde{V}_{Ryd} = \int d^3\mathbf{r} \frac{f^2 C_6}{r^6 + R_B^6} e^{-i\vec{k}\cdot\vec{r}} \quad (5.8)$$

$$= \frac{f^2 C_6}{R_B^3} \int d^3\mathbf{s} \frac{1}{1+s^6} e^{-iR_B\vec{k}\cdot\vec{s}} \quad (5.9)$$

$$(5.10)$$

where we have defined  $\vec{s} = \vec{r}/R_B$ . After integrating over  $\phi$ , we obtain

$$\tilde{V}_{Ryd} = \frac{2\pi f^2 C_6}{R_B^3} \int \int s^2 ds \sin\theta d\theta \frac{1}{1+s^6} e^{-iR_B k s \cos\theta}. \quad (5.11)$$

By symmetry the result will be real, so we take the real part of the above equation and proceed

$$\tilde{V}_{Ryd} = \frac{2\pi f^2 C_6}{R_B^3} \int_0^\infty \frac{s^2}{1+s^6} ds \int_0^\pi \cos[kR_B s \cos\theta] \quad (5.12)$$

$$\frac{f^2 C_6}{R_B^3} 2\pi \int_0^\infty \frac{2s \sin[kR_B s]}{kR_B(1+s^6)} ds \quad (5.13)$$

$$(5.14)$$

The remaining one dimensional integral can be evaluated numerically using Mathematica. To check these results, we use the scaled units of ref [13] and are able to accurately reproduce the dispersion relation.

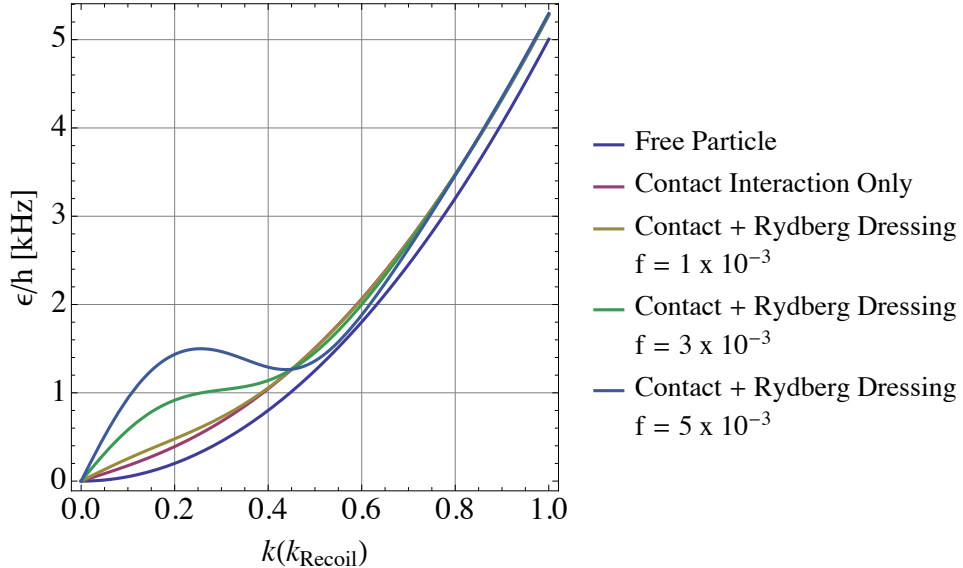


Figure 5.2 : Depiction of how Rydberg dressing interactions modify the dispersion of a BEC with principal quantum number  $n = 25$  and a peak density of  $5 \times 10^{13} \text{ cm}^{-3}$  for various Rydberg fraction,  $f$ . Note how the introduction of contact interactions yields a deviation from the free particle dispersion at all  $k$  and Rydberg dressing only modifies the dispersion at low  $k$ .

From the functional form above, we see that the effects of Rydberg dressing are completely specified by knowledge of the Rydberg level used (i.e.  $C_6$ ), the Rydberg fraction and the blockade radius. Using these results, we plot the dispersion relationship for a BEC of  ${}^{84}\text{Sr}$ , for a peak density of  $5 \times 10^{13} \text{ cm}^{-3}$  and scattering length  $a = 123 a_0$  in figures 5.2 and 5.3 as a function of Rydberg fraction and principal quantum number.

Examining these plots, we see that Rydberg dressing leads to the so called Roton-Maxon dispersion relation which has a few interesting features. At large momenta, the Rydberg dressed interactions yield no difference in the dispersion relationship. This

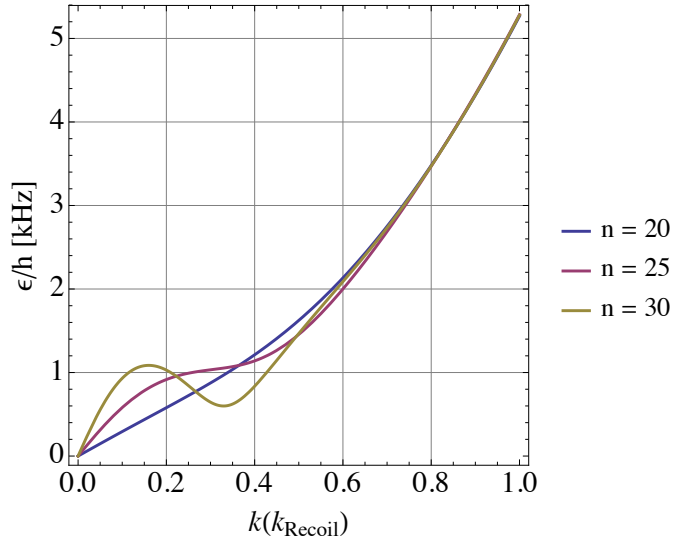


Figure 5.3 : Dependence of dispersion of Rydberg dressed BEC on principal quantum number  $n$ . The calculations use a constant Rydberg fraction,  $f = 3 \times 10^{-3}$  and a peak density of  $5 \times 10^{13} \text{ cm}^{-3}$ .

makes sense because of the short range cutoff. When taking a Fourier transform, short length scales correspond to large momenta and as such the cutoff should kill any effect at large momentum. Also of note, the peak of the effect is controlled largely by the blockade radius. This also makes sense as the blockade radius is the only new length scale we have introduced into the problem. These features are the smoking gun that we have been looking for in showing that the induced interactions from Rydberg dressing are long-ranged. Simply measuring the dispersion at a two points, one low momentum and one high, would be convincing evidence that the interactions feature a short range cutoff as expected. Further, by mapping the entire dispersion and reversing the Fourier transform, one can even map out the real space potential.

Since our goal is to see the effects of Rydberg dressing in a BEC via Bragg spec-

troscopy, we need to use a shallow angle crossing of the Bragg beams to access the low momentum regime. For reference,  $0.2 k_{recoil}$  is equivalent to a separation between the Bragg beam of  $11.5^\circ$ .

#### 5.4.1 Realizing Rydberg Dressing - Some Limitations

From the above plots, we see that Rydberg dressing can significantly modify the dispersion of a BEC. The challenge is to now measure the predicted changes. Whether or not we will be able to observe these effects in experiment boils down to understanding first where our theory is valid, and also what technical limitations exist on the precision of Bragg spectroscopy.

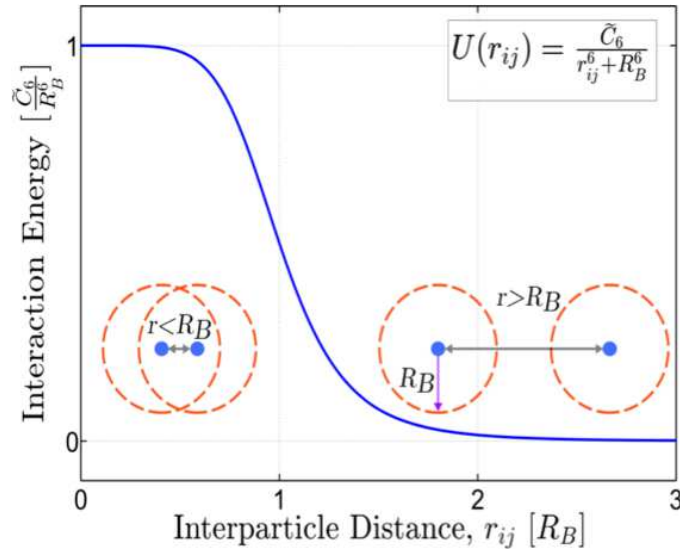


Figure 5.4 : Cartoon of interactions between Rydberg dressed atoms. At large spacings, both atoms are dressed and experience the  $1/r^6$  potential. However, at spacings less than one blockade radius, only one atom at a time can be dressed, leading to just a constant energy shift.

First, in considering where the above theory is valid, we need to consider the effects of blockade on our system. The soft core cutoff of the interatomic potential tells us that atoms spaced less than a blockade radius only see an energy shift which will not affect the dispersion or dynamics of the system. This can be understood in terms of Rydberg blockade. The strong  $1/r^6$  part of the potential comes from the interaction of the Rydberg character admixed into each of the ground state atoms. At spacings less than a blockade radius, only one atom sees the dressing and the Rydberg-Rydberg interaction doesn't exist. This picture is schematically illustrated in figure 5.4. To see the change in dispersion, and eventually the proposed associated dynamic effects, the atoms need to explore the full range of the potential, not just the soft core. This implies that we want  $\rho < \rho_B/f$ . As  $\rho_B$  is most strongly dependent on the principal quantum number, this fact implies we need to work at low principal quantum number to satisfy this condition.

At low principal quantum numbers, we can see appreciable effects for Rydberg fractions on the order of  $10^{-3}$ . A natural question to ask is how large does the effect need to be for us to be able to resolve it via Bragg spectroscopy? Since our signal from the experiment is a shift in a spectroscopic peak, we need to consider how small of a shift we will be able to see. Small shifts are more apparent when one is looking at a narrow spectroscopic feature. To maximize our signal to noise, we need to consider how narrow we can make the Bragg peak.

From equation 5.3, we can always narrow the peak by exposing the lasers for longer. This makes sense as the width is being limited by the energy-time uncertainty principle. However, this is not the only limitation on the width of the Bragg peak. Density inhomogeneity also plays an important role. Our derivation of 5.6 shows that

the position of the peak depends on the density, therefore different parts of the trap will behave differently yielding a broadening of the peak. As derived in ref [100], this limits the rms width of the peak to  $\Delta\omega = \sqrt{8/147}g\rho_0/\hbar$  which is  $\sim 250$  Hz for a BEC of  $^{84}\text{Sr}$  at a density of  $10^{14}$  cm $^{-3}$ . This places a fundamental limit on the narrowest peak we can resolve, however, we will see other limitations can play a more important role.

Another important consideration that is easily overlooked is the stability of the condensate. We have found that in our experiment, there is a sloshing motion of the BEC that is not stable from shot to shot. This gives rise to a small variable initial velocity which also can broaden the Bragg spectrum. Our suspicion is that the sloshing comes from an instability of the beam pointing of the ODT as there is a long path and possible thermal lensing coming from the AOMs that form each to the two arms, but we have so far been unable to confirm that this is the cause. Instead, we have noticed that the sloshing is primarily in the horizontal direction, so by probing the Bragg spectra in the vertical direction the broadening due to sloshing is greatly reduced.

Finally, and arguably most importantly, it is important to consider the limitations imposed on the experiment from atom loss. Ideally, there would be no loss during the time of the Bragg pulse so that the density does not change during the excitation time. We use Bragg beams detuned from the narrow  $^1S_0 \rightarrow ^3P_1$  resonance which allows us to completely suppress loss from the Bragg lasers themselves, but as previously discussed the Rydberg dressing lasers cause a fast loss. Techniques have been developed to interpret Bragg spectra even in the presence of fast loss [103], however, the loss must remain moderate during the time of the pulse. This is the primary limitation

which has stopped us from being able to observe Rydberg dressing. For Rydberg fractions expected to give rise to 100 Hz shifts, we are limited to short excitation times yielding 10 kHz wide peaks, which is currently too small of a fractional change for us to reliably measure. However, if an alternative scheme of Rydberg dressing is developed or another regime is found yielding a slower loss, then it might be possible to resolve these shifts.

#### 5.4.2 Bragg Spectroscopy - Results

In this section, I will show the preliminary results of our work exploring Bragg spectroscopy of a  $^{84}\text{Sr}$  BEC. Owing to limited optical access, we are not able to continuously change the angle between Bragg beams. However, the results provided here show low momentum and high momentum Bragg spectroscopy and would be well suited to detect Rydberg dressing for principal quantum numbers near  $n = 25$ .

It is also worthwhile to note that this technique is very easy to implement in the case of Sr. Owing to the narrow linewidth of the  $^1S_0 \rightarrow ^3P_1$  transition in Sr, Bragg beams are easily generated from a common laser with two synthesizer driven AOMs from an injection locked slave. Powers on the order of a 1 mW for detunings of 100 MHz are sufficient to yield a sufficiently large excitation fraction as well.

As a first experiment with Bragg spectroscopy, we use counter-propagating beams which transfers the greatest momentum, the results of which are plotted in figure 5.5. As we see in the figure, the diffracted atoms are clearly separated from the main cloud and we are able to obtain a narrow spectrum. The x axis of the plot labels the detuning between the two Bragg beams, however, zero on the plot corresponds to the resonance position for free particle dispersion. As can be seen, we can clearly resolve

the shift due to the contact interactions of the BEC.

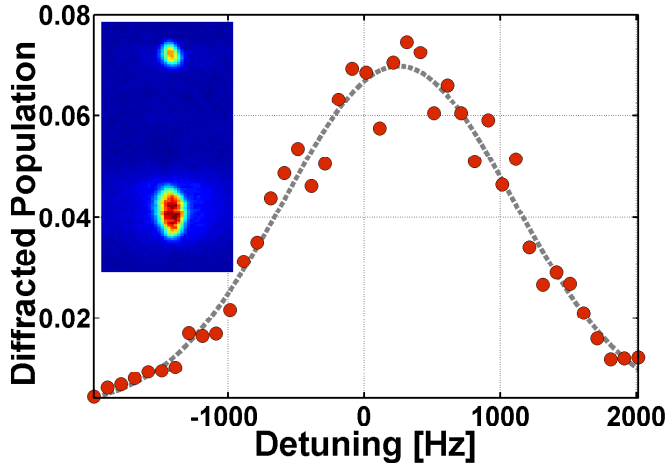


Figure 5.5 : Example Bragg spectra for counter-propagating Bragg beams. Zero detuning corresponds to resonance for free particle dispersion. Inset: Absorption image of BEC and diffracted fraction.

To test our ultimate sensitivity, we perform a set of measurements to see how narrow the Bragg spectrum can be in our system. Narrowing the spectrum is achieved by increasing the exposure time of the Bragg beams and the intensities are reduced accordingly to keep the diffracted population less than 10%. The results are plotted in figure 5.6, and show a few interesting features. For all data, we find that the spectra are better described by a gaussian (blue dashes) than the prediction of equation 5.3 (black lines). This is evidence that we are seeing some type of broadening. This is confirmed in the left panel of figure 5.6 where it is apparent that the measured width is always slightly larger than the width we expect just from time energy uncertainty. Ultimately, exposing for longer fails to narrow the spectra and we are find a minimum width of 2 kHz. The exact reason for this limit is unknown, and will be the source

of future investigation. However, the observed widths are sufficient to measure shifts on the order of 100 Hz.

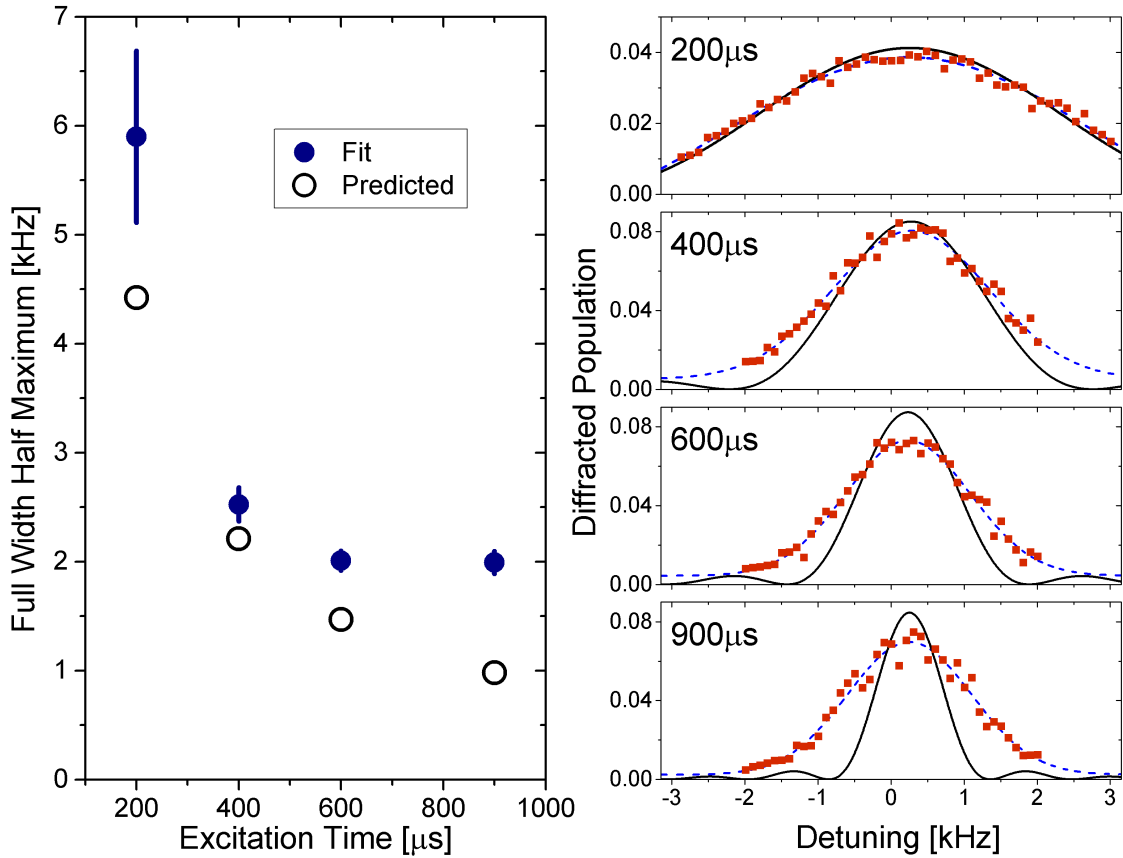


Figure 5.6 : Left Panel: Dependence of the width of Bragg spectra on exposure time. Right Panel: Example Bragg spectra for various exposure times. Data agree well with a gaussian (blue dashes) and appear slightly broader than expected from equation 5.3. This is evidence of broadening present in the system which ultimately limits the width to  $\sim 2$  kHz.

Another test of this method is whether it accurately represents the shift we expect due to contact interactions. The scattering length of  $^{84}\text{Sr}$  is well known and from

knowledge of our trap we can calculate the density of our BEC. By varying the number of atoms in the condensate and the depth of the trap we are able to change the density of the condensate and measure the shift. As shown in figure 5.7 we can easily resolve the shift from resonance, however our results are surprising. Rather than agreeing with the shift expected from the average density ( $\rho_{avg} = \frac{4}{7}\rho_0$ ) as has been found in previous experiments [100, 101], we find the data matches well with the shift expected from the peak density,  $\rho_0$ . At this time, we do not know the source of this discrepancy. The most likely source is the difficulty of accurately knowing our trap frequencies at the low trap depths required to form a BEC.

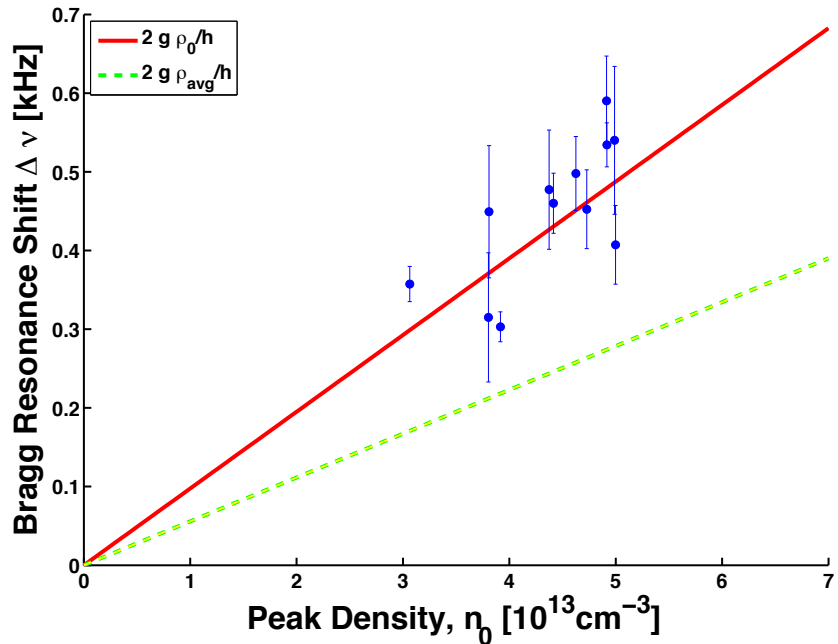


Figure 5.7 : Measurement of shift of Bragg peak as a function of peak density of the condensate. Data appears to agree well with shift expected from peak density rather than average density.

As a final result, we explore the use of shallow angle ( $21^\circ$ ) Bragg spectroscopy. The results of one such experiment is plotted in figure 5.8. With a low momentum transferred, a major concern is the difficulty of spatially resolving the diffracted atoms from the main cloud. However, as our results show, with a long enough time of flight (40 ms for data shown here) we can resolve the peaks and obtain clear spectra. Note here that the x axis is directly the detuning between the Bragg beams. As the resonance position is so close to zero detuning, the peaks corresponding to opposite direction momentum kicks actually overlap. However, since they are spatially separated, it is possible to tell them apart. While choosing the x axis in this manner does not allow one to easily see the shift due to contact interactions as was shown in figure 5.5, we find the resonance position is also consistent with a shift due to contact interactions.

## 5.5 Outlook

With the obtained Bragg spectra shown here, we believe we are capable of resolving shifts on the order of 100 Hz with excitation times of  $200 \mu s$  or longer. However, as mentioned our loss scales have proven too fast so far. Going forward, there are a few possibilities which might help overcome the challenges we've faced so far.

As I mentioned in the introduction, there are two routes to Rydberg dressing of a BEC: off-resonant excitation and Autler-Townes. The work of the Pfau group [25] and ours shows that both of these methods feature fast loss scales. As Rydberg blockade is postulated to be a problem in both methods, it seems that working at even lower principal quantum number might be favorable. This might necessitate

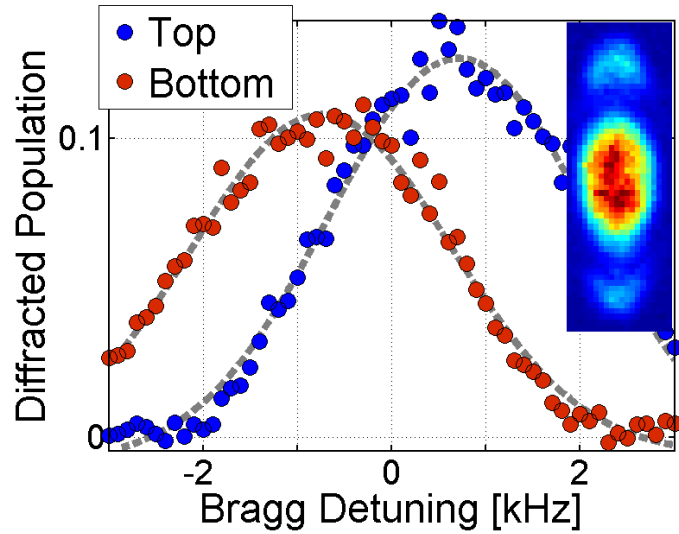


Figure 5.8 : Example spectra for Bragg spectroscopy performed with beams crossed at ( $21^\circ$ ). Inset: Absorption image of BEC and diffracted fraction. Due to the overlap of Bragg peaks with opposite momentum, two diffracted clouds are visible in the image.

looking at even smaller transferred momentum in Bragg spectroscopy, which would likely yield issues of spatially separating the excited atoms. However, our greatest current limitation in this regard arises because we probe in the tight axis of the trap, which has the fastest expansion. If we were to solve the issue of the BEC sloshing in the trap, we could probe in the slowly expanding weakly confined axis of the trap, which would circumvent this problem.

Alternatively, one could work with a lower density BEC. For Sr, this is possible by using  $^{86}\text{Sr}$  which has a scattering length of  $823\ a_0$  typically yielding densities 1 order of magnitude lower. This would potentially be helpful in mitigating the loss processes from Rydberg dressing, however, would also reduce the signal present in

Bragg spectroscopy. At this time it is not clear whether this is a worthwhile course of action as more needs to be learned about the density dependence of the loss processes from Rydberg dressing.

## Chapter 6

### Conclusion

As described in the introduction to this thesis, divalent-electron atoms such as Sr offer many new and exciting opportunities to study novel phenomena with strongly interacting Rydberg gases. These systems feature narrow intercombination lines that provide access high-lying Rydberg states with reduced loss and an optically active core that greatly enriches the possibilities for detecting and manipulating these highly excited atoms. The work presented here lays important groundwork towards future experiments with this system.

In order to best take advantage of the benefits that Sr offers, we have focused on excitation to the  $^3S_1$  Rydberg series of  $^{84}\text{Sr}$ . This work represents the first two-photon excitation to a Rydberg state via an intermediate triplet excited state and shows the promise of this scheme. We have also demonstrated techniques to detect Rydberg atoms even in the absence of electric-field plates and charged particle detection. While ground-state atom loss is not as powerful of a tool for detection as state-selective field ionization, its simplicity makes it useful for certain types of experiments and lowers the level of experimental complication necessary to study Rydberg atoms.

Our first exploration of this system was the creation of ultralong-range molecules. This work provides the first precision measurement of the electron-Sr scattering length and is the first observation of these exotic molecules in a non-alkali system. In the study of these molecules, we have barely scratched the surface of what might be

possible with Sr. The absence of a p-wave shape resonance might yield longer molecule lifetimes compared to Rb, and this would have important consequences for studies of Rydberg atoms in high-density gases, such as a BEC. Further, the presence of doubly excited states can cause perturbations in the Rydberg series that has been predicted to yield stronger oscillator strength for excitation to ultralong-range molecules with a strong permanent dipole moment.

Second, we have explored in detail the effects of Rydberg-Rydberg interactions on Autler-Townes spectra. Using a modified mean-field treatment to describe energy-level shifts and dephasing, we are able to accurately capture the early-time dynamics of this rich system. Our data shows suggestive evidence of the source of large dephasing rates that we see. Understanding of this dephasing is essential, as it is currently the largest roadblock in the path to observing Rydberg dressing of a BEC. Further work towards this end will hopefully confirm our suspicions that a population in lower-lying p states is the cause of the loss, in which case it might be possible to remove the population via microwave transitions and lessen the effect.

Finally, we have laid out a course to the eventual detection of Rydberg dressing in a BEC via Bragg spectroscopy. This method provides a clear signature of the effect of Rydberg-dressed interactions and provides smoking-gun evidence of their long-ranged nature. Towards this end, we have shown preliminary results that demonstrate the sensitivity of this technique and give confidence that will be useful provided the loss caused by Rydberg dressing can be reduced.

As a final note to the reader, I hope I have been able to convince you that divalent-electron Rydberg atoms show great promise for future work exploring strongly interacting dipolar gases. With the promise of a wide variety of exciting experiments in

## Appendix A

### Matlab Code

For reference I am attaching Matlab code which was used in chapter 4. The first program, shiftHistogramv3.m, is used to calculate the distribution of shifts for a homogeneous gas. This program runs on its own with no extra input needed.

```

function shiftHistogramv2
%shiftHistogram - Builds histogram to fit distribution of shifts at a
given
%           density
% v2          - Adds cutoff at blockade radius

%Open matlabpool if none open
if matlabpool('size') == 0
    matlabpool open
end
close all

numPart = 10^4;
numBins = 10^4;
maxShift = 10^3;
lengthScale = numPart^(1/3);
density = numPart/(lengthScale^3);
x = rand(numPart,1).*lengthScale;
y = rand(numPart,1).*lengthScale;
z = rand(numPart,1).*lengthScale;
shiftVect = zeros(length(x),1);
shiftVect1xRhoB = zeros(length(x),1); scaledShiftVect1xRhoB =
zeros(length(x),1);
shiftVect5xRhoB = zeros(length(x),1); scaledShiftVect5xRhoB =
zeros(length(x),1);
shiftVect10xRhoB = zeros(length(x),1); scaledShiftVect10xRhoB =
zeros(length(x),1);
shiftVect20xRhoB = zeros(length(x),1); scaledShiftVect20xRhoB =
zeros(length(x),1);
shiftVect30xRhoB = zeros(length(x),1); scaledShiftVect30xRhoB =
zeros(length(x),1);
shiftVect40xRhoB = zeros(length(x),1); scaledShiftVect40xRhoB =
zeros(length(x),1);
shiftVect50xRhoB = zeros(length(x),1); scaledShiftVect50xRhoB =
zeros(length(x),1);
nnVect = 10*ones(length(x),1);
rB1 = 1; rB5 = 5^(1/3); rB10 = 10^(1/3); rB20 = 20^(1/3);
rB30 = 30^(1/3); rB40 = 40^(1/3); rB50 = 50^(1/3);
parfor i = 1:numPart
    for j = 1:numPart
        if j~=i
            r = ((x(j)-x(i))^2 + (y(j)-y(i))^2 + (z(j)-z(i))^2)^(1/2);
            shiftVect(i) = r^-6 + shiftVect(i);
            if r > rB1
                shiftVect1xRhoB(i) = 1/(r^6) + shiftVect1xRhoB(i);
            else
                shiftVect1xRhoB(i) = shiftVect1xRhoB(i);
            end
            if r > rB5

```

```

        shiftVect5xRhoB(i) = 1/(r^6) + shiftVect5xRhoB(i);
    else
        shiftVect5xRhoB(i) = shiftVect5xRhoB(i);
    end
    if r > rB10
        shiftVect10xRhoB(i) = 1/(r^6) + shiftVect10xRhoB(i);
    else
        shiftVect10xRhoB(i) = shiftVect10xRhoB(i);
    end
    if r > rB20
        shiftVect20xRhoB(i) = 1/(r^6) + shiftVect20xRhoB(i);
    else
        shiftVect20xRhoB(i) = shiftVect20xRhoB(i);
    end
    if r > rB30
        shiftVect30xRhoB(i) = 1/(r^6) + shiftVect30xRhoB(i);
    else
        shiftVect30xRhoB(i) = shiftVect30xRhoB(i);
    end
    if r > rB40
        shiftVect40xRhoB(i) = 1/(r^6) + shiftVect40xRhoB(i);
    else
        shiftVect40xRhoB(i) = shiftVect40xRhoB(i);
    end
    if r > rB50
        shiftVect50xRhoB(i) = 1/(r^6) + shiftVect50xRhoB(i);
    else
        shiftVect50xRhoB(i) = shiftVect50xRhoB(i);
    end
    scaledShiftVect1xRhoB(i) = shiftVect1xRhoB(i)*(density*1);
    scaledShiftVect5xRhoB(i) = shiftVect5xRhoB(i)*(density*5);
    scaledShiftVect10xRhoB(i) =
        shiftVect10xRhoB(i)*(density*10);
    scaledShiftVect20xRhoB(i) =
        shiftVect20xRhoB(i)*(density*20);
    scaledShiftVect30xRhoB(i) =
        shiftVect30xRhoB(i)*(density*30);
    scaledShiftVect40xRhoB(i) =
        shiftVect40xRhoB(i)*(density*40);
    scaledShiftVect50xRhoB(i) =
        shiftVect50xRhoB(i)*(density*50);
    end
end
bins = linspace(0,maxShift,numBins);
scaleBins = linspace(0,10,1000);
rHundredsBins = linspace(0,10,1000);
histShift = histc(shiftVect,bins);
histShift1xRhoB = histc(shiftVect1xRhoB,bins); scaledHistShift1XRhoB
= histc(scaledShiftVect1xRhoB,scaleBins);

```

```

histShift5xRhoB = histc(shiftVect5xRhoB,bins);    scaledHistShift5XRhoB
= histc(scaledShiftVect5xRhoB,scaleBins);
histShift10xRhoB = histc(shiftVect10xRhoB,bins);
scaledHistShift10XRhoB = histc(scaledShiftVect10xRhoB,scaleBins);
histShift20xRhoB = histc(shiftVect20xRhoB,bins);
scaledHistShift20XRhoB = histc(scaledShiftVect20xRhoB,scaleBins);
histShift30xRhoB = histc(shiftVect30xRhoB,bins);
scaledHistShift30XRhoB = histc(scaledShiftVect30xRhoB,scaleBins);
histShift40xRhoB = histc(shiftVect40xRhoB,bins);
scaledHistShift40XRhoB = histc(scaledShiftVect40xRhoB,scaleBins);
histShift50xRhoB = histc(shiftVect50xRhoB,bins);
scaledHistShift50XRhoB = histc(scaledShiftVect50xRhoB,scaleBins);

%counts = nnVect./numPart;
probR = numPart/100.*4*pi.*rHundredthsBins.^2.*exp(-
(4/3).*pi*rHundredthsBins.^3);

figure(1)
plot(scaleBins,smooth(scaledHistShift1XRhoB),'sk','MarkerSize',
6,'MarkerFaceColor','k');hold on;
plot(scaleBins,smooth(scaledHistShift5XRhoB),'sb','MarkerSize',
6,'MarkerFaceColor','b');hold on;
plot(scaleBins,smooth(scaledHistShift10XRhoB),'sr','MarkerSize',
6,'MarkerFaceColor','r');hold on;
plot(scaleBins,smooth(scaledHistShift20XRhoB),'sg','MarkerSize',
6,'MarkerFaceColor','g');hold on;
plot(scaleBins,smooth(scaledHistShift30XRhoB),'dk','MarkerSize',
6,'MarkerFaceColor','k');hold on;
plot(scaleBins,smooth(scaledHistShift40XRhoB),'db','MarkerSize',
6,'MarkerFaceColor','b');hold on;
plot(scaleBins,smooth(scaledHistShift50XRhoB),'dr','MarkerSize',
6,'MarkerFaceColor','r');hold on;
set(gca,'FontSize',24,'FontWeight','Demi')
legend('\rho/\rho_B = 1','\rho/\rho_B = 5','\rho/\rho_B = 10','\rho/
\rho_B = 20',...
      '\rho/\rho_B = 30','\rho/\rho_B = 40','\rho/\rho_B =
50','FontSize',24,'FontWeight','Bold')
xlabel('V/ \rho_B \rho [2\pi C_6 / h]','FontSize',
28,'FontWeight','Bold')
ylabel('Occurrences','FontSize',28,'FontWeight','Bold')
end

```

obeSolverDataCompareSummaryv3.m is used for the calculation of Autler-Townes spectra. This program must be called with an argument [data] in order to read in the data which will be plotted for comparison to theory. The program looks for a specific structure to the data, but this is easily modified by the user.

```

function [ output_args ] =
obeSolverDataCompareSummaryv3( data1,data2 )
% obeSolverDataCompareSummary - Solves the optical bloch equations
using the
%           local density approximation and compares to spectra
data
%           with simple plots for presentation
% v2 - Uses smaller number of spectra for clarity
% v3 - Combines plots
% Initialize parallel worker
%Open matlabpool if none open
if matlabpool('size') == 0
    matlabpool open
end
close all
atomicMass = 1.66*10^-27;
mSr = 84*atomicMass;
kB = 1.38*10^-23;

%% Options
density = 'Low'; %Choose density of data, valid options 'High', 'Low'
plotFits = 1;      %1 to plot all fits, 0 to suppress

%%Unchanged parameters
Omega12      = 2*pi*2.4*10^6;
Delta12       = 0;
Gamma10       = 2*pi*7.5*10^3;
Gamma1Dephase = 2*pi*30*10^3;
Gamma21       = (1/3)*2*pi*50*10^3;
Gamma2Loss    = (2/3)*2*pi*50*10^3;
Gamma2DephaseLaser = 2*pi*300*10^3;
C6Hz          = C6(24);
w1            = 2*pi*11.6;
w2            = 2*pi*18.3;
w3            = 2*pi*131.3;
omegarbar     = (w1*w2*w3)^(1/3);
scaleDensities = [0.0225 0.0725 0.1305 0.1955 0.2685 0.35 0.442 0.548
0.676 0.8735]; %Densities chosen to accurately weight spectra

% Make vector of changed variables
dephaseVect = [0 0 1 2];
VrydrydVect = [0 1 1 1];

%% Loop through high and low density data
if strcmpi(density,'Low') || strcmpi(density,'All')
    figHan1 = figure; figHan2 = figure;
    figHan3 = figure; figHan4 = figure;
    for i =4:length(data1.avgVar)

```

```

%Read in data and store in temp variables
indVarLD = -data2.avgIndVar{i} + 93.34;
specLD = data2.avgNumAtom{i};
numPulsesLD = data2.avgVar3{i};
pulseWidthLD = data2.avgVar2{i};

sortSpec = sort(specLD);
n0LD = mean(sortSpec(end-10:end-5));
normSpecLD = n0LD - ((n0LD - specLD)./numPulsesLD);
Omega01 = 2*pi*data2.avgVar{i}*10^3;
tempLD = (data2.avgTempX{i} + data2.avgTempY{i})/2;
tLD = mean(tempLD(1:3))*10^-9;
peakDensity = (n0LD/((2*pi*kB*tLD)/
(mSr*omegarbar^2))^(3/2));

%Collect relevant parameters into vector
paramVect(1) = Omega01; paramVect(9) =
C6(24); paramVect(2) = Omega12; paramVect(10) =
pulseWidthLD.*10^-6; paramVect(3) = Delta12; paramVect(11) =
(pulseWidthLD + 50).*10^-6; paramVect(4) = Gamma10; paramVect(12) =
(pulseWidthLD + 50).*10^-6; paramVect(5) = Gamma1Dephase; paramVect(13) =
tLD; paramVect(6) = Gamma21; paramVect(14) =
w1; paramVect(7) = Gamma2Loss; paramVect(15) =
w2; paramVect(8) = Gamma2DephaseLaser; paramVect(16) =
w3;

%Loop over changed variables
%h = waitbar(0,'Calculating spectra');

for k = 1:length(VrydrydVect)
    paramVect(17) = dephaseVect(k);
    paramVect(18) = VrydrydVect(k);
    spectra =
obeSpectraSolve(peakDensity,scaleDensities,indVarLD,paramVect);
    n0Spec = mean(spectra([1:3 end-3:end]));

    if plotFits
        if k==1
            set(0,'CurrentFigure',figHan1);
            titleText = '\alpha = 0 \beta = 0';
        elseif k == 2
            set(0,'CurrentFigure',figHan2);
    end
end

```

```

        titleText = '\alpha = 1 \beta = 0';
    elseif k ==3
        set(0,'CurrentFigure',figHan3);
        titleText = '\alpha = 1 \beta = 1';
    elseif k ==4
        set(0,'CurrentFigure',figHan4);
        titleText = '\alpha = 1 \beta = 2';
    end
    figText = strcat('\Omega_{01} =
',num2str(0mega01/(2*pi*10^3)), ' kHz');

        subplot(length(data1.avgVar)-3,1,i-3)
        plot(indVarLD,normSpecLD./
n0LD,'sb','MarkerSize',8,'MarkerFaceColor','b'); hold on;
        plot(indVarLD,spectra./n0Spec,'-
r','LineWidth',5); hold on;
        set(gca,'FontSize',24,'FontWeight','Demi')
        xlim([indVarLD(length(indVarLD)) indVarLD(1)])
        ylim([min(normSpecLD./n0LD) 1])
        if i == 4
            title(titleText,'FontSize',
32,'FontWeight','Bold')
        end
        if i == length(data1.avgVar)
            xlabel('Delta_{01}/2\pi
[MHz]','FontSize',30,'FontWeight','Bold')

        end
        if i == 5 && k == 1
            ylabel('Relative Atom Number','FontSize',
30,'FontWeight','Bold')
        end
        if k == 1
            text(-0.25 * indVarLD(1), min(normSpecLD./
n0LD) + 0.25*(1-min(normSpecLD./n0LD)),figText,'FontSize',
24,'FontWeight','Bold')
        end
    end
end
if strcmp(density,'High') || strcmp(density,'All')
    figHan1 = figure; figHan2 = figure;
    figHan3 = figure; figHan4 = figure;
    for i =1:length(data1.avgVar)-3
        %Read in data and store in temp variables
        indVarHD = -data1.avgIndVar{i} + 93.34;
        specHD = data1.avgNumAtom{i};
        numPulsesHD = data1.avgVar3{i};
        pulseWidthHD = data1.avgVar2{i};

```

```

sortSpec = sort(specHD);
n0HD = mean(sortSpec(end-10:end-5));
normSpecHD = n0HD-((n0HD - specHD)./numPulsesHD);
Omega01 = 2*pi*data1.avgVar{i}.*10^3;
tempHD = (data1.avgTempX{i} + data1.avgTempY{i})/2;
tHD = mean(tempHD(1:3)).*10^-9;
peakDensity = (n0HD/((2*pi*kB*tHD)/
(mSr*omegarbar^2))^(3/2));

%Collect relevant parameters into vector
paramVect(1) = Omega01; paramVect(9) =
C6(24);
paramVect(2) = Omega12; paramVect(10) =
pulseWidthHD.*10^-6; paramVect(11) =
(pulseWidthHD + 50).*10^-6; paramVect(12) =
(pulseWidthHD + 50).*10^-6; paramVect(13) =
paramVect(5) = Gamma1Dephase; tHD;
paramVect(6) = Gamma21; paramVect(14) =
w1; paramVect(7) = Gamma2Loss; paramVect(15) =
w2; paramVect(8) = Gamma2DephaseLaser; paramVect(16) =
w3;

%Loop over changed variables
%h = waitbar(0,'Calculating spectra');

for k = 1:length(VrydrydVect)
    paramVect(17) = dephaseVect(k);
    paramVect(18) = VrydrydVect(k);
    spectra =
obeSpectraSolve(peakDensity,scaleDensities,indVarHD,paramVect);
    n0Spec = mean(spectra([1:3 end-3:end]));

    if plotFits
        if k==1
            set(0,'CurrentFigure',figHan1);
            titleText = '\alpha = 0 \beta = 0';
        elseif k == 2
            set(0,'CurrentFigure',figHan2);
            titleText = '\alpha = 1 \beta = 0';
        elseif k ==3
            set(0,'CurrentFigure',figHan3);
            titleText = '\alpha = 1 \beta = 1';
        elseif k ==4
    end
end

```

```

        set(0,'CurrentFigure',figHan4);
        titleText = '\alpha = 1 \beta = 2';
    end
    figText = strcat('\Omega_{01} =
',num2str(Omega01/(2*pi*10^3)), ' kHz');

    subplot(length(data1.avgVar)-3,1,length(data1.avgVar)-2-i)
        plot(indVarHD,normSpecHD./
n0HD,'sb','MarkerSize',8,'MarkerFaceColor','b'); hold on;
        plot(indVarHD,spectra./n0Spec,'-
r','LineWidth',5); hold on;
        set(gca,'FontSize',24,'FontWeight','Demi')
        xlim([indVarHD(length(indVarHD)) indVarHD(1)])
        ylim([min(normSpecHD./n0HD) 1])
        if i == 3
            title(titleText,'FontSize',
32,'FontWeight','Bold')
        end
        if i == 2 && k == 1
            ylabel('Relative Atom Number','FontSize',
30,'FontWeight','Bold')
        end
        if i == 1
            xlabel('\Delta_{01}/2\pi
[MHz]','FontSize',30,'FontWeight','Bold')
        end
        if k == 1
            text(-0.25 * indVarHD(1),
min(normSpecHD./n0HD) + 0.25*(1-min(normSpecHD./
n0HD)),figText,'FontSize',24,'FontWeight','Bold')
        end
    end
end

function spectra =
obeSpectraSolve(peakDensity,scaleDensities,detuningVect,paramVect)
%Unpack passed variables
densityVect = peakDensity.*scaleDensities;
Omega01      = paramVect(1);
Omega12      = paramVect(2);
Delta12      = paramVect(3);
Gamma10      = paramVect(4);
Gamma1Dephase = paramVect(5);

```

```

Gamma21           = paramVect(6);
Gamma2Loss        = paramVect(7);
Gamma2DephaseLaser = paramVect(8);
C6               = paramVect(9);
tRed             = paramVect(10);
tUV              = paramVect(11);
tTotal            = paramVect(12);
T                = paramVect(13);
w1               = paramVect(14);
w2               = paramVect(15);
w3               = paramVect(16);
cDephase          = paramVect(17);
cInt              = paramVect(18);
initialConditions = [1 0 0 0 0 0]; % [p00 p11 p22 p01 p12 p02]

%Initialize vectors and loop over densities
scaledSpectra = zeros(length(densityVect),length(detuningVect),3);
groundPopulation =
zeros(length(densityVect),length(detuningVect));
for j=1:length(densityVect);
    temp1 = zeros(length(detuningVect),1);
    temp2 = zeros(length(detuningVect),1);
    temp3 = zeros(length(detuningVect),1);
    parfor i = 1:length(detuningVect)
        fitCall = @(t,rho)
funcOBE(t,rho,Omega01,Omega12,2*pi*detuningVect(i)*10^6,Delta12,Gamma1
0,Gamma1Dephase,
Gamma21,Gamma2Loss,Gamma2DephaseLaser,C6,tRed,tUV,densityVect(j),cDep
ase,cInt);
        [~,rho] = ode45(fitCall,[0 tTotal], initialConditions);
        temp1(i) = rho(length(rho),1);
        temp2(i) = rho(length(rho),2);
        temp3(i) = rho(length(rho),3);
    end
    scaledSpectra(j,:,:) = [temp1 temp2
temp3].*densityWeight(densityVect(j),peakDensity,T,w1,w2,w3);
    groundPopulation(j,:) = (temp1 + temp2 + (1/3)*temp3).**
densityWeight(densityVect(j),peakDensity,T,w1,w2,w3);
end
spectra = trapz(densityVect,groundPopulation,1);

end

function rhoOut =
funcOBE(t,rho,Omega01,Omega12,Delta01,Delta12,Gamma10,Gamma1Dephase,
Gamma21,Gamma2Loss,Gamma2DephaseLaser,C6,tRed,tUV,Density,cDephase,cIn
t)
    %This function defines the optical bloch equations for a 3 level
    %ladder system involving interacting Rydberg states
    %Define constants

```

```

rB = (C6/(2*Omega12))^(1/6);
Vrydryd = cInt*4*pi*C6*Density/(3*rB^3);
Gamma2DephaseRyd = cDephase*4*pi*C6*Density/(3*rB^3);

%Determine if red and UV lasers are on... this method 8X faster
than
%using heaviside functions
if t <= tRed
    redLogic = 1;
else
    redLogic = 0;
end

if t <= tUV
    uvLogic = 1;
else
    uvLogic = 0;
end

% Initialize rhoOut
rhoOut = zeros(6,1);
% Get current values of density matrix
p00 = rho(1); p01 = rho(4);
p11 = rho(2); p12 = rho(5);
p22 = rho(3); p02 = rho(6);

rhoOut(1) = Gamma10* p11 - Omega01*imag(p01)*redLogic;
rhoOut(2) = -Gamma10*p11 + Gamma21*p22 +
Omega01*imag(p01)*redLogic - Omega12*imag(p12)*uvLogic;
rhoOut(3) = -(Gamma21+Gamma2Loss)*p22 + Omega12*imag(p12)*uvLogic;
rhoOut(4) = -((Gamma10+Gamma1Dephase)/2+1i*Delta01)*p01...
- 1i*Omega01/2*(p11-p00)*redLogic
+1i*Omega12/2*p02*uvLogic;
rhoOut(5) = -((Gamma21+Gamma2Loss+Gamma2DephaseLaser+
(Gamma2DephaseRyd*p22)+Gamma10)/2 ...
+ 1i*(Delta12-Vrydryd*p22))*p12-1i*Omega12/2*(p22-
p11)*uvLogic - 1i*Omega01/2*p02*redLogic;
rhoOut(6) = -((Gamma1Dephase+Gamma21+Gamma2Loss+Gamma2DephaseLaser
+(Gamma2DephaseRyd*p22))/2+1i*(Delta01+Delta12-Vrydryd*p22))*p02...
+ 1i*Omega12/2*p01*uvLogic-1i*Omega01/2*p12*redLogic;
end

function C6 = C6(n)
%Calculate C6 in Hz * m^6
a = -2.387*10^-3; b = 1.211; c1 = -21.18;
hbar = 1.06 * 10^-34;
hartree = 4.36*10^-18;% J
aBohr = 5.29*10^-11;
C6atomic = n^11*(a*n^2 + b*n + c1);
C6 = C6atomic*hartree*aBohr^6/hbar;

```

```
end

function densityWeight = densityWeight(n,n0,T,w1,w2,w3)
    %Weighting function for local density approximation
    atomicmass = 1.66*10^-27;
    mSr = 84*atomicmass;
    kB = 1.38*10^-23;
    densityWeight = ((2.*pi)./(w1.*w2.*w3)).*((2.*kB.*T)./
mSr).^(3/2).*(log(n0./n)).^(1/2);
end
```

## Bibliography

- [1] V. Gurarie and L. Radzihovsky, “Resonantly paired fermionic superfluids,” *Annals of Physics*, vol. 322, no. 1, pp. 2 – 119, 2007. January Special Issue 2007.
- [2] L. Radzihovsky and D. E. Sheehy, “Imbalanced Feshbach-resonant Fermi gases,” *Reports on Progress in Physics*, vol. 73, no. 7, p. 076501, 2010.
- [3] I. Bloch, J. Dalibard, and W. Zwerger, “Many-body physics with ultracold gases,” *Rev. Mod. Phys.*, vol. 80, pp. 885–964, Jul 2008.
- [4] D. Comparat and P. Pillet, “Dipole blockade in a cold Rydberg atomic sample,” *J. Opt. Soc. Am. B*, vol. 27, pp. A208–A232, Jun 2010.
- [5] L. D. Carr, D. DeMille, R. V. Krems, and J. Ye, “Cold and ultracold molecules: science, technology and applications,” *New Journal of Physics*, vol. 11, no. 5, p. 055049, 2009.
- [6] A. Griesmaier, J. Werner, S. Hensler, J. Stuhler, and T. Pfau, “Bose-Einstein Condensation of Chromium,” *Phys. Rev. Lett.*, vol. 94, p. 160401, Apr 2005.
- [7] M. Lu, S. H. Youn, and B. L. Lev, “Trapping Ultracold Dysprosium: A Highly Magnetic Gas for Dipolar Physics,” *Phys. Rev. Lett.*, vol. 104, p. 063001, Feb 2010.

- [8] M. Baranov, “Theoretical progress in many-body physics with ultracold dipolar gases,” *Physics Reports*, vol. 464, no. 3, pp. 71 – 111, 2008.
- [9] L. Santos, G. V. Shlyapnikov, and M. Lewenstein, “Roton-Maxon Spectrum and Stability of Trapped Dipolar Bose-Einstein Condensates,” *Phys. Rev. Lett.*, vol. 90, p. 250403, Jun 2003.
- [10] H. P. Büchler, E. Demler, M. Lukin, A. Micheli, N. Prokof’ev, G. Pupillo, and P. Zoller, “Strongly Correlated 2D Quantum Phases with Cold Polar Molecules: Controlling the Shape of the Interaction Potential,” *Phys. Rev. Lett.*, vol. 98, p. 060404, Feb 2007.
- [11] G. Pupillo, A. Micheli, M. Boninsegni, I. Lesanovsky, and P. Zoller, “Strongly Correlated Gases of Rydberg-Dressed Atoms: Quantum and Classical Dynamics,” *Phys. Rev. Lett.*, vol. 104, p. 223002, Jun 2010.
- [12] R. M. W. van Bijnen, S. Smit, K. A. H. van Leeuwen, E. J. D. Vredenbregt, and S. J. J. M. F. Kokkelmans, “Adiabatic formation of Rydberg crystals with chirped laser pulses,” *Journal of Physics B: Atomic, Molecular and Optical Physics*, vol. 44, no. 18, p. 184008, 2011.
- [13] N. Henkel, R. Nath, and T. Pohl, “Three-Dimensional Roton Excitations and Supersolid Formation in Rydberg-Excited Bose-Einstein Condensates,” *Phys. Rev. Lett.*, vol. 104, p. 195302, May 2010.
- [14] I. Lesanovsky, “Many-Body Spin Interactions and the Ground State of a Dense Rydberg Lattice Gas,” *Phys. Rev. Lett.*, vol. 106, p. 025301, Jan 2011.

- [15] F. Maucher, N. Henkel, M. Saffman, W. Królikowski, S. Skupin, and T. Pohl, “Rydberg-Induced Solitons: Three-Dimensional Self-Trapping of Matter Waves,” *Phys. Rev. Lett.*, vol. 106, p. 170401, Apr 2011.
- [16] N. Prokof’ev, “What makes a crystal supersolid?,” *Advances in Physics*, vol. 56, no. 2, pp. 381–402, 2007.
- [17] M. Boninsegni, “Supersolid Phases of Cold Atom Assemblies,” *Journal of Low Temperature Physics*, vol. 168, no. 3-4, pp. 137–149, 2012.
- [18] M. Boninsegni and N. V. Prokof’ev, “Colloquium : Supersolids: What and where are they?,” *Rev. Mod. Phys.*, vol. 84, pp. 759–776, May 2012.
- [19] F. Cinti, P. Jain, M. Boninsegni, A. Micheli, P. Zoller, and G. Pupillo, “Supersolid Droplet Crystal in a Dipole-Blockaded Gas,” *Phys. Rev. Lett.*, vol. 105, p. 135301, Sep 2010.
- [20] J. R. R. Ph.D., “Xxxiv. on the structure of the line-spectra of the chemical elements,” *Philosophical Magazine Series 5*, vol. 29, no. 179, pp. 331–337, 1890.
- [21] C. L. Vaillant, M. P. A. Jones, and R. M. Potvliege, “Long-range Rydberg-Rydberg interactions in calcium, strontium and ytterbium,” *Journal of Physics B: Atomic, Molecular and Optical Physics*, vol. 45, p. 135004, Mar. 2012.
- [22] P. McQuillen, X. Zhang, T. Strickler, F. B. Dunning, and T. C. Killian, “Imaging the evolution of an ultracold strontium Rydberg gas,” *Phys. Rev. A*, vol. 87, p. 013407, Jan 2013.

- [23] G. Lochead, D. Boddy, D. P. Sadler, C. S. Adams, and M. P. A. Jones, “Number-resolved imaging of excited-state atoms using a scanning autoionization microscope,” *Phys. Rev. A*, vol. 87, p. 053409, May 2013.
- [24] W. Li, T. Pohl, J. M. Rost, S. T. Rittenhouse, H. R. Sadeghpour, J. Nipper, B. Butscher, J. B. Balewski, V. Bendkowsky, R. Löw, and T. Pfau, “A homonuclear molecule with a permanent electric dipole moment.,” *Science*, vol. 334, p. 1110, Nov. 2011.
- [25] J. B. Balewski, A. T. Krupp, A. Gaj, S. Hofferberth, R. Lw, and T. Pfau, “Rydberg dressing: understanding of collective many-body effects and implications for experiments,” *New Journal of Physics*, vol. 16, no. 6, p. 063012, 2014.
- [26] Y.-Y. Jau, A. M. Hankin, T. Keating, I. H. Deutsch, and G. W. Biedermann, “Entangling Atomic Spins with a Strong Rydberg-Dressed Interaction,” *ArXiv e-prints*, Jan. 2015.
- [27] Y. N. M. de Escobar, P. G. Mickelson, M. Yan, B. J. DeSalvo, S. B. Nagel, and T. C. Killian, “Bose-Einstein Condensation of  $^{84}\text{Sr}$ ,” *Phys. Rev. Lett.*, vol. 103, p. 200402, Nov 2009.
- [28] P. G. Mickelson, Y. N. Martinez de Escobar, M. Yan, B. J. DeSalvo, and T. C. Killian, “Bose-Einstein condensation of  $^{88}\text{Sr}$  through sympathetic cooling with  $^{87}\text{Sr}$ ,” *Phys. Rev. A*, vol. 81, p. 051601, May 2010.
- [29] B. J. DeSalvo, M. Yan, P. G. Mickelson, Y. N. Martinez de Escobar, and T. C. Killian, “Degenerate Fermi Gas of  $^{87}\text{Sr}$ ,” *Phys. Rev. Lett.*, vol. 105, p. 030402, Jul 2010.

- [30] S. Stellmer, M. K. Tey, B. Huang, R. Grimm, and F. Schreck, “Bose-Einstein Condensation of Strontium,” *Phys. Rev. Lett.*, vol. 103, p. 200401, Nov 2009.
- [31] M. K. Tey, S. Stellmer, R. Grimm, and F. Schreck, “Double-degenerate Bose-Fermi mixture of strontium,” *Phys. Rev. A*, vol. 82, p. 011608, Jul 2010.
- [32] S. Stellmer, M. K. Tey, R. Grimm, and F. Schreck, “Bose-Einstein condensation of  $^{86}\text{Sr}$ ,” *Phys. Rev. A*, vol. 82, p. 041602, Oct 2010.
- [33] S. B. Nagel, C. E. Simien, S. Laha, P. Gupta, V. S. Ashoka, and T. C. Killian, “Magnetic trapping of metastable  $^3P_2$  atomic strontium,” *Phys. Rev. A*, vol. 67, p. 011401, Jan 2003.
- [34] S. Stellmer and F. Schreck, “Reservoir spectroscopy of  $5s5p\ ^3P_2 \sim 5snd\ ^3D_{1,2,3}$  transitions in strontium,” *Phys. Rev. A*, vol. 90, p. 022512, Aug 2014.
- [35] P. G. Mickelson, Y. N. M. de Escobar, P. Anzel, B. J. DeSalvo, S. B. Nagel, A. J. Traverso, M. Yan, and T. C. Killian, “Repumping and spectroscopy of laser-cooled Sr atoms using the  $(5s5p)\ 3\ P\ 2$  ( $5s4d\ 3\ D\ 2$ ) transition,” *Journal of Physics B: Atomic, Molecular and Optical Physics*, vol. 42, no. 23, p. 235001, 2009.
- [36] J. Carriou and P. Luc, *Atlas du Spectre d'Absorption de la Molécule Tellure*. Laboratoire Aime-Cotton, CNRS II, Orsay, France, 1980.
- [37] J. E. Sansonetti and G. Nave, “Wavelengths, transition probabilities, and energy levels for the spectrum of neutral strontium (sri),” *Journal of Physical and Chemical Reference Data*, vol. 39, no. 3, pp. –, 2010.

- [38] M. Yan, R. Chakraborty, A. Mazurenko, P. G. Mickelson, Y. N. M. de Escobar, B. J. DeSalvo, and T. C. Killian, “Numerical modeling of collisional dynamics of Sr in an optical dipole trap,” *Phys. Rev. A*, vol. 83, p. 032705, Mar 2011.
- [39] R. Drever, J. Hall, F. Kowalski, J. Hough, G. Ford, A. Munley, and H. Ward, “Laser phase and frequency stabilization using an optical resonator,” *Applied Physics B*, vol. 31, no. 2, pp. 97–105, 1983.
- [40] M. Weissbluth, *Atoms and molecules*. Academic Press, 1978.
- [41] R. Beigang, K. Lcke, D. Schmidt, A. Timmermann, and P. J. West, “One-Photon Laser Spectroscopy of Rydberg Series from Metastable Levels in Calcium and Strontium,” *Physica Scripta*, vol. 26, no. 3, p. 183, 1982.
- [42] S. Kunze, R. Hohmann, H.-J. Kluge, J. Lantzsch, L. Monz, J. Stenner, K. Stratmann, K. Wendt, and K. Zimmer, “Lifetime measurements of highly excited Rydberg states of strontium I,” *Zeitschrift fr Physik D Atoms, Molecules and Clusters*, vol. 27, no. 2, pp. 111–114, 1993.
- [43] C. Greene, A. Dickinson, and H. Sadeghpour, “Creation of polar and nonpolar ultra-long-range Rydberg molecules,” *Physical Review Letters*, vol. 85, p. 2458, Sept. 2000.
- [44] V. Bendkowsky, B. Butscher, J. Nipper, J. P. Shaffer, R. Löw, and T. Pfau, “Observation of ultralong-range Rydberg molecules.,” *Nature*, vol. 458, p. 1005, Apr. 2009.
- [45] J. Tallant, S. T. Rittenhouse, D. Booth, H. R. Sadeghpour, and J. P. Shaffer,

- “Observation of Blueshifted Ultralong-Range Cs<sub>2</sub> Rydberg Molecules,” *Physical Review Letters*, vol. 109, p. 173202, Oct. 2012.
- [46] M. A. Bellos, R. Carollo, J. Banerjee, E. E. Eyler, P. L. Gould, and W. C. Stwalley, “Excitation of Weakly Bound Molecules to Trilobitelike Rydberg States,” *Physical Review Letters*, vol. 111, p. 053001, July 2013.
- [47] H. Saßmannshausen, F. Merkt, and J. Deiglmayr, “Experimental Characterization of Singlet Scattering Channels in Long-Range Rydberg Molecules,” *Phys. Rev. Lett.*, vol. 114, p. 133201, Mar 2015.
- [48] a. T. Krupp, A. Gaj, J. B. Balewski, P. Ilzhöfer, S. Hofferberth, R. Löw, T. Pfau, M. Kurz, and P. Schmelcher, “Alignment of D-State Rydberg Molecules,” *Physical Review Letters*, vol. 112, p. 143008, Apr. 2014.
- [49] D. A. Anderson, S. A. Miller, and G. Raithel, “Photoassociation of Long-Range *nD* Rydberg Molecules,” *Phys. Rev. Lett.*, vol. 112, p. 163201, Apr 2014.
- [50] A. Gaj, A. T. Krupp, J. B. Balewski, S. Hofferberth, and T. Pfau, “Ultracold atom-electron interaction: from two to many-body physics,” 2014.
- [51] J. Millen, G. Lochead, and M. Jones, “Two-Electron Excitation of an Interacting Cold Rydberg Gas,” *Physical Review Letters*, vol. 105, pp. 1–4, Nov. 2010.
- [52] R. Mukherjee, J. Millen, R. Nath, M. P. a. Jones, and T. Pohl, “Many-body physics with alkaline-earth Rydberg lattices,” *Journal of Physics B: Atomic, Molecular and Optical Physics*, vol. 44, p. 184010, Sept. 2011.

- [53] E. Fermi, “Sopra lo spostamento per pressione delle righe elevate delle serie spettrali,” *Nuovo Cimento*, vol. 11, p. 157, 1934.
- [54] A. Omont, “On the theory of collisions of atoms in Rydberg states with neutral particles,” *Journal de Physique*, vol. 38, p. 1343, 1977.
- [55] Y. N. Martinez de Escobar, P. G. Mickelson, P. Pellegrini, S. B. Nagel, A. Traverso, M. Yan, R. Côté, and T. C. Killian, “Two-photon photoassociative spectroscopy of ultracold  $^{88}\text{Sr}$ ,” *Physical Review A*, vol. 78, p. 062708, 2008.
- [56] B. Butscher, V. Bendkowsky, J. Nipper, J. B. Balewski, L. Kukota, R. Löw, T. Pfau, W. Li, T. Pohl, and J. M. Rost, “Lifetimes of ultralong-range Rydberg molecules in vibrational ground and excited states,” *Journal of Physics B: Atomic, Molecular and Optical Physics*, vol. 44, p. 184004, Sept. 2011.
- [57] F. Robicheaux, “Ionization due to the interaction between two Rydberg atoms,” *Journal of Physics B: Atomic, Molecular and Optical Physics*, vol. 38, p. 333, Jan. 2005.
- [58] V. Bendkowsky, B. Butscher, J. Nipper, J. B. Balewski, J. P. Shaffer, R. Löw, T. Pfau, W. Li, J. Stanojevic, T. Pohl, and J. M. Rost, “Rydberg Trimers and Excited Dimers Bound by Internal Quantum Reflection,” *Physical Review Letters*, vol. 105, p. 163201, Oct. 2010.
- [59] C. L. Vaillant, M. P. A. Jones, and R. M. Potvliege, “Multichannel quantum defect theory of strontium bound Rydberg states,” *J. Phys. B*, vol. 47, no. 15, p. 155001, 2014.

- [60] S. Ye, X. Zhang, F. B. Dunning, S. Yoshida, M. Hiller, and J. Burgdorfer, “Efficient three-photon excitation of quasi-one-dimensional strontium Rydberg atoms with  $n \sim 300$ ,” *Phys. Rev. A*, vol. 90, p. 013401, Jul 2014.
- [61] H. L. Schwartz, T. M. Miller, and B. Bederson, “Measurement of the static electric dipole polarizabilities of barium and strontium,” *Phys. Rev. A*, vol. 10, pp. 1924–1926, Dec 1974.
- [62] K. Bartschat and H. R. Sadeghpour, “Ultralow-energy electron scattering from alkaline-earth atoms: the scattering-length limit,” *Journal of Physics B: Atomic, Molecular and Optical Physics*, vol. 36, p. L9, Jan. 2003.
- [63] A. Traverso, R. Chakraborty, Y. N. Martinez de Escobar, P. G. Mickelson, S. B. Nagel, M. Yan, and T. C. Killian, “Inelastic and elastic collision rates for triplet states of ultracold strontium,” *Physical Review A*, vol. 79, p. 060702(R), 2009.
- [64] A. Gaëtan, Y. Miroshnychenko, T. Wilk, A. Chotia, M. Viteau, D. Comparat, P. Pillet, A. Browaeys, and P. Grangier, “Observation of collective excitation of two individual atoms in the Rydberg blockade regime,” *Nature Physics*, vol. 5, pp. 115–118, Jan. 2009.
- [65] E. Urban, T. A. Johnson, T. Henage, L. Isenhower, D. D. Yavuz, T. G. Walker, and M. Saffman, “Observation of Rydberg blockade between two atoms,” *Nature Physics*, vol. 5, pp. 110–114, Jan. 2009.
- [66] M. Saffman, T. Walker, and K. Molmer, “Quantum information with Rydberg atoms,” *Reviews of Modern Physics*, vol. 82, p. 2313, Aug. 2010.

- [67] T. Peyronel, O. Firstenberg, Q.-Y. Liang, S. Hofferberth, A. V. Gorshkov, T. Pohl, M. D. Lukin, and V. Vuletić, “Quantum nonlinear optics with single photons enabled by strongly interacting atoms,” *Nature*, vol. 488, no. 2, pp. 57–60, 2012.
- [68] T. E. Lee, H. Häffner, and M. C. Cross, “Collective quantum jumps of Rydberg atoms,” *Physical Review Letters*, vol. 108, no. January, pp. 1–5, 2012.
- [69] H. Schempp, G. Günter, M. Robert-De-Saint-Vincent, C. S. Hofmann, D. Breyel, A. Komnik, D. W. Schönleber, M. Gärttner, J. Evers, S. Whitlock, and M. Weidemüller, “Full counting statistics of laser excited Rydberg aggregates in a one-dimensional geometry,” *Physical Review Letters*, vol. 112, pp. 1–5, 2014.
- [70] N. Malossi, M. M. Valado, S. Scotto, P. Huillery, P. Pillet, D. Ciampini, E. Arimondo, and O. Morsch, “Full counting statistics and phase diagram of a dissipative Rydberg gas,” *Physical Review Letters*, vol. 113, pp. 1–5, 2014.
- [71] A. Urvoy, F. Ripka, I. Lesanovsky, D. Booth, J. P. Shaffer, T. Pfau, and R. Löw, “Strongly correlated growth of Rydberg aggregates in a vapour cell,” *arxiv.org/1408.0039*, 2015.
- [72] I. Lesanovsky and J. P. Garrahan, “Out-of-equilibrium structures in strongly interacting Rydberg gases with dissipation,” *Physical Review A - Atomic, Molecular, and Optical Physics*, vol. 90, pp. 1–5, 2014.
- [73] T. Pohl, E. Demler, and M. D. Lukin, “Dynamical Crystallization in the Dipole Blockade of Ultracold Atoms,” *Physical Review Letters*, vol. 104, p. 043002, Jan.

2010.

- [74] P. Schauß, M. Cheneau, M. Endres, T. Fukuhara, S. Hild, A. Omran, T. Pohl, C. Gross, S. Kuhr, and I. Bloch, “Observation of spatially ordered structures in a two-dimensional Rydberg gas.,” *Nature*, vol. 491, p. 87, Nov. 2012.
- [75] A. W. Glaetzle, M. Dalmonte, R. Nath, C. Gross, I. Bloch, and P. Zoller, “Designing Frustrated Quantum Magnets with Laser-Dressed Rydberg Atoms,” *Physical Review Letters*, vol. 114, no. May, pp. 1–5, 2015.
- [76] R. M. W. van Bijnen and T. Pohl, “Quantum Magnetism and Topological Ordering via Rydberg Dressing near Förster Resonances,” *Physical Review Letters*, vol. 114, no. June, p. 243002, 2015.
- [77] J. Honer, H. Weimer, T. Pfau, and H. P. Büchler, “Collective Many-Body Interaction in Rydberg Dressed Atoms,” *Phys. Rev. Lett.*, vol. 105, p. 160404, Oct 2010.
- [78] J. E. Johnson and S. L. Rolston, “Interactions between Rydberg-dressed atoms,” *Phys. Rev. A*, vol. 82, p. 033412, Sep 2010.
- [79] T. M. Weber, T. Niederprüm, T. Manthey, P. Langer, V. Guarnera, G. Baronini, and H. Ott, “Continuous coupling of ultracold atoms to an ionic plasma via Rydberg excitation,” *Physical Review A - Atomic, Molecular, and Optical Physics*, vol. 86, pp. 1–4, 2012.
- [80] M. P. Robinson, B. L. Tolra, M. W. Noel, T. F. Gallagher, and P. Pillet, “Spontaneous Evolution of Rydberg Atoms into an Ultracold Plasma,” *Physical*

- Review Letters*, vol. 85, no. 21, p. 4466, 2000.
- [81] T. C. Killian, T. Pattard, T. Pohl, and J. M. Rost, “Ultracold Neutral Plasmas,” *Physics Reports*, vol. 449, p. 77, 2007.
- [82] T. Wang, S. F. Yelin, R. Côté, E. E. Eyler, S. M. Farooqi, P. L. Gould, M. Koštrun, D. Tong, and D. Vrinceanu, “Superradiance in ultracold Rydberg gases,” *Physical Review A - Atomic, Molecular, and Optical Physics*, vol. 75, pp. 3–6, 2007.
- [83] K. J. Weatherill, J. D. Pritchard, R. P. Abel, M. G. Bason, a. K. Mohapatra, and C. S. Adams, “Electromagnetically induced transparency of an interacting cold Rydberg ensemble,” vol. 201002, p. 4, 2008.
- [84] C. Carr, R. Ritter, C. G. Wade, C. S. Adams, and K. J. Weatherill, “Nonequilibrium phase transition in a dilute Rydberg ensemble,” *Physical Review Letters*, vol. 111, pp. 1–6, 2013.
- [85] F. Karlewski, M. Mack, J. Grimmel, N. Sándor, and J. Fortágh, “State-selective all-optical detection of Rydberg atoms,” *Phys. Rev. A*, vol. 91, p. 043422, Apr 2015.
- [86] H. Schempp, G. Günter, C. S. Hofmann, C. Giese, S. D. Saliba, B. D. Depaola, T. Amthor, M. Weidemüller, S. Sevinçli, and T. Pohl, “Coherent population trapping with controlled interparticle interactions,” *Physical Review Letters*, vol. 104, pp. 1–4, 2010.
- [87] S. Sevinçli, C. Ates, T. Pohl, H. Schempp, C. S. Hofmann, G. Günter,

- T. Amthor, M. Weidemüller, J. D. Pritchard, D. Maxwell, A. Gauguet, K. J. Weatherill, M. P. a. Jones, and C. S. Adams, “Quantum interference in interacting three-level Rydberg gases: coherent population trapping and electromagnetically induced transparency,” *Journal of Physics B: Atomic, Molecular and Optical Physics*, vol. 44, p. 184018, 2011.
- [88] U. Raitzsch, R. Heidemann, H. Weimer, B. Butscher, P. Kollmann, R. Löw, H. P. Büchler, and T. Pfau, “Investigation of dephasing rates in an interacting Rydberg gas,” *New Journal of Physics*, vol. 11, 2009.
- [89] J. D. Pritchard, D. Maxwell, A. Gauguet, K. J. Weatherill, M. P. A. Jones, and C. S. Adams, “Cooperative atom-light interaction in a blockaded Rydberg ensemble,” *Physical Review Letters*, vol. 105, p. 193603, Nov. 2010.
- [90] T. Amthor, C. Giese, C. S. Hofmann, and M. Weidemüller, “Evidence of an antiblockade in an ultracold Rydberg gas,” *Physical Review Letters*, vol. 104, no. January, pp. 8–11, 2010.
- [91] H. Zhang, L. Wang, J. Chen, S. Bao, L. Zhang, J. Zhao, and S. Jia, “Autler-Townes splitting of a cascade system in ultracold cesium Rydberg atoms,” *Physical Review A - Atomic, Molecular, and Optical Physics*, vol. 87, pp. 1–5, 2013.
- [92] H. Zhang, L. Zhang, L. Wang, S. Bao, J. Zhao, S. Jia, and G. Raithel, “Autler-Townes spectroscopy with interaction-induced dephasing,” *Physical Review A*, vol. 90, p. 043849, 2014.
- [93] M. Tanasittikosol, C. Carr, C. S. Adams, and K. J. Weatherill, “Subnatural linewidths in two-photon excited-state spectroscopy,” *Phys. Rev. A*, vol. 85,

- p. 033830, Mar 2012.
- [94] W. Li, I. Mourachko, M. W. Noel, and T. F. Gallagher, “Millimeter-wave spectroscopy of cold rb rydberg atoms in a magneto-optical trap: Quantum defects of the  $ns$  ,  $np$  , and  $nd$  series,” *Phys. Rev. A*, vol. 67, p. 052502, May 2003.
- [95] C.-J. Lorenzen and K. Niemax, “Precise quantum defects of ns, np and nd levels in cs i,” *Zeitschrift fr Physik A Atoms and Nuclei*, vol. 315, no. 2, pp. 127–133, 1984.
- [96] C. Ates, S. Sevinçli, and T. Pohl, “Electromagnetically induced transparency in strongly interacting Rydberg gases,” *Physical Review A - Atomic, Molecular, and Optical Physics*, vol. 83, pp. 1–4, 2011.
- [97] C. Carr, R. Ritter, C. G. Wade, C. S. Adams, and K. J. Weatherill, “Nonequilibrium phase transition in a dilute rydberg ensemble,” *Phys. Rev. Lett.*, vol. 111, p. 113901, Sep 2013.
- [98] C. R. Monroe, E. A. Cornell, C. A. Sackett, C. J. Myatt, and C. E. Wieman, “Measurement of cs-cs elastic scattering at  $T = 30 \mu\text{k}$ ,” *Phys. Rev. Lett.*, vol. 70, pp. 414–417, Jan 1993.
- [99] M. Yan, B. J. DeSalvo, B. Ramachandhran, H. Pu, and T. C. Killian, “Controlling Condensate Collapse and Expansion with an Optical Feshbach Resonance,” *Phys. Rev. Lett.*, vol. 110, p. 123201, Mar 2013.
- [100] J. Stenger, S. Inouye, A. P. Chikkatur, D. M. Stamper-Kurn, D. E. Pritchard, and W. Ketterle, “Bragg Spectroscopy of a Bose-Einstein Condensate,” *Phys.*

- Rev. Lett.*, vol. 82, pp. 4569–4573, Jun 1999.
- [101] J. Steinhauer, R. Ozeri, N. Katz, and N. Davidson, “Excitation Spectrum of a Bose-Einstein Condensate,” *Phys. Rev. Lett.*, vol. 88, p. 120407, Mar 2002.
- [102] C. Pethick and H. Smith, *Bose-Einstein Condensation in Dilute Gases*. Cambridge University Press, 2002.
- [103] M. Theis, G. Thalhammer, K. Winkler, M. Hellwig, G. Ruff, R. Grimm, and J. H. Denschlag, “Tuning the Scattering Length with an Optically Induced Feshbach Resonance,” *Phys. Rev. Lett.*, vol. 93, p. 123001, Sep 2004.